1988

Circulation and Sediment Dispersal on the Louisiana-Mississippi-Alabama Continental Shelf.

Scott Page Dinnel
Louisiana State University and Agricultural & Mechanical College

Order Number 8917811

Circulation and sediment dispersal on the Louisiana-Mississippi-Alabama continental shelf

Dinnel, Scott Page, Ph.D.

The Louisiana State University and Agricultural and Mechanical Col., 1988

U·M·I
300 N. Zeeb Rd.
Ann Arbor, MI 48106

CIRCULATION AND SEDIMENT DISPERSAL ON THE LOUISIANA-MISSISSIPPI-ALABAMA CONTINENTAL SHELF

A Dissertation

Submitted to the Graduate Faculty of the
Louisiana State University
Agriculture and Mechanical College
in partial fulfillment of the
requirements for the degree of
Doctor of Philosophy

in

The Department of Marine Sciences

by
Scott Page Dinnel
B.S., University of South Carolina
M.S., Louisiana State University
December 1988

ACKNOWLEDGMENTS

This research was sponsored by the Louisiana Universities Sea Grant Program and Louisiana State University and the Mississippi-Alabama Sea Grant Consortium and the University of Alabama. The Rockefellar Scholarship Program, Louisiana Governor's Education Commission, and the Coastal Studies Institute, Louisiana State University provided additional support throughout my graduate student career. Dauphin Island wind data was provided by the Dauphin Island Sea Lab, Alabama.

No simple words can thank my advisor Bill Wiseman, his supervision, support and confidence enabled me to overcome many problems and complete my research. Will Schroeder contributed more that just research materials, ideas or collaboration, his unflagging enthusiasm got me over many rough spots. The rest of my committee, Harry Roberts, R. Eugene Turner, Shih-Ang Hsu, and Rick Shaw, all have aided me with interest, ideas and discussion.

Gerry Newman, the watchdog of the Marine Sciences Department, has saved me numerous times from missing deadlines, improper forms, and incorrect thoughts. Celia Harrod and Kerry Lyle have produced most of the figures in the dissertation and the eventual publications.

Most of all I would like to thank my wife, Beverly, for her companionship on a long, arduous, frustrating, sometimes tedious and trying, but eventually successful journey.

TABLE OF CONTENTS

LIST OF TABLES

LIST OF FIGURES

ABSTRACT

The circulation on the LMAS and adjacent regions has been characterized using historical hydrographic data and current meter data. Generalized seasonal circulation patterns have been proposed based on objective data over the inner shelf, outer shelf, and upper slope.

Hydrographic data, acquired from the National Oceanographic Data Center, covering the Louisiana-Mississippi-Alabama shelf (LMAS) and slope was analyzed. Seasonal maps of dynamic heights, relative to 500 db, were computed.

Inner shelf current data, acquired from the U.S. Army Corps of Engineers, was analyzed. Three current meter deployments (winter 1980, spring 1981, summer 1981) with up to eight mooring locations, along with coastal winds, were subject to complex spectral analyses, complex empirical orthogonal function analyses, and momentum balance analyses.

Westward flows on the inner shelf, outer shelf and upper slope in the spring and summer are interpreted as the northern and southern portions of closed cyclonic and anticyclonic circulation cells, respectively. Spring and summer midshelf flow is eastward, with offshelf flow over the eastern LMAS shelf break. Upper slope flow continues on westward in front of the Mississippi Delta, while outer shelf flow turns northward onto the shelf just east of the Delta. These two circulating cells are assumed to continue

in the fall. Flow in front of the Delta is to east in fall and winter. Winter shelf circulation appears to consist of a single cyclonic cell. There is weak offshelf flow all along the shelf-break in winter.

Wave-induced sediment resuspension and advection by subtidal bottom currents are both necessary for net sediment transport on the inner shelf. Long-term hindcast wave statistics for the LMAS, acquired from the U.S Army Corps of Engineers, were analyzed. Sediment resuspension during high wave conditions can occur in water depths of 40 m or less. Highest wave conditions, with durations on the order of hours per year, may resuspension sediment in up to 80 m water depth. Sediment transport occurs primarily during prefrontal winds conducive to long waves and cyclonic inner shelf flow in the winter and spring. Outer shelf and upper slope sediments are most likely to be resuspended only by hurricane condition waves or, possibly, by direct influence of the Loop Current.

1. INTRODUCTION

The Louisiana-Mississippi-Alabama shelf (LMAS) is a relatively small isolated portion of the continental shelf that lies along the United States' Gulf of Mexico coast. The LMAS extends east of the Mississippi Delta and the Louisiana barrier islands and south from the Mississippi-Alabama barrier islands (Figure 1). The seaward limit to the LMAS proper is the shelf break, which, along most of the shelf, lies near the 100 m isobath and is aligned approximately west-southwest east-northeast. The LMAS is roughly triangular in shape. It is bounded on the north by the Mississippi-Alabama barrier islands, on the west by a line running along the Chandeleur Islands and extending to the Mississippi Delta, and on the south by the shelf break. The isobaths approximate a right angle in the northwest portion of the shelf. The northern and western sides of the region are separated from large shallow sounds by barrier island systems with numerous tidal passes.

Although much smaller than the Louisiana-Texas and the West Florida shelves, the LMAS still has a significant socio-economic importance. The petroleum industry continues exploration and production on the continental shelves and slopes of the Gulf of Mexico, albeit at reduced levels of activity (Gramling and Brabant, 1984). The Tuscaloosa Trend, partially underlying the LMAS, has warranted interest at the national level. The U.S. Department of the Interior,

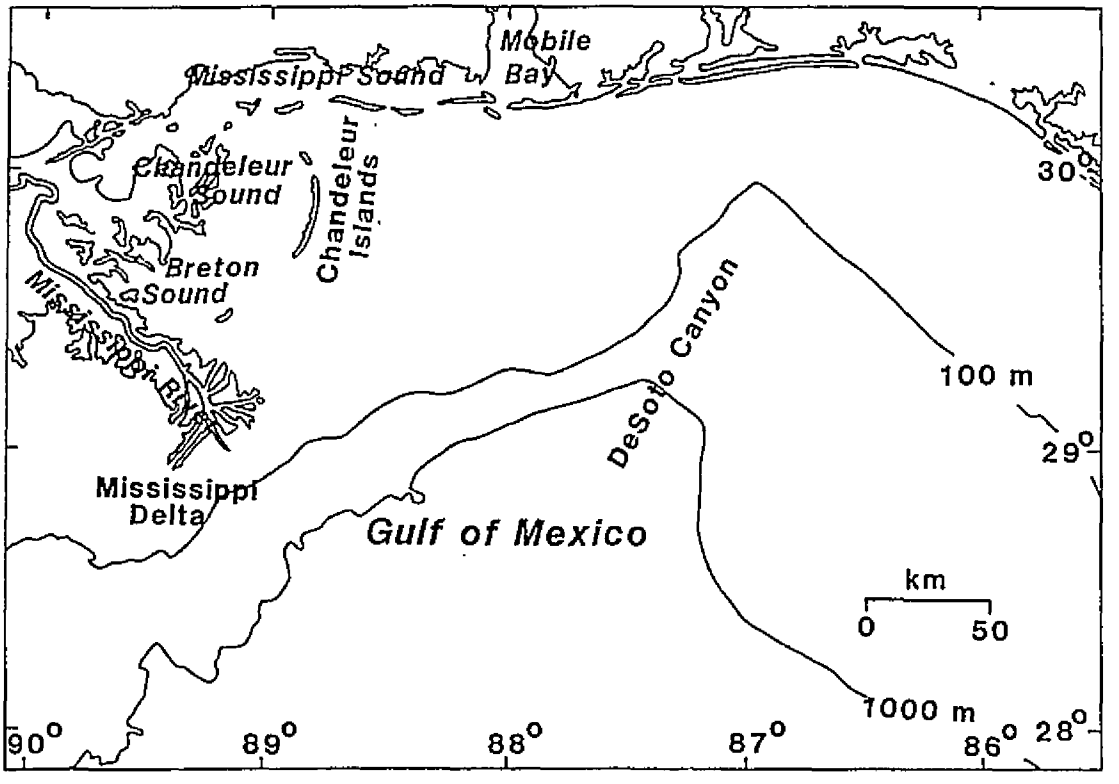

Figure 1. Location map of LMAS region.

Minerals Management Service, has funded an extensive data search and synthesis for the Tuscaloosa Trend region (Vittor, 1985) and a field project is currently underway in the region.

Economic uses of the LMAS region include major ship travel via the Mississippi River Gulf Outlet, Gulfport Ship Channel, Pascagoula Ship Channel and the Mobile Ship Channel. Dredge spoil maintenance associated with these channels across the sounds and inner shelf has prompted circulation surveys by the Corps of Engineers (Kjerfve, 1983; Kjerfve and Sneed, 1984) and modeling efforts (Outlaw, 1983; Sheng, 1983; Schmaltz, 1985).

The extensive estuarine and nearshore waters in the Mississippi Delta region and surrounding states are important for their commercial and recreational fish industries (Gunter, 1963; Thompson and Arnold, 1971; Larsen et al, 1980; Vittor, 1985).

Sediment transport processes are of immediate concern to dredge spoil transport but are also important in understanding the transport of offshore drilling muds (TRI, 1983) and the fate of pollutants and sediment-borne contaminants. The historical transport of sediment is of interest to a basic understanding of continental shelf sedimentation in this region.

The distribution of sediment types and mineral suites along with heavy mineral source identification have been reported on different occasions for the LMAS region

(Goldstein, 1942; Scruton, 1956; Shepard, 1956; Curray, 1960; Van Andel, 1960; Van Andel and Poole, 1960; Fairbank, 1962; Ludwick, 1964; Upshaw et al, 1966; Doyle and Sparks, 1980; Kindinger et al, 1982; U.S. Department of the Interior, 1982; U.S. Department of Commerce, 1985). The large-scale patterns of the sediment size distribution maps of Scruton (1956), Shepard (1956), Ludwick (1964), Doyle and Sparks (1980), Kindinger et al (1982), the U.S. Department of the Interior (1982) and the U.S. Department of Commerce (1985) are essentially the same. Small-scale variability is high between maps. All reflect a dependence on the sampling scheme. It has been reported that sediment size variability is large, even at spatial scales of hundreds of meters, on the inner shelf south of Mobile Bay (W. W. Schroeder, personal communication).

Goldstein (1942) described two sediment provinces in this region. The Mississippi Province (MP), primarily silt and clay, was characterized by a heavy mineral suite of amphiboles and pyroxenes, attributed to present day Mississippi River discharge. The Eastern Gulf Province (EGP) was predominantly fine sands, with heavy minerals, kyanite and staurolite, and a southern Appalachian source. Fairbank (1962) described a boundary between the MP and EGP on the LMAS, with the latter encompassing Mobile Bay, Mississippi Sound, and the inner shelf offshore of the Mississippi-Alabama barrier islands. Fairbank also added to the sediment characterization of these two provinces. He stated that MP

had a higher proportion of iron oxides, a lower proportion of resistive minerals (i.e. garnet, zircon, tourmaline), different types of organic debris, more fecal pellets and worm tubes, and less shell fragments.

Clay minerals are transported onto the LMAS via the Mississippi River and the Mobile River System. The Mississippi River contributes a smectite rich composition (60-80% smectite, 10-20% kaolinite, 20-30% illite) (Griffin, 1962). Although only an estimated 25-35% moves east to the LMAS (Scruton, 1956) the Mississippi River clays still dominate the shelf. The Mobile River system contributes one thirteenth the suspended sediment that the Mississippi River does and has approximately equal percentages of smectite and kaolinite (Griffin, 1962). A shelf decrease in smectite and an increase in kaolinite as one moves eastward from the Mississippi Delta has been noted (Huang et al, 1975). Shelf clays in the LMAS region are primarily smectites (75%), with 18% kaolinite and 7 % illite.

Sediment is introduced to the LMAS by river discharge. Some is first deposited in the shallow sounds and bays (Shepard, 1956; Scruton, 1956). Some transported directly onto the LMAS during spring floods (Upshaw et al, 1966; Abston et al, 1987). Inner shelf and adjacent sound sediments in this region are resuspended and transported by tidal action (Scruton, 1956; Sheng, 1983), and wind waves and currents due to extratropical cyclones and the associated cold fronts (Scruton, 1956; Schroeder et al,

1985). Midshelf sediments are reworked approximately once every one to two years and deeper shelf sediments are reworked once every five years by hurricanes (Upshaw et al, 1966; Swift et al, 1971).

Although a great deal of descriptive work has been done in this region, little actual process work has been attempted. Using Landsat images, not in situ current measurements, Schroeder et al (1985) have qualitatively examined shelf-sound sediment transport processes during cold-air outbreaks. Their results are restricted to sediment transport in the surface layers and constrained by the lack of ground truth currents. Basic understanding of sediment transport on the LMAS should begin with a description of the general circulation, identification of transport processes and their frequency of occurrence, and the coupling of the advection and resuspension processes.

Circulation on the LMAS is not fully understood. Leipper (1954) suggested an easterly flow in June, and a closed cyclonic gyre, in December, with easterly flow over the slope. These data were most likely highly influenced by the Loop Current.

Spatially and temporally isolated drifter studies and quasi-synoptic hydrographic data are insufficient to determine a complete picture of the LMAS circulation. Chew et al (1962) suggested the bifurcation of an offshore, northward current south of the Mississippi Delta. This bifurcation is inferred from a saddle topography of the

dynamic heights determined from a single cruise. Recovery sites of drifters released within 30 km southeast of the Mississippi Delta in the fall and summer of 1960 and 1961 were consistent with predominantly westward currents near the Delta in the fall, and predominantly eastward currents in early summer (Ichiye, 1960). Large observed variations in shelf salinity, temperature and density distributions were due primarily to seasonal Mississippi River discharge (Ichiye, 1960; Chew et al, 1962; Drennan, 1968). Using drifter and surface hydrographic data, Drennan (1968) suggested eastward summer and fall slope currents, offshore of the LMAS, that bifurcate over the De Soto Canyon, resulting in a northeastward parabathic continuation of flow and an eastward branching current. In addition, he suggested a winter cyclonic circulation over the entire shelf. Tolbert and Salsman (1964) observed that most drift cards released on the inner shelf offshore of Panama City, Florida, were recovered (67%) on the Florida coastline adjacent to the release point, and that 20% were recovered from the east coast of Florida. Molinari et al (1979) summarized extensive drifter study results for the LMAS. Fifty to 75% of recovered drifters released inshore of the 200 m isobath from January to June were recovered on the Louisiana-Mississippi-Alabama-Florida coast. Those released offshore of the 200 m isobath had a 50% east coast of Florida recovery rate. Fifty percent of the recovered drifters released to the south or southeast of the Mississippi River

Delta were found on the west Louisiana or Texas coasts. Half of the recovered drifters released over the outer shelf and slope from August to November were found west of the Mississippi Delta. Kindinger et al (1982) deployed drifters in a spatial grid over the western LMAS in April 1981. Recovery was good, 79%, but results were not readily interpreted. Under a predominantly northeast wind, drifters near the Mississippi barrier islands moved eastward. Those offshore of the shelf break moved west across the delta. General movement of the remainder was to the northwest. Schroeder et al (1987) inferred cyclonic circulation on the shelf in winter and LMAS to Loop Current exchange in winter, spring and summer with various buoys serving as unplanned drifters.

Drifter data are difficult to interpret, when only release and recovery points are known. Never-the-less, there is general agreement on a few points. A shelf-scale gyre exists on the LMAS in the winter and spring with some recirculation possible throughout the year. Flow on the upper slope, offshore of the LMAS, is eastward in the summer and fall, with some portion of this flow moving across the De Soto Canyon and southeast along the eastern flank of the Canyon. There must be shelf-break exchange in all seasons, but it is more likely to involve large transport during a northward Loop Current intrusion. Westward transport across the Delta front is possible in all seasons, but is more likely in the summer and fall and probably originates over

the upper slope.

Loop Current features are observed in the dynamic topographies for the Gulf of Mexico. These features dominate the upper 1000 m in the eastern Gulf (Austin, 1955; Collier et al, 1958; Duxbury, 1962; Molinari et al, 1978), and occasionally intrude right up onto the LMAS where they directly influence circulation (Huh et al, 1981; Schroeder et al, 1987). Sturges and Evans (1983) found coherence between Loop Current positions and sea level at St. Petersburg, Florida, on long time scales. The fast southward currents over the upper slope, driven by northward extensions of the Loop Current, resulted in lower water on the west Florida coast.

Current meter data for the LMAS region are relatively sparse. A few isolated current meter records exist for the outer LMAS and slope regions. Both westward and eastward mean flows have been reported from the outer shelf and upper slope in this area on seasonal time scales (Molinari et al, 1979; Ebbesmeyer et al, 1982; Molinari and Mayer, 1982; Wiseman and Dinnel, 1988). Strong current events were reported by all these investigators. Flow reversals with sustained current velocity events of 0.30 to 0.50 m/s over periods of 20 to 30 days were, in each case, attributed to the Loop Current or a Loop Current feature.

In the next chapter I describe the outer LMAS and upper slope circulation. I utilize maps of dynamic height and the fresh water content calculated from historical hydrographic

data. Although primarily used in a deep ocean setting, in situ hydrographic data have successfully been used to estimate geostrophic velocities and flow in marginal sea and continental shelf settings (Helland-Hansen, 1934; Stefannson et al, 1971; Herman, 1982; Smedstad and Weber, 1986). Csanady (1979) and Cochrane and Kelly (1986) have used historical hydrographic data to determine average dynamic topographies and geostrophic flows in shelf regions. Fresh water content has been used to suggest possible circulation patterns on the Mid Atlantic Bight (Ketchum and Keen, 1955) and the Louisiana-Texas shelf (Dinnel and Wiseman, 1986).

Inner shelf circulation over the LMAS has been inferred from synthesis of unplanned drifters, current meters and local wind records for specific events during short time periods of the fall and winter (Schroeder et al, 1987) and from Landsat imagery for post-cold-air outbreak conditions (Schroeder et al, 1985).

Current meter data, from depths shallower than 40 m, is mainly restricted to single season deployments along the Mississippi-Alabama inner shelf. Kjerfve and Sneed (1984) reported a mean westward flow for single season deployments in winter and spring. Identification of a mean pattern from multi-year summer records was not possible because of highly variable winds (Chuang et al, 1982). Murray (1972) reported on inner shelf currents just east of the Mississippi Delta, but the data set was too short to determine a "mean" flow. Shay and Elsberry (1987) reported on current meters from the

De Soto Canyon region, yet their analysis was restricted to inertial frequency currents associated with Hurricane Frederic in 1979.

Inner shelf circulation is described, in Chapter 3, through an in-depth analysis of current meter data collected by Raytheon (1981a,1981b,1981c) for the U.S. Army, Corps of Engineers, and described by Kjerfve and Sneed (1984). Three techniques will be used to analyze time series of current meter, water level, and wind data from three seasons. These techniques are spectrum and cross-spectrum analysis, complex empirical orthogonal function analysis and estimation of the vertically-integrated momentum balance. A description of the mean circulation patterns, the spatial and temporal distribution of the flow, and a description of the variability in circulation patterns due to meteorological forcing, i.e. cold fronts, are the desired results.

In Chapter 4 I describe shelf sediment transport. I focus on the mechanisms of tidal currents, subtidal currents (described in Chapters 2 and 3), waves, and couplings between them. The inner shelf current meter deployments provide the tidal and subtidal current information. Wave statistics were acquired from a 20-year hindcast performed by the Wave Information Study (here after referred to as WIS), (U.S. Army, Draft Report) for four stations in the LMAS region. In situ significant wave height and dominant period were collected by the National Data Buoy Office (NDBO) at an offshore buoy. These are combined with winter

and spring current meter information from the inner shelf to determine the relationship of sediment transport on the shelf with cold-front passage.

2. SEASONAL FLOW ON THE OUTER SHELF AND UPPER SLOPE

HYDROGRAPHIC DATA

Hydrographic data (temperature, salinity and calculated sigma-t values) were acquired from the National Oceanographic Data Center (NODC). These data cover the continental shelf and upper slope from 86.5 W^{o}, east of the De Soto Canyon, to 89.5^{o} W, and and from the coast offshore to beyond the 1000 m isobath. Data from over the western flank of De Soto Canyon and the upper slope were included so that I might describe the circulation over areas adjacent to the LMAS proper. The data set was collected during cruises from 1937 to the late 1970's, with the majority of the data taken in the 1960's and 1970's. More recent data either has not reached NODC has not been assimilated into the data banks.

The hydrographic data were partitioned by longitude and depth (Dinnel, 1983). Parabathic segments were created, assuming flow to be predominantly along-isobath, by partitioning at half degree longitudes along regions bounded by constant depths. These longitudinal partitions create quasi-diabathic transects. Meridional boundaries are 86.5^{o}, 87.0^{o}, 87.5^{o}, 88.0^{o}, 88.5^{o}, 89.0^{o}, and 89.5^{o}. Transects, then, run along the 86.75^{o}, 87.25^{o}, 87.75^{o}, 88.25^{o}, 88.75^{o}, and 89.25^{o} meridians. Depth boundaries are the 0, 20, 40, 60, 80, 100, 150, 200, 300, 400 and 500 m isobaths. For example, a segment could be bounded by the 60 and 80 m

isobath and by the 87° and 87.5° meridians (Figure 2).

Temporal variation in the hydrographic data will be described by tri-monthly partitions chosen as seasons. Monthly and bimonthly partitions were not chosen because they were data sparse. Surface salinity patterns on the outer shelf occur in response to the Mississippi River discharge (Ichiye, 1960; Chew et al, 1962; Drennan, 1968). Based on a distributary dependent partition of flow, 47% of the Mississippi River discharge from the birds-foot delta potentially flows eastward onto the LMAS (U.S. Army, 1974; Dinnel, 1986). On a monthly mean basis, the regional rivers along the LMAS coast usually discharge less than 50% of the estimated Mississippi River flow (Figure 3). The rivers discharging onto the LMAS, with the exception of the Mississippi River, flow onto the inner shelf. The Mississippi River, because of geologically recent delta building, discharges directly onto the outer LMAS and slope. Therefore, the Mississippi River discharge determines the hydrographic seasons of the shelf. The lowest river input is in the fall (September, October and November). The onset of the annual flood increases river input onto the shelf in winter (December, January and February). The highest river input occurs in the spring (March, April and May). The summer river input (June, July and August) decreases to the fall low. Estimates of local precipitation and evaporation

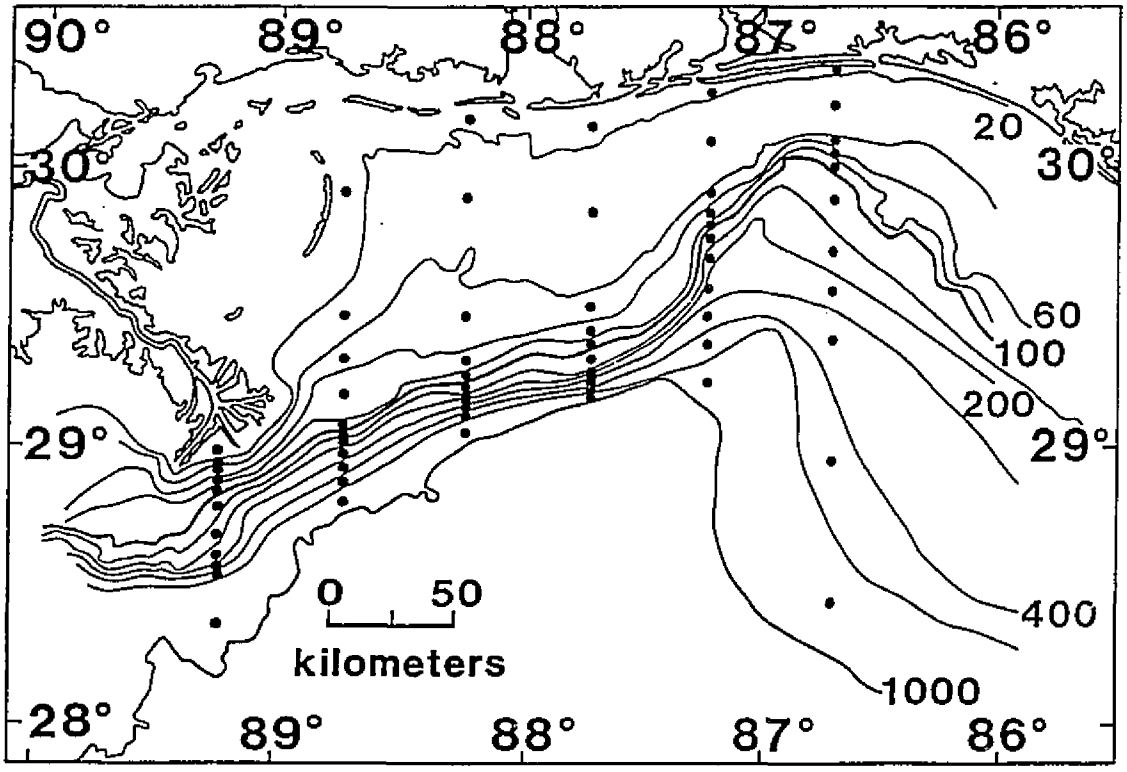

Figure 2. Plan view of hydrographic areal divisions. Dots represent station locations characteristic of individual divisions. Depth contours in meters.

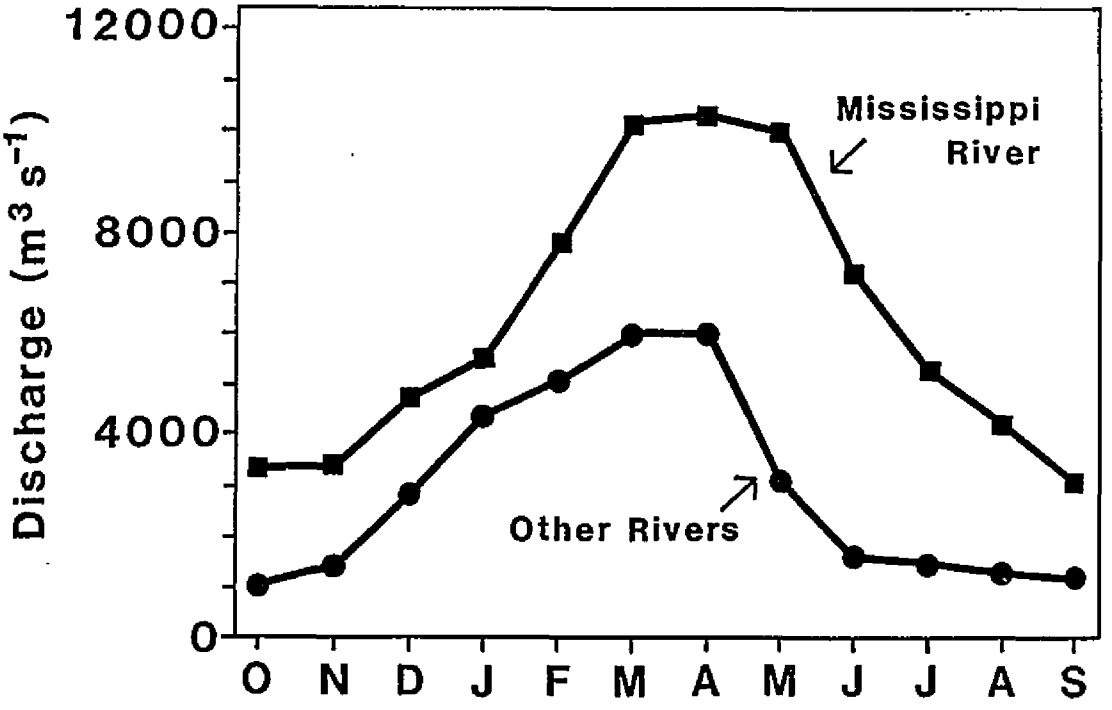

Figure 3. Direct river discharge to the LMAS. Monthly means from the Mississippi River and local rivers in Louisiana, Mississippi, and Alabama, (Schroeder and Lysinger, 1979; U.S. Department of Commerce, 1974, 1985b).

differences are at best 10% of the seasonal Mississippi River discharge and so any influence is masked.

ANALYSIS

Geopotential Calculations

Characteristic profiles of salinity, temperature and sigma-t were estimated for each segment, by season and for the entire data set. The median value was selected as representative at each depth where data occurred. The median was chosen, rather than the mean, in order to reduce the influence of large spatial and temporal variation in the surface layers. A third order polynomial in pressure was then fit to each of the resultant data profiles. The bottom depth for each characteristic profile was chosen to be the average of the bounding isobaths for that segment. When an individual profile did not extend to this depth, that profile was assumed to be isothermal, isohaline and isopycnal between the deepest available data and the bottom. Real data that exceeded the segment average bottom depths were used in the curve fit, but not in subsequent integration.

Geopotential anomalies, D, were computed for each segment by integrating the specific volume anomaly, δ,

$$D = \int_{p_2}^{p_1} \delta \, dp.$$

from one isobaric surface, p_2, to another, p_1, using the

trapezoidal rule and 1 db increments. The specific volume anomaly, δ was determined as:

$$\delta = \Delta_{s,t} + \delta_{t,p} + \delta_{s,p}.$$

Where $\Delta_{s,t}$ is the thermosteric anomaly, $\delta_{t,p}$ is the anomaly due to temperature and pressure, and $\delta_{s,p}$, is the anomaly due to salinity and pressure. Note that, $\delta_{s,t,p}$, the anomaly due to salinity, temperature and pressure is small and was ignored (Sverdrup et al, 1942).

Csanady (1979) suggested that the integration of the specific volume anomaly solely over the water column is inadequate in shallow regions. If the bottom pressure is less than the reference pressure, the integration should be done in two parts. The first part,

$$D_d = \int_{p_b}^{p} \delta \, dp,$$

is the integration of the specific volume anomaly from p_b, the pressure surface at the bottom, or at a reference surface shallower than the bottom, to the desired pressure surface, p. The second part,

$$D_b = \int_{p_r}^{p_b} \delta \, dp,$$

the geopotential anomaly integrated along the bottom from the reference surface, p_r, to the bottom of each segment profile, p_b. D_b is only added to D_d when p_r is greater than

p_b.

Csanady (1979) pointed out that isopycnals tilting toward the shore create positive geopotential anomalies. Isopycnals tilting upward toward the shore create negative geopotential anomalies. A detailed knowledge of the tilt of the specific volume anomalies as they intersect the bottom is required in a shelf-slope region. Good cross-shelf data profiles at closely spaced stations represent the bottom specific volume anomaly field better than only a few cross-shelf stations. To approximate the term D_b, linear interpolations along the bottom were made between stations (Figure 4). This procedure is equivalent to that described by Helland-Hansen (1934).

Problems arise when stations are few in number across the upper slope and shelf, or when large specific volume changes occur over short distances near the shelf break. These situations generate inflated inner shelf geopotential anomaly estimates.

Dynamic heights, are simply the geopotential anomaly at a particular pressure divided by the acceleration due to gravity. The computed dynamic heights are referenced to the 500 db surface. The dynamic structure at 0 db (sea surface) or at any pressure above the 500 db reference pressure can be determined. The 500 db pressure surface, although not a level of no motion, should be below the level of seasonal hydrographic changes and stable relative to the water column above. Specific volume anomalies at the reference pressure

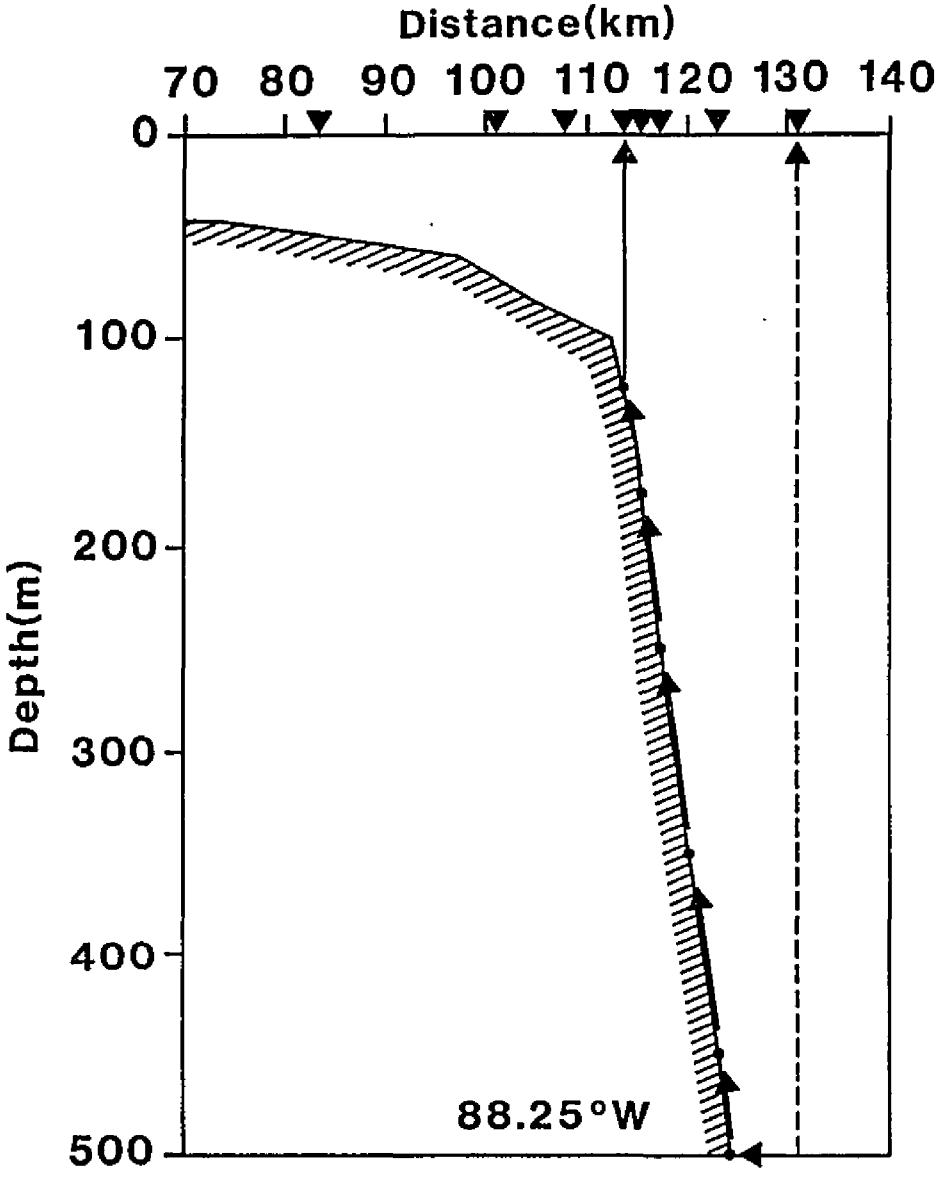

Figure 4. Shelf cross-section at 87.25° W, showing possible dynamic height integration path across shelf.

for each transect and season are listed in Table 1. The alongshelf variability is greater than the interseasonal variability. Most of the seasonal dynamic height variations are assumed to occur above this level. This assumption allows interseasonal comparisons. There is dynamic structure at 500 db relative to deeper pressures (Austin, 1955; Collier et al, 1958; Duxbury, 1962; Molinari et al, 1978). This may be attributable to the Loop Current or to associated features. The northward extent of Loop features is not well documented for some periods covered by my historical data. During other periods, especially in the 1960 and 1970's, the Loop Current path is moderately well known. During these times the Loop Current and associated features appear to have been a degree of latitude or more to the south of the study area. I, therefore, have not attempted to portion my hydrographic data to further eliminate any Loop Current influence. The seasonal dynamic height topography at 0 and 50 db with respect to 500 db was mapped and contoured at intervals of 5 dynamic cm over the upper slope and outer shelf. Dynamic heights were not computed for the mid and inner shelf. A priori, it was assumed that the flow is ageostrophic in shallow waters.

Furthermore, errors have been incorporated into the calculation of the geopotential anomalies from the curve fitting procedure used to approximate the temperature, salinity and sigma-t profiles. The third-order polynomials tended to overestimate the surface values and underestimate

Table 1. Seasonal specific volume anomaly values for each transect at the reference pressure 500 db. Units are $x10^{-4}$ m^3/kg.

Season	89.25°	88.75°	88.25°	87.75°	87.25°	86.75°
Spring	11.31	9.34	10.08	9.42	9.62	10.14
Summer	9.06	9.44	9.53	9.32	8.87	9.33
Fall	9.42	9.82	9.63	8.92	9.34	9.83
Winter	10.49	9.14	9.15	9.53	9.23	7.13

the deepest values. Errors were greatest when there were large vertical gradients over short depths and least when the water column was vertically homogeneous. Dynamic height errors from poor bottom data would accumulated during integration along the bottom. This supports the neglect of the more landward stations.

Fresh Water Content Calculations

The third order polynomial in pressure fit to the median salinity profile data, for each seasonal segment, was vertically integrated to determine a characteristic salinity for each segment. Stations shallower than 100 m were integrated to the bottom, deeper stations were integrated to a maximum of 100 m. This is approximately the depth of the shelf break, and approximately the depth of salinity profile maxima. The fresh water fraction, F, of any segment volume was estimated as,

$$F = 1 - \left(\frac{1}{S_o h_i} \int_0^{h_i} S_i \, dz \right),$$

where S_o is a reference salinity, S_i a characteristic salinity profile at station i, and h_i is the water depth at station i. The reference salinity was taken at 36.6 ppt, approximately the maximum salinity in the upper 500 m. Ninety-five percent of the measured salinities are below this reference value. The fresh water fraction at station i multiplied by the volume of segment i gives the fresh water

volume this segment. This fresh water volume divided by the surface area of segment i is the average height of fresh water in that segment. Estimates of the height of fresh water at each segment were plotted on a map of the shelf and contoured by hand for each season.

The segment fresh water volumes were summed over the entire shelf to give the total fresh water present on the shelf. Only those transects west of 87^{o} W were included in this procedure. Because of data sparseness, only 54 to 78% of the total shelf volume is represented in any given season (Table 2).

To recover data from segments not actually sampled, missing fresh water heights were interpolated from the contour maps. The fresh water volume was then determined through multiplication by the appropriate segment surface area. The adjusted fresh water volumes are also listed in Table 2.

RESULTS

Dynamic Height Topography

The spring 0/500 and 50/500 db dynamic height topographies are consistent with weak geostrophic flow in the vertical (Figure 5). General circulation is clockwise around a topographic high centered on the central outer shelf. Geostrophic flow is westward across the Mississippi Delta (hereafter referred to as the Delta), but turns northward just east of the Delta

Table 2. Fresh water volumes, calculated from a reference salinity of 36.6 ppt, and the shelf volume percentage sampled for each season, for the upper 100 m of the LMAS region from 87° to 89.5° W.

Season	Fresh Water Volume (km^3)	Coverage (%)	Prorated Volume (km^3)
Spring	31.90	64	42.29
Summer	41.40	78	47.98
Fall	45.91	54	69.93
Winter	29.98	62	37.31

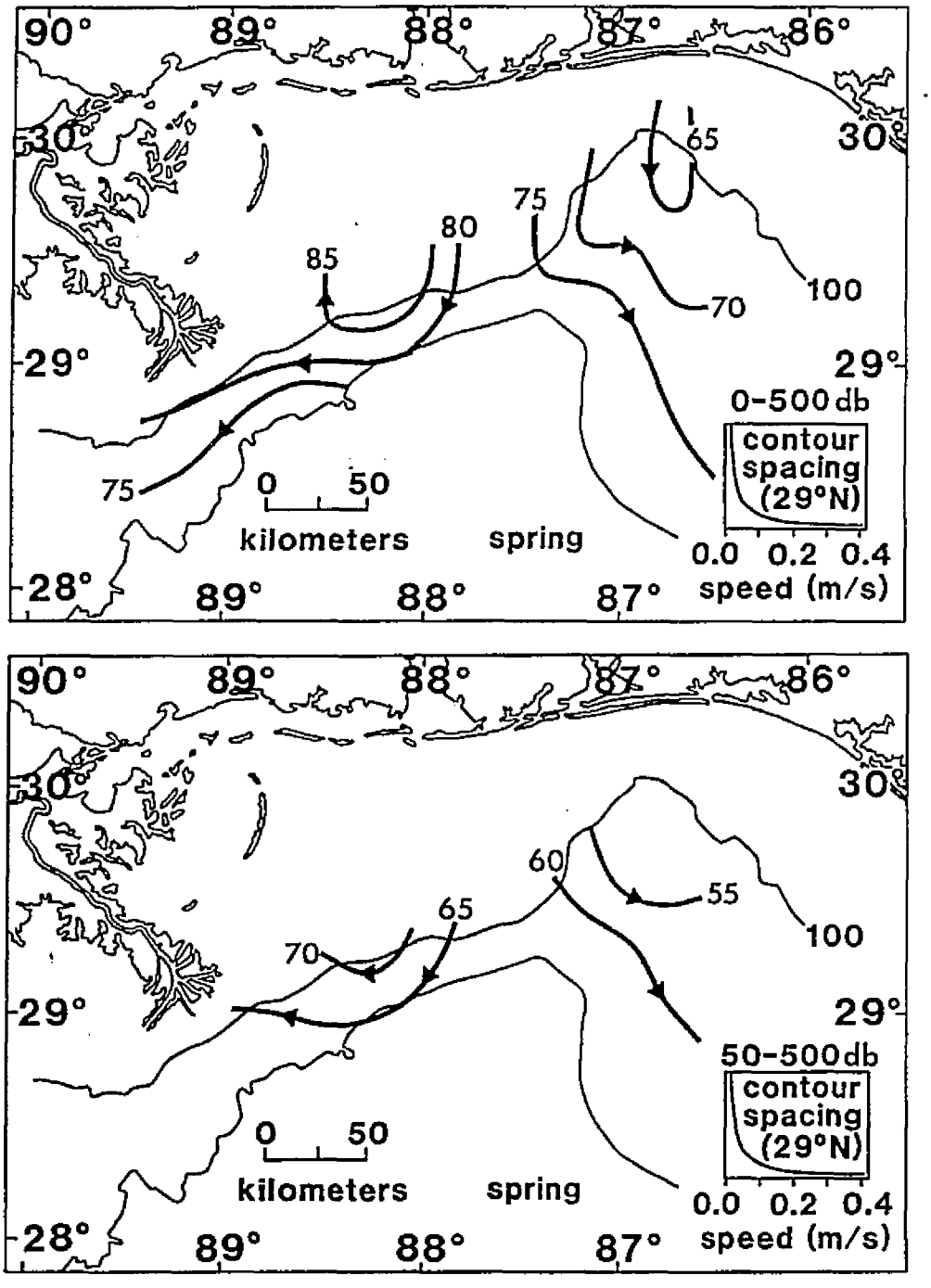

Figure 5. Spring dynamic height topographies, 0/500 db, 50/500 db. Contours are in dynamic centimeters, arrows indicate direction of flow.

and west of the dynamic high. A low at the head of the De Soto Canyon (hereafter referred to as the Canyon) is indicative of southeastward parabathic flow over the eastern flank of the Canyon. Offshelf flow occurs over the eastern LMAS. This flow splits over the upper slope and flows east across the Canyon and west around the high. Geostrophic speeds, estimated from the distance between isopleths, are 0.05 m/s or less.

A topographic high occurs in roughly the same place on the central shelf break during summer (Figure 6). The low is also present, but shifted westward over the Canyon flank. There is little difference in topography between the Delta and the center of the high, yet there is a rapid drop in topography alongshelf northeast of the high. The flow is offshore at 0 db and eastward, oblique to the isobaths, at 50 db. Geostrophic speeds are approximately 0.1 and 0.05 m/s at 0 and 50 db, respectively. Once over the upper slope, flow on both surfaces splits and moves parabathically. Due south of the Delta, shelf break flow is westward. Dynamic heights are lower to the west. An onshore flow, adjacent to the Delta, may exist in this region. Flow over the Canyon is weak, less than 0.05 m/s, and northeastward.

The dynamic heights in the fall are the highest of any season. The topographic high persists and covers most of the shelf on the 0 db surface (Figure 7). Quasi-parabathic geostrophic currents flow southward along the western flank of the Canyon and westward along the shelf break and over

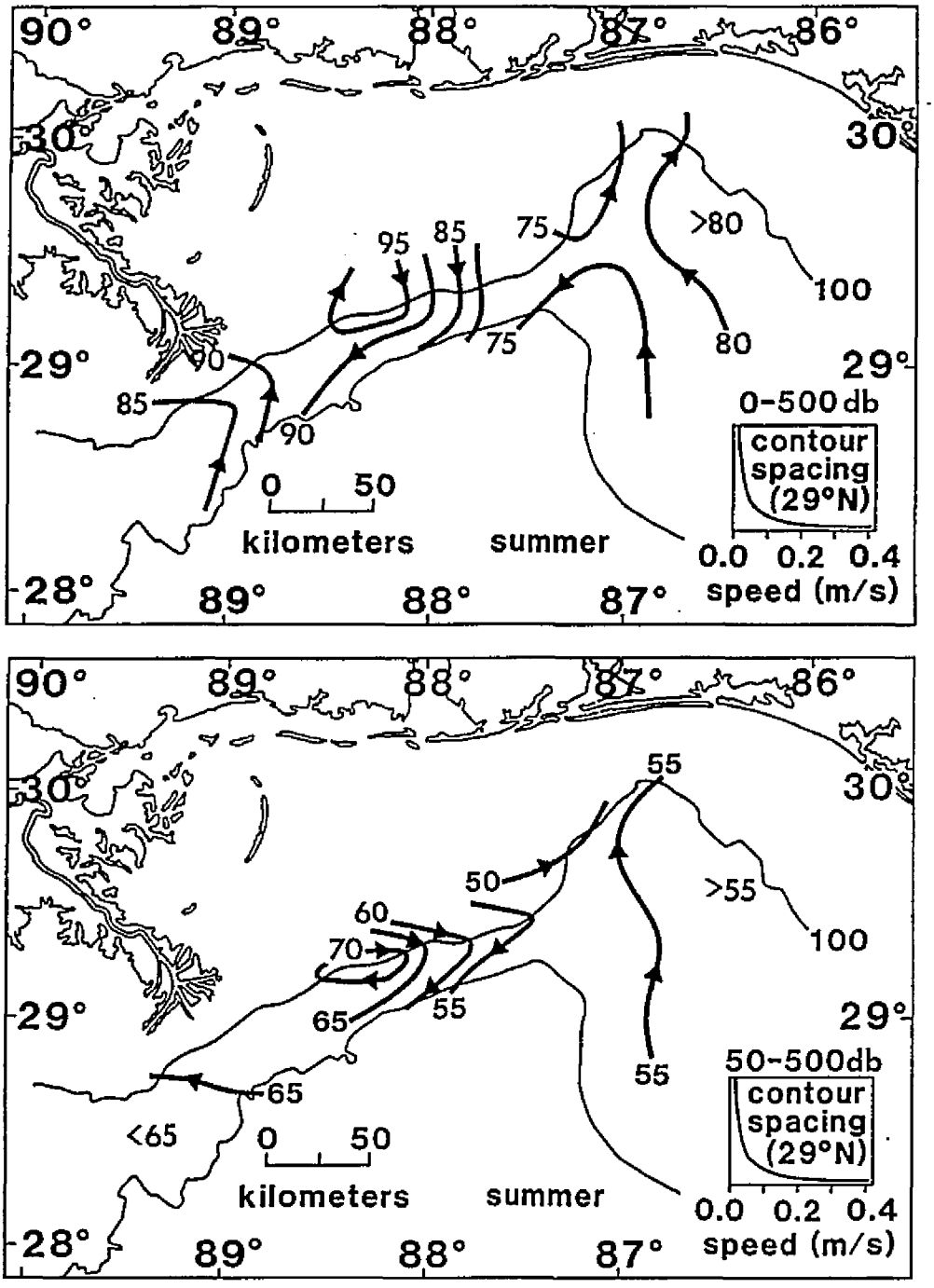

Figure 6. Summer dynamic height topographies, 0/500 db, 50/500 db. Contours are in dynamic centimeters, arrows indicate direction of flow.

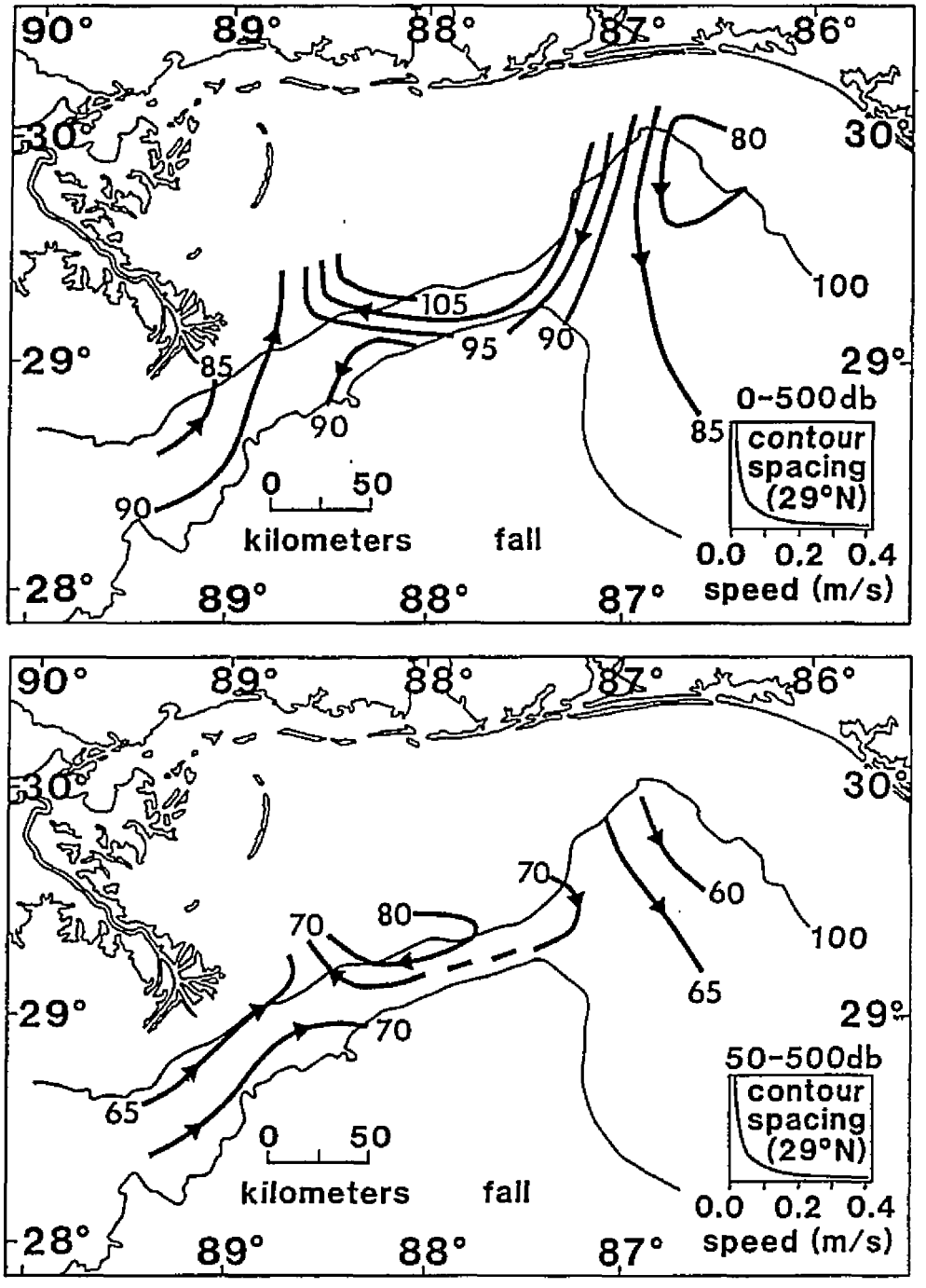

Figure 7. Fall dynamic height topographies, 0/500 db, 50/500 db. Contours are in dynamic centimeters, arrows indicate direction of flow.

the upper slope. Weak eastward flow across the Delta converges with the alongshelf westward flow and turns onshore just east of the Delta. Low topography, at the head of the Canyon, is consistent with southeastward parabathic flow along the eastern flank. Topography on the 50 db surface is similar but not identical to the 0 db surface (Figure 7). The high is limited to the central shelfbreak. The dynamic height contours are nearly closed on the landward side. Weak anti-cyclonic flow, less than 0.05 m/s, around the high joins a weak eastward flow from across the Delta and moves onshore just east of the Delta. Landward of the high, flow is eastward and shelf normal at the shelf break over the western Canyon flank. Over the eastern Canyon flank, flow is along isobath.

A dramatic reduction in dynamic heights occurs between the fall and winter season. The topographic high is much reduced on both the 0 and 50 db surfaces and has shifted up onto the shelf (Figure 8). There is a weak trough that extends along the upper slope, separating dynamic heights of about the same magnitude over the slope and shelf. Geostrophic speeds are much less than 0.05 m/s. Very weak cross shelf flow persists over the eastern LMAS, with speeds of less than 0.05 m/s. This flow splits, moving west along the outer shelf and upper slope and east up the Canyon. Flow south of the Delta is eastward over the outer shelf and westward over the upper slope.

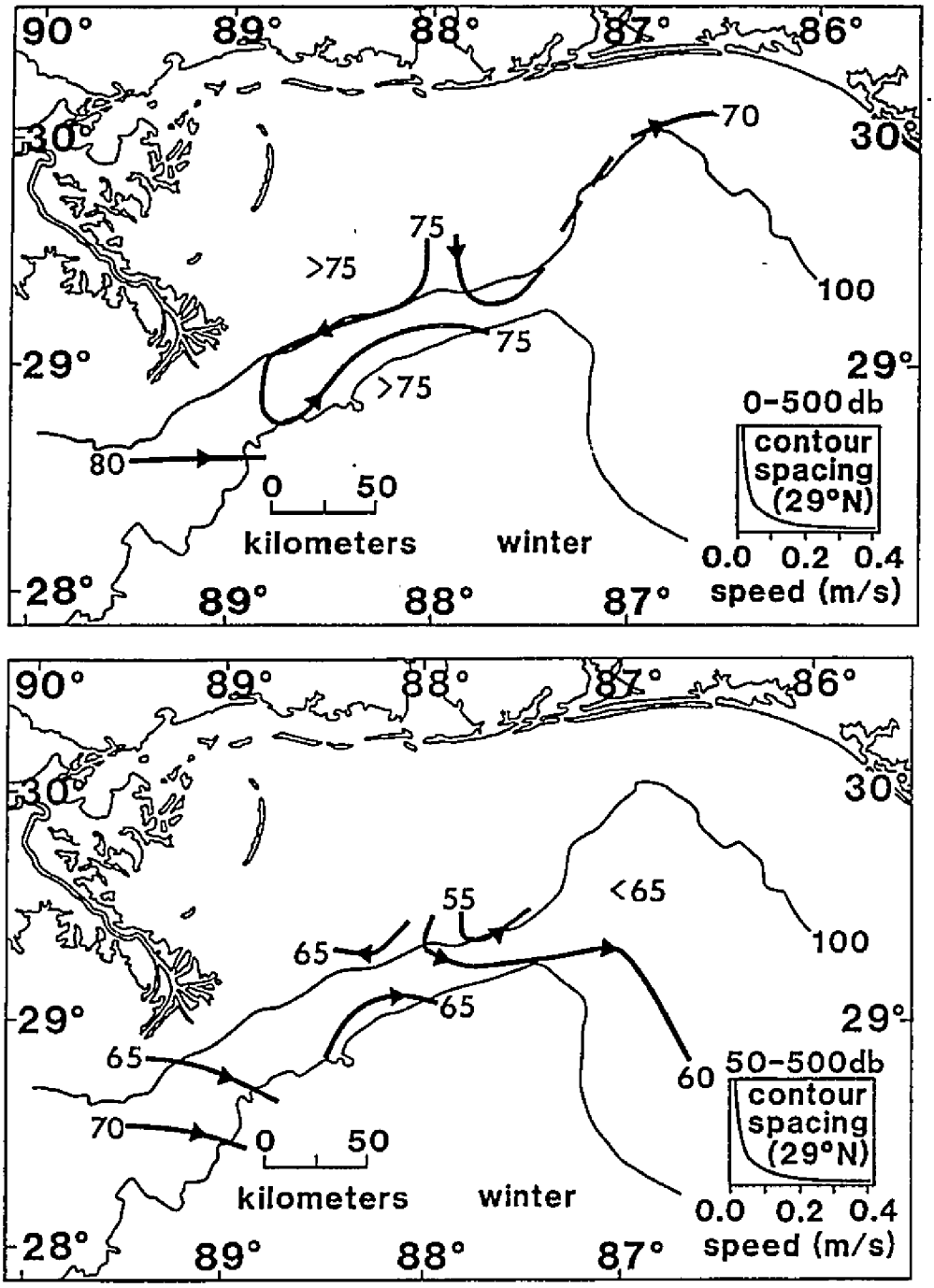

Figure 8. Winter dynamic height topographies, 0/500 db, 50/500 db. Contours are in dynamic centimeters, arrows indicate direction of flow.

A high and a low topographic feature, were found in all seasons, on both the 0 and 50 db levels, except the winter. The topographic high is centered on the outer shelf or shelf break roughly in the center of the LMAS, slightly west of 88°W. The low is weak and usually located near the head of the Canyon. Both features are present in the annual mean dynamic topography (Figure 9). General circulation around these features produces offshelf flow on the eastern LMAS. Westward alongshelf flow occurs south of the high. Geostrophic flow just to the east of the Delta is onshelf. Flow up the eastern flank of the Canyon at the shelf break is seasonal and depends on the location of the topographic low.

Fresh Water Content

Regions of high fresh water content appear to originate from the Mississippi Delta and disperse eastward along the shelf break (Figure 10). Lower fresh water content is found over the upper slope, over the De Soto Canyon, and over the eastern portions of the LMAS.

The spring fresh water content is highest immediately east of the Mississippi Delta along the shelf break (Figure 10). Low values occur over the upper slope, with the remaining shelf having moderate content and fairly even distribution. Summer fresh water content is similar to that in the spring, but the high content region extends farther from the Delta eastward along the shelf break (Figure 10).

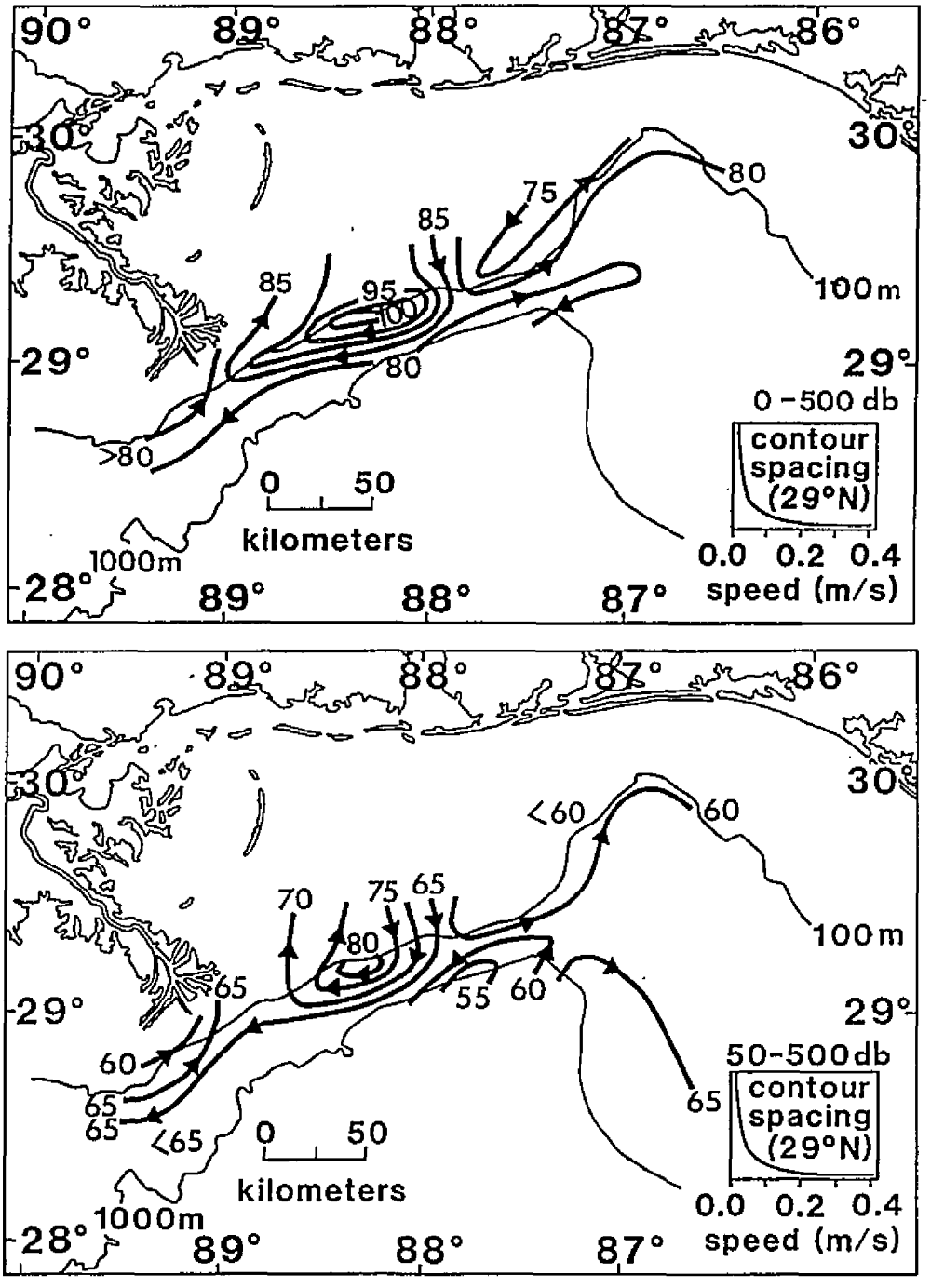

Figure 9. Annual mean dynamic height topography, 0/500 db, 50/500 db. Contours are in dynamic centimeters, arrows indicate direction of flow.

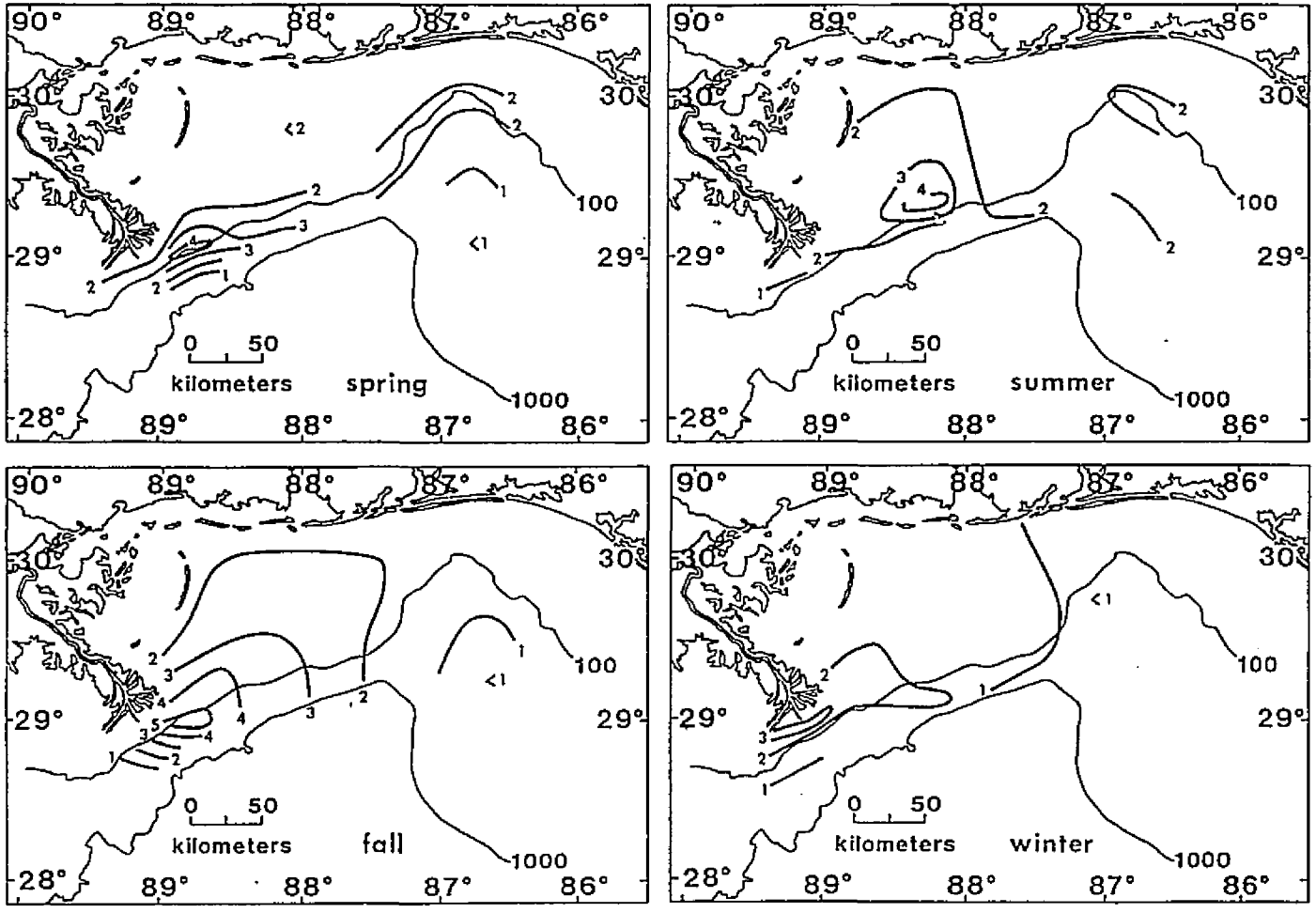

Figure 10. Seasonal fresh water content for the upper 100 m, spring (upper left), summer (upper right), fall (lower left), winter (lower right). Units are height of fresh water in meters.

The offshore and remaining shelf regions are characterized by similar fresh water contents to those found in the spring.

The change in fresh water content from the summer to fall, is principally due to landward dispersion (Figure 10). The highest values are found immediately east of the Delta, a steep gradient separates this tongue of high fresh water content from the very low content offshore. The gradient is much weaker east and landward of the high content region.

Winter fresh water content is the lowest of the four seasons. Highest content during winter occurs adjacent to the Delta, and moderate values extend eastward along the shelf break (Figure 10). Most of the shelf has low content and the De Soto Canyon region has even less.

DISCUSSION

The seasonal circulation of the region is not as simple as described by Leipper (1954). Shelf-scale circulation features do exist and they vary in strength and location.

Seasonal geostrophic circulation on the outer shelf and upper slope is anticyclonic around seasonally persistent dynamic topography centered on the shelf break and cyclonic around dynamic topography usually found at the head of De Soto Canyon. The flow generally tends to be parabathic or at small angles to the bathymetry, except at the eastern and western ends of the topographic high, where flow can be more normal to the bathymetry. The flow across the front of the

Delta is seasonal. Spring and summer flows are westward. Fall and winter flows are eastward.

Low dynamic heights near the head of De Soto Canyon are present seasonally. Cyclonic geostrophic flow occurs around these features. Such a dynamic low is clearly present in the spring topography. Geostrophic flow estimates are off the eastern LMAS and then southeastward along the eastern flank of the Canyon. The offshelf flow is indicated at a location where shelf-break exchange has not previously been reported.

The flow on the outer shelf and upper slope is a response to the fresh water discharge from the Mississippi River. Salinity controls the density in this region and the Mississippi River discharge controls the salinity, at least in the upper 100 m where most of the dynamic topography occurs. During spring, fresh water discharge disperses along the shelf break towards the east. This dispersion is also evident as a ridge of dynamic heights extending eastward from the Delta. Geostrophic circulation around this dynamic high in the vicinity of the Delta and over the outer shelf and upper slope continues through the fall. This ridge of dynamic height is separated from the Delta in the summer and begins to disperse over the shelf. Freshwater discharge at this time is much less than during the spring. High dynamic topography encompasses most of the shelf in the fall, circulation is anticyclonic over the outer shelf and upper slope. The great decrease in fresh water content between the fall and winter is evident by the greatly reduced dynamic

topography in the winter.

The spring and summer flow directed westward across the Mississippi Delta front has been observed in more than one study, as have eastward flow in fall and winter (Ichiye, 1960; Chew et al, 1962; Drennan, 1968; Molinari et al, 1979; Ebbesmeyer et al, 1982; Kindinger et al, 1982; Molinari and Mayer, 1982; Wiseman and Dinnel, 1988). Winter cyclonic circulation on the shelf proper (Drennan, 1968; Schroeder et al, 1987) is not corroborated by my analysis of the present data from the outer shelf. However, the winter season contained only 15% of the historical data. The results may not be as representative as for the other seasons.

An eastward current along the upper slope (Chew et al, 1962; Drennan, 1968) is not supported by this analysis. The presence of the Loop Current or an associated feature, may have been driving the eastward current described in the literature. Moored current meter records from the region suggest observed eastward flow is a Loop phenomenon (Molinari et al, 1979; Ebbesmeyer et al, 1982; Molinari and Mayer, 1982; and Wiseman and Dinnel, 1988).

Information derived from the seasonal dynamic heights is from averaged data. The patterns described are weighted to the times and locations of frequent data collection. It is believed that the incorporation of multiyear data will offset biases due to interannual variability or sampling scheme.

3. SEASONAL FLOW ON THE INNER SHELF

DATA

Data Description

Current meter data from eight locations on the inner shelf (Table 3, Figure 11) was acquired from the U.S. Army Corps of Engineers. Current speed and direction, and water temperature and salinity were measured during three deployments: 1 November 1980 to 9 January 1981, 21 March to 21 May 1981, 15 July to 13 August 1981. There were two meters on each mooring. One was 3 m below the air-sea interface and the other was 1.8 m above the water-sediment interface. These meters depths will be referred to as surface and bottom. Current meters will be referenced according to mooring and depth. For example, CM3S, refers to the surface meter at mooring 3. The reader should refer to Kjerfve and Sneed (1984), or the quality control reports from Raytheon (1981a, 1981b, 1981c), the field deployment company for additional information.

The quality of many of the records was questionable. Three sources were used to qualify a record for analysis, the quality control reports from Raytheon (1981a, 1981b, 1981c), preliminary data reports by Schroeder (1981a, 1981b, 1982), and visual examination of the raw time series themselves.

The salinity data were generally the least usable, although some meters had salinity data, which along with

Table 3. Locations of current meter moorings, coastal water level, bottom pressure, coastal and buoy wind stations.

Current Meter Station	Latitude Deg. N	Longitude Deg. W	Surface Meter Depth (m)	Bottom Meter Depth (m)	Station Depth (m)
CM1	30.15	89.86	3.0	9.4	11.3
CM2	30.08	88.72	3.0	11.0	12.8
CM3	30.17	88.64	3.0	11.9	13.7
CM4	30.17	88.38	3.0	12.8	14.6
CM5	30.05	88.28	3.0	17.7	19.5
CM6	30.21	88.19	3.0	9.8	11.6
CM7	30.01	88.12	3.0	20.1	21.9
CM8	30.05	87.91	3.0	14.9	16.8

Bottom Pressure	Latitude Deg. N	Longitude Deg. W	Station Depth (m)
DIWL	30.25	88.075	
P1	29.88	88.46	32.9
P2	29.88	88.083	32.9
P3	29.88	87.75	32.9

Wind Station	Latitude Deg. N	Longitude Deg. W
DI	30.249	88.077
BY	29.30	87.50

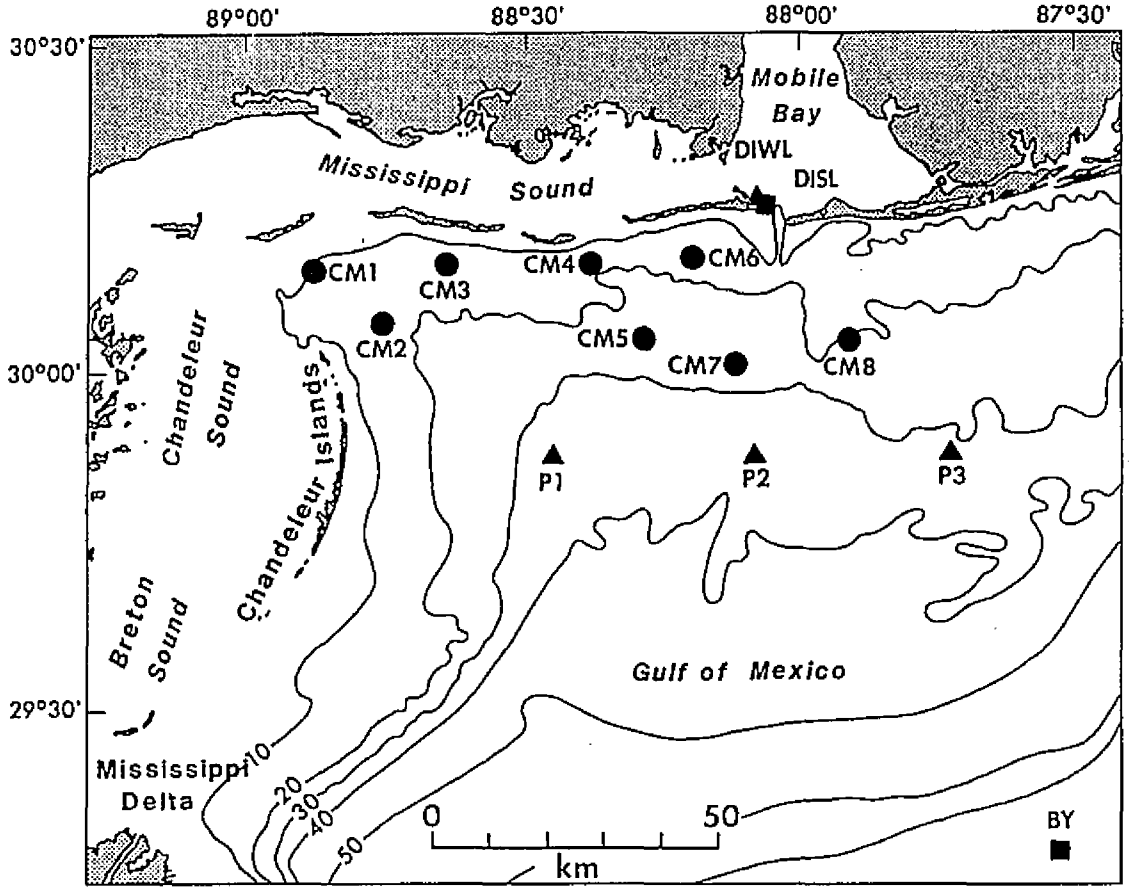

Figure 11. Station locations of current meters (CM), bottom pressure gauges (P), Dauphin Island winds (DISL), buoy winds (BY), and Dauphin Island water level (DIWL) in the study region.

temperature, served as a qualitative source of information concerning stratification. Salinity and temperature data from Kjerfve and Sneed (1984), for all three deployments, are described for CM8.

Hourly winds (DI) from Dauphin Island Sea Lab (DISL) and available half-hourly winds from National Data Buoy Office (NDBO) buoy 42009 (BY) (Table 3, Figure 11), were obtained. Those data which were concurrent with the current meter were used in the subsequent analyses. BY winds were not measured during the third current meter deployment.

Concurrent water level from a NOAA/NOS tide gauge at Dauphin Island (DIWL), #8735180, and bottom pressure measured at three locations (P1, P2, P3) on the shelf seaward of the current meters (Table 3, Figure 11), were also obtained. All gauges measured the total pressure. The data will be referred to as water level, for convenience. Dinnel and Schroeder (in press) found that water level data at Dauphin Island was highly coherent with water level data for the coastal Gulf of Mexico in this region. All water level and pressures were demeaned and detrended for subsequent analyses, because only DIWL was geodetically referenced.

Data Analysis

Speed and direction data, for both wind or currents, were converted to velocity components with $\underline{u}$, positive to the east and $\underline{v}$, positive to the north. Wind stress, $\underline{\tau}_w$, was

determined from the wind velocity, $\underline{U}$,

$$\tau_w = \rho_a C_d \underline{U}|\underline{U}|,$$

where ρ_a is a reference air density, C_d, is a drag coefficient determined after Amorocho and DeVries (1980, 1981). All currents, winds and wind stress have an oceanographic orientation.

All data sets were low-pass filtered in the frequency domain with a cutoff of 0.6 days, then resampled at 0.125 days. Data were Fast Fourier Transformed (FFT), the coefficients of those frequencies not desired were set to zero, and data were then inverse transformed to obtain a filtered time series. The subsequent analyses used the low pass filtered data, unless specifically noted otherwise.

Means and variances about the means were computed using standard formulae. Standard errors about the mean, SE, were estimated using the formula

$$SE = \frac{\langle s^2 \rangle^{1/2}}{(T/t_o)^{1/2}}$$

where $\langle s^2 \rangle^{1/2}$, is the rms speed of the low passed current record, T is the total record length, and t_o is the correlation time scale, estimated as the area under the normalized autocovariance function of each record, integrated out to the first zero crossing (Beardsley and Boicourt, 1981; Wiseman and Dinnel, 1988). The angle of rotation, θ, to the principal axes was computed using the

formula

$$\theta = \tan^{-1}\left[\frac{2S^2_{uv}}{S^2_u - S^2_v}\right]$$

where S^2_{uv}, S^2_u and S^2_v, are the covariance, and variances of the $\underline{u}$ and $\underline{v}$ velocity components, respectively.

Complex spectrum analysis

Current and wind stress data are treated as vector quantities in the time series analyses. The complex vector, $\underline{W}$, is the sum of two polarized components, $\underline{W}_1$, the east-west component (real) and $\underline{W}_2$, the north-south component (imaginary). Variance preserving autospectra are computed for these vector times series with a FFT program. Spectrum output consist of the magnitude squared of two counter-rotating vectors, or phasors, at discrete frequencies. The sum of the positive (counterclockwise rotation) and negative (clockwise rotation) spectra equals the total spectrum. The vector sum of the phasors at each frequency, is the hodograph of $\underline{W}$ at that frequency. When both phasors are of the same magnitude, the resultant motion is rectilinear. Cross-spectra between two vectors can also be estimated. An advantage to using vectors, complex inputs, is that the coherence is not dependent on the coordinate system (Gonella, 1972; Mooers, 1973).

Coherence-squared and phase were determined between two vector data sets, e.g. wind stress and current velocity or

current velocity at two locations.

Complex EOF analysis

Complex EOF analysis was performed with current and wind stress time series as input. A large number of investigators have used complex EOF analyses of geophysical data successfully (Hardy and Walton, 1978; Legler, 1983; Denbo and Allen, 1984, Servain and Legler, 1986, Wiseman et al., 1988). The following, brief discussion of the technique, primarily follows that of Hardy (1977).

A matrix, **S**, with complex elements, S_{nm}, has n = 1,N input complex time series vectors, each of m = 1,M values. In this analysis, m represents time, measured concurrently at all N inputs. $\mathbf{H} = 1/M\ \mathbf{S}\ \mathbf{S}^t$ defines a Hermitian matrix, **H**, of N x N elements. $\mathbf{S}^t$, is the complex conjugate transpose of **S**. **H** is composed of complex values except along the diagonals, which are real and proportional to the specific energy of each input. In the present analysis, the diagonals have been normalized in order to allow for nonsimilar inputs, i.e. currents and wind stress. **H** is analogous to a normalized variance-covariance or correlation matrix in scalar EOF analyses. In the present analysis I will refer to variances and covariances. These are, in truth, correlations. N real eigenvalues, λ_j, and N orthogonal eigenvectors, $\underline{E}_j$ exist satisfying

$$\mathbf{H}\ \underline{E}_j = \lambda_j\ \underline{E}_j \qquad j = 1,N$$

and

$$\underline{E}_i^t \, \underline{E}_j = \delta_{ij} \qquad i,j = 1,N.$$

$\underline{E}_j$ has complex elements. $\underline{E}_i^t$ is the complex conjugate transpose of $\underline{E}_i$. δ_{ij} is the Kronecker delta function. A fraction of the total variance in the data set is associated with each eigenvalue. This fraction can be determined as the ratio of the individual eigenvalues, to the sum of all the eigenvalues. Hardy and Walton (1978) referred to this ratio as a figure of merit. The ratio of any eigenvalue to the sum of the eigenvalues will be noted here as $\%S_t$,

$$\%S_t = \left(\lambda_k / \sum_{j=1}^{N} \lambda_j \right) \times 100, \qquad k = 1,N.$$

Let **E** be a 1 x N matrix containing eigenvectors of **H** and satisfying

$$\mathbf{E}_n \, \mathbf{E}^t{}_n = \mathbf{I}_n,$$

and let $\underline{S}_m$ be the m^{th} column of elements in **S**. $\underline{C}_{nm}$ is defined as

$$\underline{C}_{nm} = \mathbf{E}^t{}_n \, \underline{S}_m.$$

$\underline{C}_{nm}$ is a time series of m complex projection coefficients for the n^{th} mode, and is referred to as the n^{th} principal component.

Each eigenvalue is associated with a spatial pattern or mode. The eigenvalue is a measure of the percentage of the

total variance associated with this mode. The first mode, by convention, has the largest $\%S_t$ associated with its spatial pattern, the second mode has the next largest $\%S_t$, and so on. The normalized inputs used in this analysis allow determination of a level at which the $\%S_t$ associated with each mode can be statistically distinguished from that which would result from inputs of random noise (Overland and Preisendorfer, 1982).

Each mode has an eigenvector associated with it, which has complex elements, $\beta_j \exp(i\phi_j)$, where β will be referred to as a weight and ϕ will be referred to as a phase angle. The EOF algorithm only determines the eigenvectors to within an arbitrary rotation.

A meaningful orientation relative to the physical setting is desirable. Because of the invariant nature of the eigenvectors, the absolute phase angles within each mode need not have a physical meaning. Each principal component has an axis of preferred orientation, which is obtained by maximizing the energy in the projection of the principal component onto an N-dimensional vector of identical complex components (Appendix I). The orientation of these components is the desired rotation of the eigenvector. This enables an objective orientation of the entire eigenvector into one of two directions.

The eigenvalues are <u>mathematical</u> partitions of variance. The associated eigenvectors need not model a geophysical phenomenon. Great caution must be used when physically

interpreting these patterns.

Momentum balance analysis

The terms in the vertically-integrated horizontal momentum equations,

$$\frac{\partial U}{\partial t} + U\frac{\partial U}{\partial x} + V\frac{\partial U}{\partial y} - fV + g\frac{\partial \eta}{\partial x} - \frac{\tau_{sx}}{\rho_w H} + \frac{\tau_{bx}}{\rho_w H} = R_x$$

$$\frac{\partial V}{\partial t} + U\frac{\partial V}{\phi f} + V\frac{\partial V}{\partial y} + fU + g\frac{\partial \eta}{\partial y} - \frac{\tau_{sy}}{\rho_w H} + \frac{\tau_{by}}{\rho_w H} = R_y,$$

will be estimated. H is the water depth, η is the sea surface deviation from mean sea level, f is the coriolis parameter, g is the acceleration due to gravity, U and V are vertically-averaged speeds, and τ_s and τ_b are the surface and bottom stress, respectively. The flow is assumed to be barotropic because of the shallow water column. The residual terms, R_x and R_y, include the baroclinic pressure gradient terms and additional terms arising from the vertically-integrated, time-averaged advective terms. These latter terms are generalized Reynolds' stresses (Appendix II). The available data were inadequate for estimating either the baroclinic pressure gradient or the generalized Reynolds' stresses. Surface meter velocity components were taken as representative of the vertically-averaged velocity components, U and V. The barotropic pressure gradients, $g\partial\eta/\partial x$ and $g\partial\eta/\partial y$, were determined from the demeaned and detrended DI water level and bottom pressure data. The

barometric pressure field of synoptic weather systems was assumed to affect the entire region uniformly. The barotropic pressure gradients were evaluated as the slopes of planes fit to western (DIWL, P1 and P2) and eastern (DIWL, P2 and P3) pressure data sets. These were used to estimate momentum balances at current meter moorings CM5 and CM8. Positive alongshelf gradients mean pressure increases eastward and positive cross-shelf gradients mean pressure increases northward.

The surface stress is the wind stress (see above). The bottom stress, $\underline{\tau}_b$, was determined from a quadratic form using the bottom meter current velocity, $\underline{U}_b$, at CM5 and CM8.

$$\underline{\tau}_b = \rho_w C_b \underline{U}_b |\underline{U}_b| ,$$

where C_b is a bottom drag coefficient taken to be constant, 0.002, and ρ_w is a reference water density.

RESULTS

Deployment MS1

General Data Description

Eight current meters recorded usable data during the first deployment (MS1). Contemporaneous data over a 54.375 day record from 1800 CST 3 November to 2230 CST 28 December 1980 were used in the subsequent analyses. The concurrently available data from all the current meters is maximized using this record length.

Surface and bottom salinities at CM8 were fairly

constant, near 32 ppt, except for four five-day periods of vertical stratification. Temperatures, near 22° C in early November, dropped during November to near 18°C, where they remained during December. The estimated record means for salinity and temperature were used to calculate a reference density of 1023 kg/m^3. During periods of vertical stratification, the surface to bottom salinity and temperature differences were approximately 3 ppt and 2° C. Surface to bottom density differences, calculated from salinity and temperature values (Kjerfve and Sneed, 1984), were then approximately 3-4 kg/m^3. At times of stratification, the cross-shore velocity components at the surface and bottom meters were likely to be in opposite directions.

Velocity statistics are presented in Table 4. The velocity means and standard errors are graphically depicted in Figure 12. The principal axes of the low-passed currents are plotted in Figure 13.

The velocity means are considered statistically significant when they exceed two standard errors. Most of the current data sets had a statistically-significant component. The records from CM1B and CM5B do not. Only half the current records had statistically significant cross-shelf components. Three of these were northward.

Table 4. Flow statistics for MS1 current meter component means, $\underline{u}$, $\underline{v}$ ($\times 10^{-2}$ m/s), low passed variances S^2_u and S^2_v ($\times 10^{-4}$ m^2/s^2), correlation time scales, t_{ou}, t_{ov} (d), standard errors, SE_u, SE_v ($\times 10^{-2}$ m/s), and rotation angle of principal axes, θ (deg).

CM	$\underline{u}$	$\underline{v}$	S^2_u	S^2_v	t_{ou}	t_{ov}	SE_u	SE_v	θ^+
1B	-0.21	-0.23	33.98	5.06	0.75	0.81	0.69	0.27	0.43
2S	-2.67*	-3.07*	28.09	46.84	0.61	1.21	0.56	1.02	25.10
2B	-1.01*	0.63	9.92	38.64	0.88	1.17	0.40	0.91	16.11
3S	-7.07*	2.08*	79.58	26.40	1.52	1.11	1.49	0.73	-22.33
5S	-8.21*	3.51*	157.03	43.51	1.16	1.07	1.83	0.93	-20.88
5B	-0.94	1.63*	59.59	17.34	1.42	0.72	1.25	0.48	17.39
8S	-5.54*	0.88	91.19	89.90	1.18	1.44	1.41	1.54	-44.75
8B	-4.73*	0.64	64.45	15.72	1.26	0.64	1.22	0.43	-8.06

+ Positive angle measured counterclockwise.

* Statistically significant at the 95% level, i.e. larger than 2 SE.

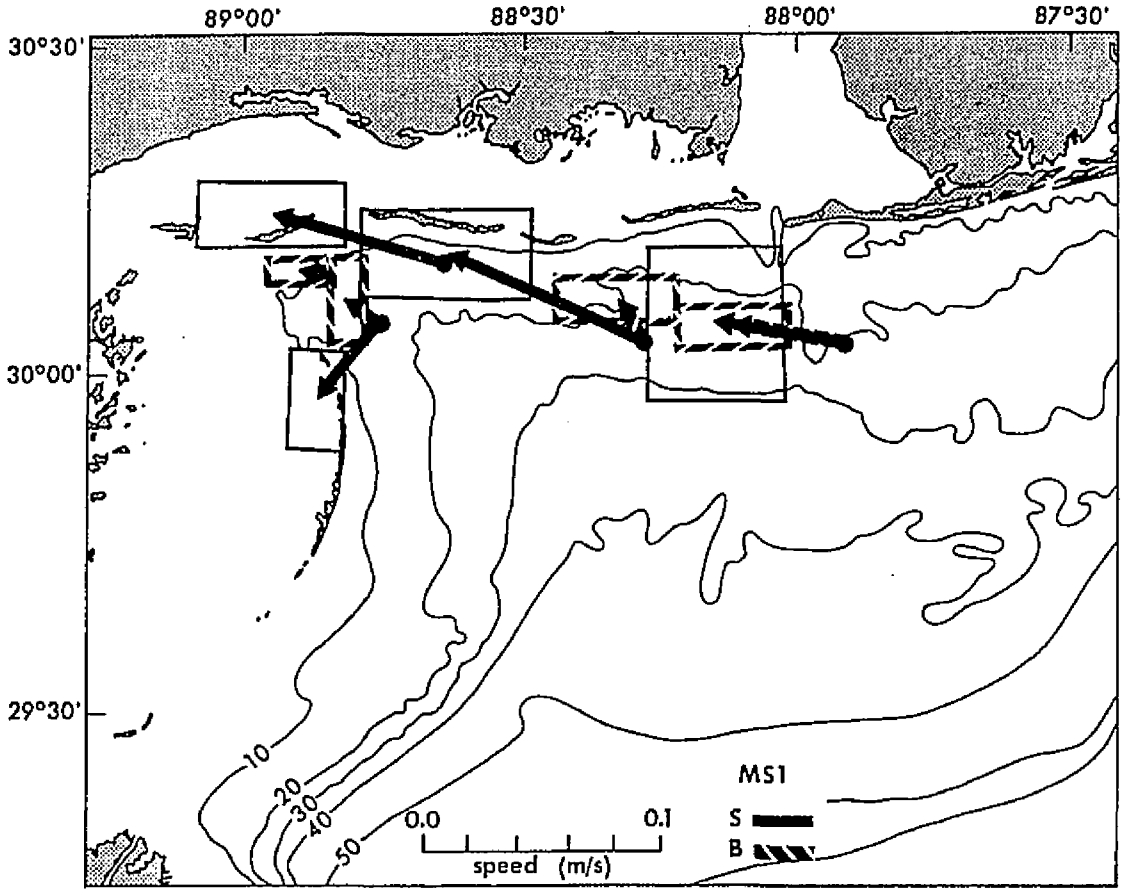

Figure 12. Current meter components mean speeds and standard errors for MS1. Boxes are ± 2 standard errors about the means.

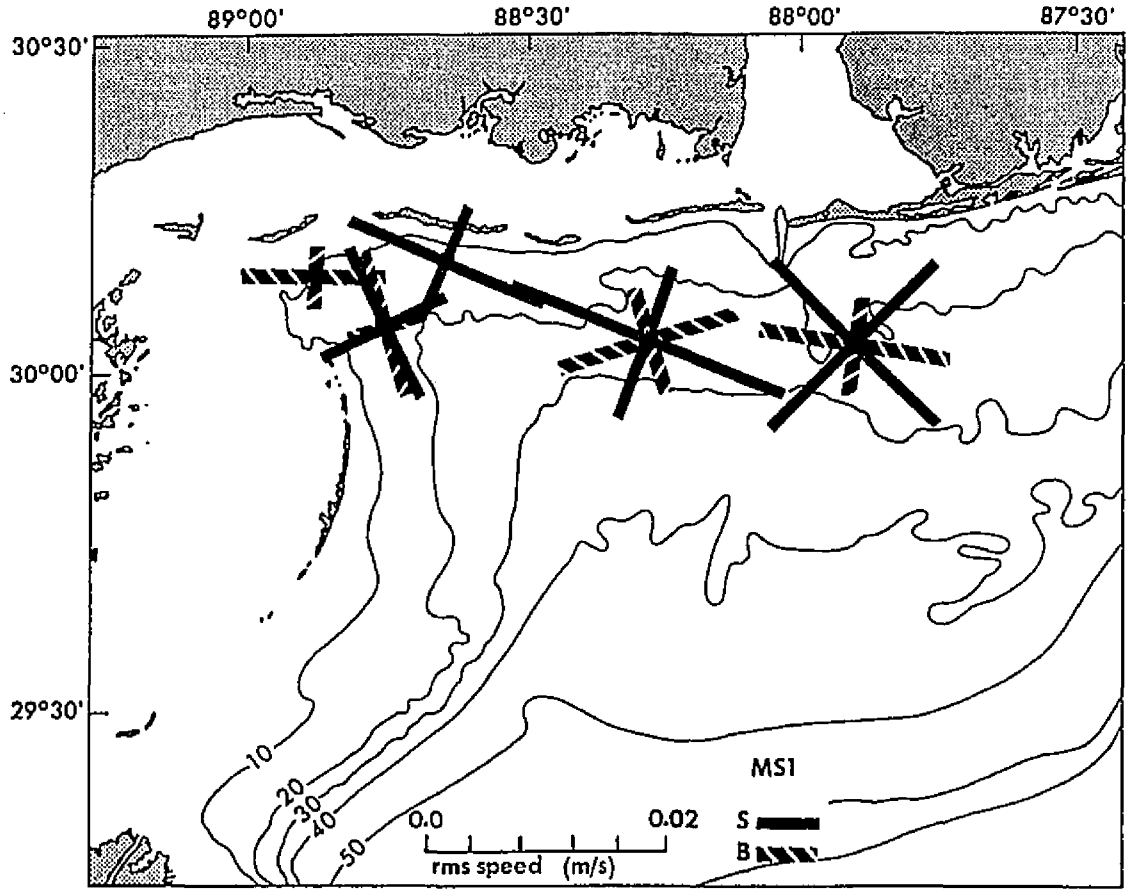

Figure 13. Current meter low passed principal axes for MS1. Length of axes are the rms values along the principal axes.

The data set from CM2S had a statistically-significant mean flow to the southwest. This flow is parabathic. The mooring is located near the apex of the bend of the inner shelf bathymetry. Mean flow at CM2B was to the west into Chandeleur Sound and statistically-significant. Mean flow at CM3S and CM5S was statistically-significant northwestward, toward the corner region. A similar pattern is also apparent in Figure 13. All major axes are oriented toward the northwest. The rms speeds of the records from the lower meters on the three moorings with both surface and bottom meters were smaller than those of the records from the upper meters. The major axes at CM5 and CM8 deflect to the left with depth as would be appropriate to Ekman veering. Subtidal currents at CM2 were deflected to the right with depth.

Visual inspection of the surface and bottom current records detected episodes of coherent flow. Energetic episodes of alongshore current reversals, with speeds up to 0.3 m/s occurred throughout the entire deployment area. Currents at CM8 were mostly oriented west-northwest or east-southeast (Figure 14). Similar orientation was observed at CM3 and CM5. Currents at CM2 were mostly oriented south-southeast or north-northwest (Figure 14). The former orientation is representative of a counterclockwise flow around the corner on the inner shelf. The latter orientation is representative of clockwise flow. Bottom currents at CM8 were similar to surface currents when inner shelf flow was

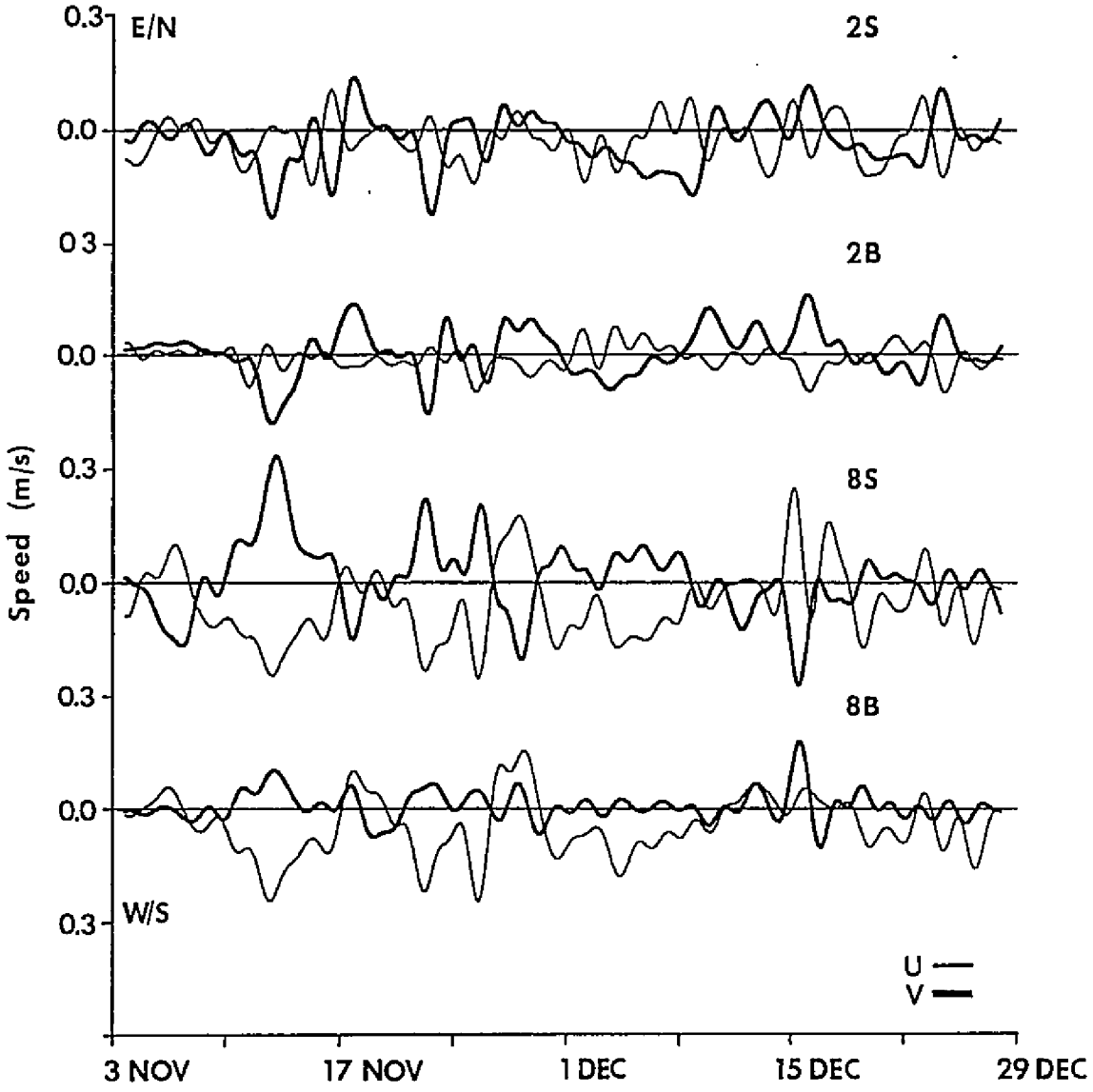

Figure 14. Current meter time series for MS1. Surface and bottom velocity components for CM2, surface and bottom velocity components for CM8. The velocity component, u, (light) is positive east; v, (dark) is positive north.

counterclockwise. When flow was clockwise, the bottom across-shelf component was opposite to the surface component, i.e. when the surface flow was east-southeast the bottom flow was east-northeast. Bottom flow at CM2 was usually very similar to the surface direction. Currents at CM1B (not shown) fluctuated in an east-west direction, in and out of the back barrier sounds through the pass at the north end of the Chandeleur Islands. The flow at CM1B was generally eastward when inner shelf flow was counterclockwise and westward when the inner shelf flow was clockwise.

Coastal winds, DI, and shelf break winds, BY, were very similar throughout the deployment. Wind shifts at BY lagged those at DI by approximately 1.5 hours and the wind direction at BY was rotated 11^{o} clockwise of that at DI.

Winds from the north were most prevalent during November and December 1980 (Figure 15). Some easterly or westerly components were also present. Very few winds blew from the south. These statistics are similar to 11-year monthly-composite wind roses for November and December (Schroeder and Wiseman, 1985).

Pressure at P1, P2, P3 and DIWL generally rose and fell in unison. DIWL was higher than the other records at high stands and lower at low stands. Large amplitude, $\pm$0.2 m, spatially-coherent fluctuations with periods on the order of 10 days were observed in the first half of the record. Smaller amplitude, $\pm$0.1 m, and less coherent fluctuations of

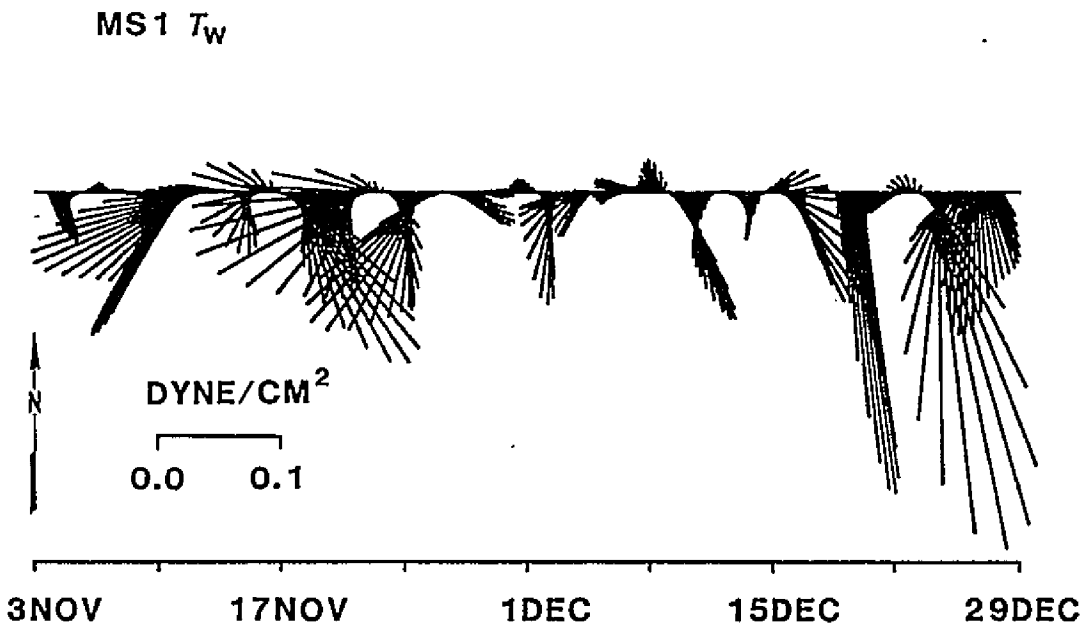

Figure 15. Stick plot of DI wind stress for MS1.

shorter periods occurred during the latter half of the record. Bottom pressures responded to frontal passages. Pressure increased coherently at all gauges prior to frontal passage and immediately dropped after passage. Exceptions were noted on 15 December and 24 December when changes at DIWL were out of phase with those on the inner shelf.

Complex Spectrum Analysis

Local wind stress spectra from DI were roughly bimodal. Greatest energy was found in frequency bands from 0.04 to 0.13 and 0.2 to 0.35 cycles per day (cpd) (Figure 16). BY wind stress spectra were similar to, but had a greater magnitude than, DI wind stress over most low-passed frequencies. Spectrum estimates at frequencies less then 0.075 cpd were computed from less than four periods of repetition and therefore have very low statistical reliability. Complex spectra are most energetic at negative frequencies (clockwise rotating winds), especially in the bands from 0.08 to 0.13 and 0.2 to 0.35 cpd. This is expected because of wind rotation related to frontal passages (Huh et al, 1984) and frontal frequencies (Dimego et al, 1976; Henry, 1979). Coherence squared between DI and BY wind stress is statistically-significant, at the 95% level, in the energetic frequency bands. The wind stress is coherent over the spatial scales of the LMAS shelf.

Complex spectra of data from CM8 (Figure 17), are most energetic at frequencies below 0.11 cpd. The other current

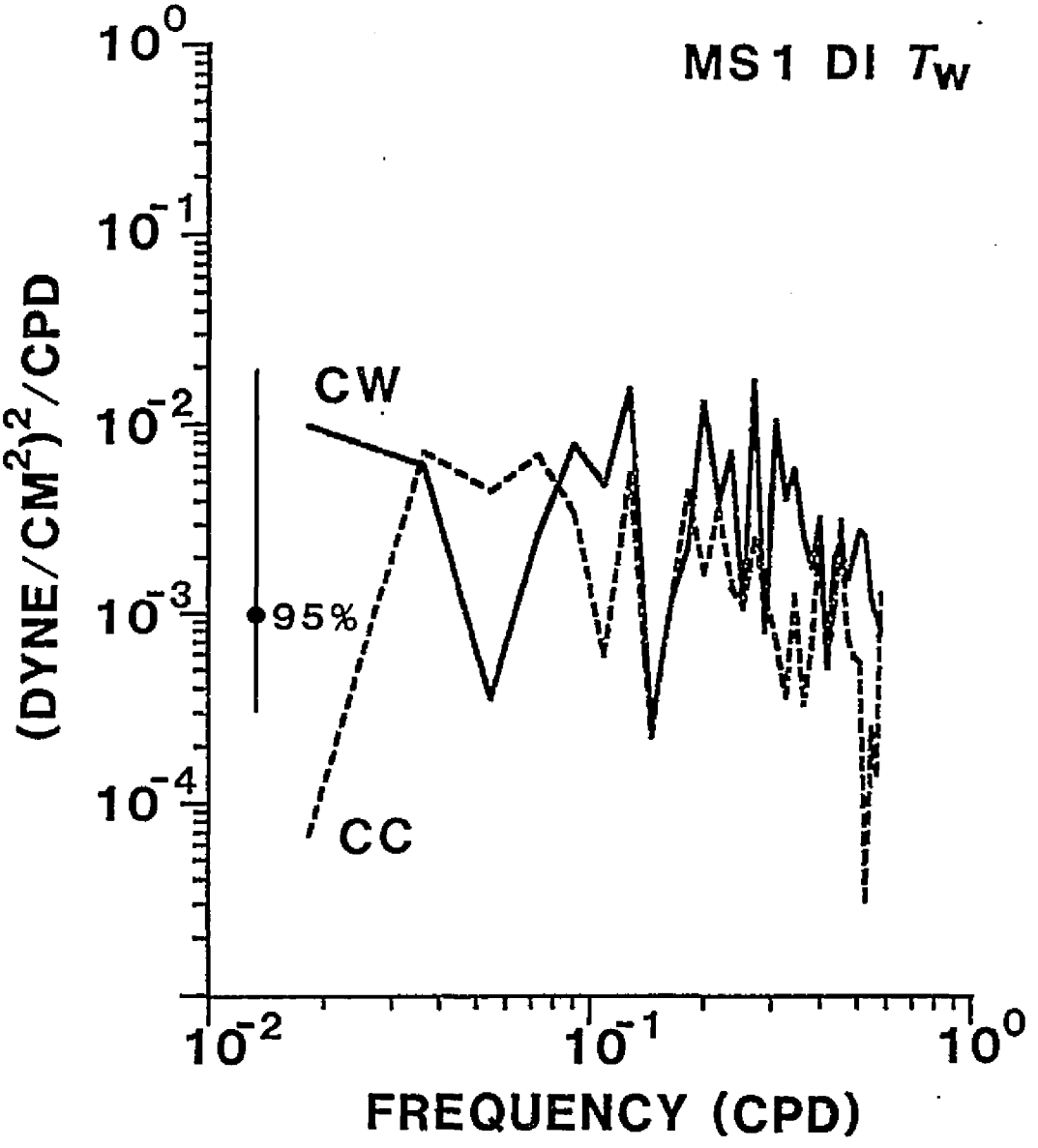

Figure 16. Complex DI wind stress spectra for MS1. Degrees of freedom are 4.

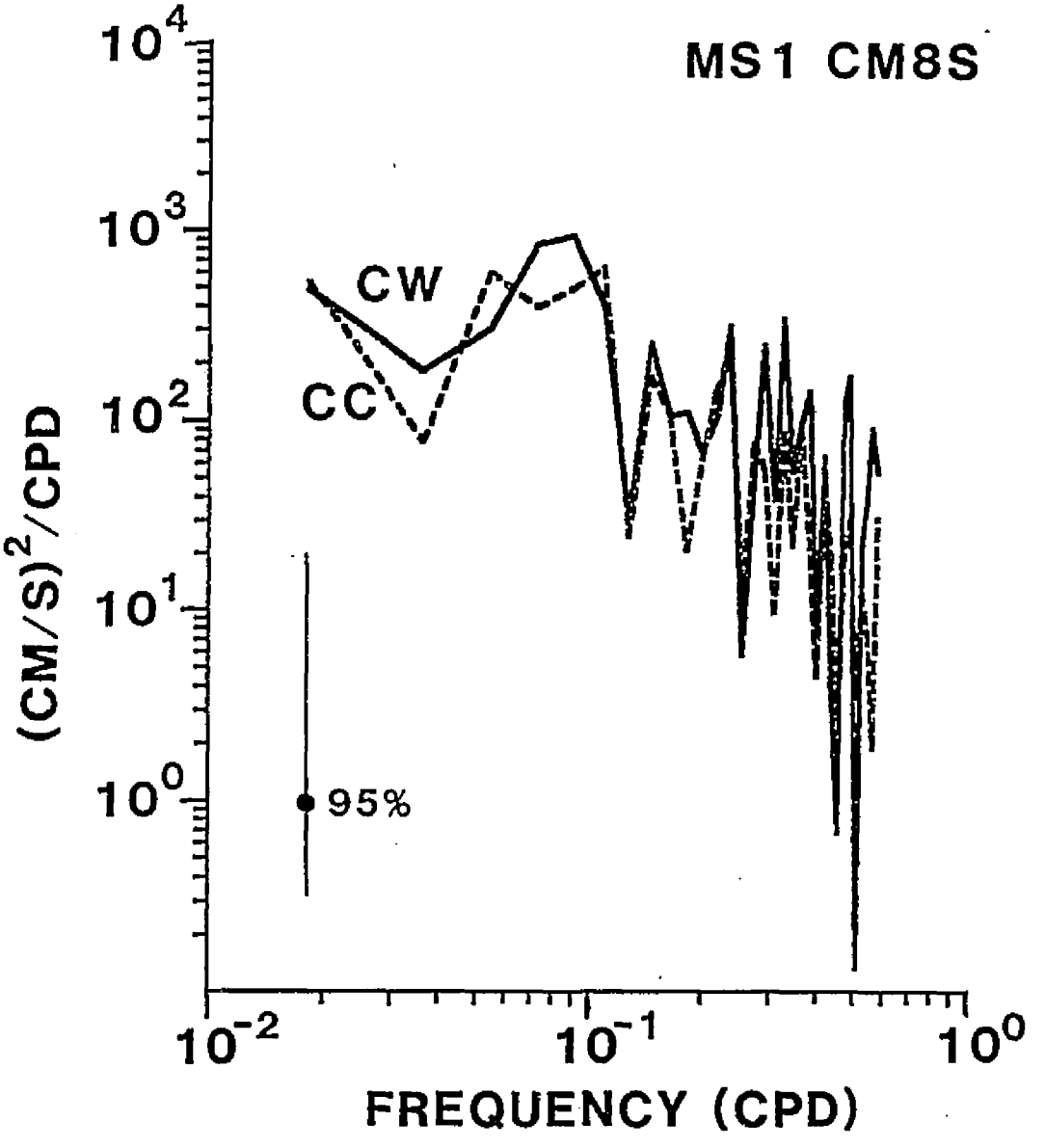

Figure 17. Complex current meter spectra from CM8S for MS1. Degrees of freedom are 4.

meter spectra are similarly distributed. Most current meter spectra are dominated by clockwise motion in the 0.2 to 0.35 cpd band. Relatively equal phasor magnitude or a counterclockwise dominance, which may indicate topographic influence characterize the spectra from CM1 and CM2. The energetic motions near 0.1 cpd are approximately rectilinear. Surface spectra are slightly more energetic than bottom spectra. Coherence-squared between surface and bottom meters at CM8 (Figure 18), is statistically-significant at frequencies less than 0.2 and 0.1 cpd for the clockwise and counterclockwise phasors, respectively, and between 0.21 and 0.45 cpd for the counterclockwise phasor.

Local wind-driven currents will be coherent with the local wind stress in the frequency bands where both the wind stress and currents are energetic. The wind stress spectra for both DI and BY were used in cross-spectrum analyses with current meter data. Both analyses produced similar relationships, so only those using DI will be presented.

The current spectra from CM1 and CM2 were coherent with the DI wind stress near $\pm$0.3 cpd and near 0.1 cpd for the counterclockwise phasor. The currents measured furthest from the coastal islands showed highest coherence at the lower frequencies, near 0.1 cpd, with both wind stress phasors, e.g. Figure 19, supporting the contention of rectilinear motion.

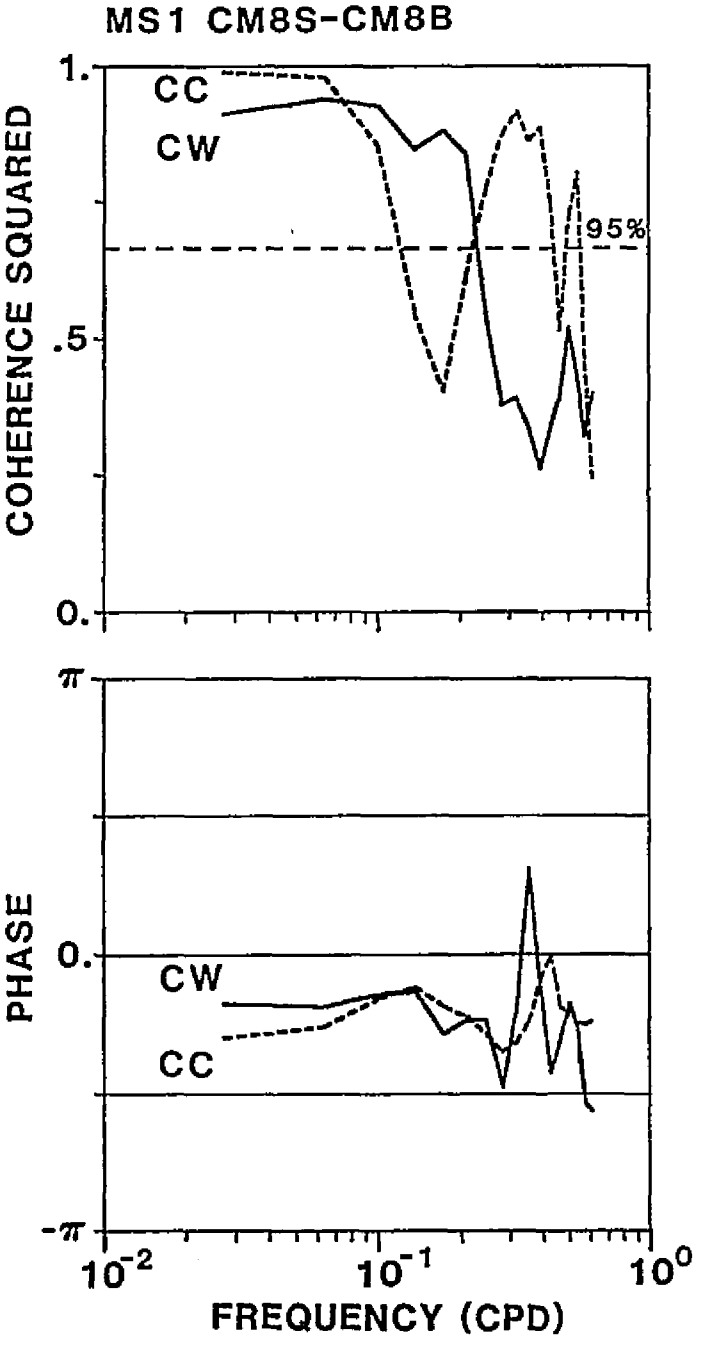

Figure 18. Complex coherence-squared and phase between surface and bottom current meters at CM8 for MS1. Positive phase indicates bottom meter lags surface meter. Degrees of freedom are 8.

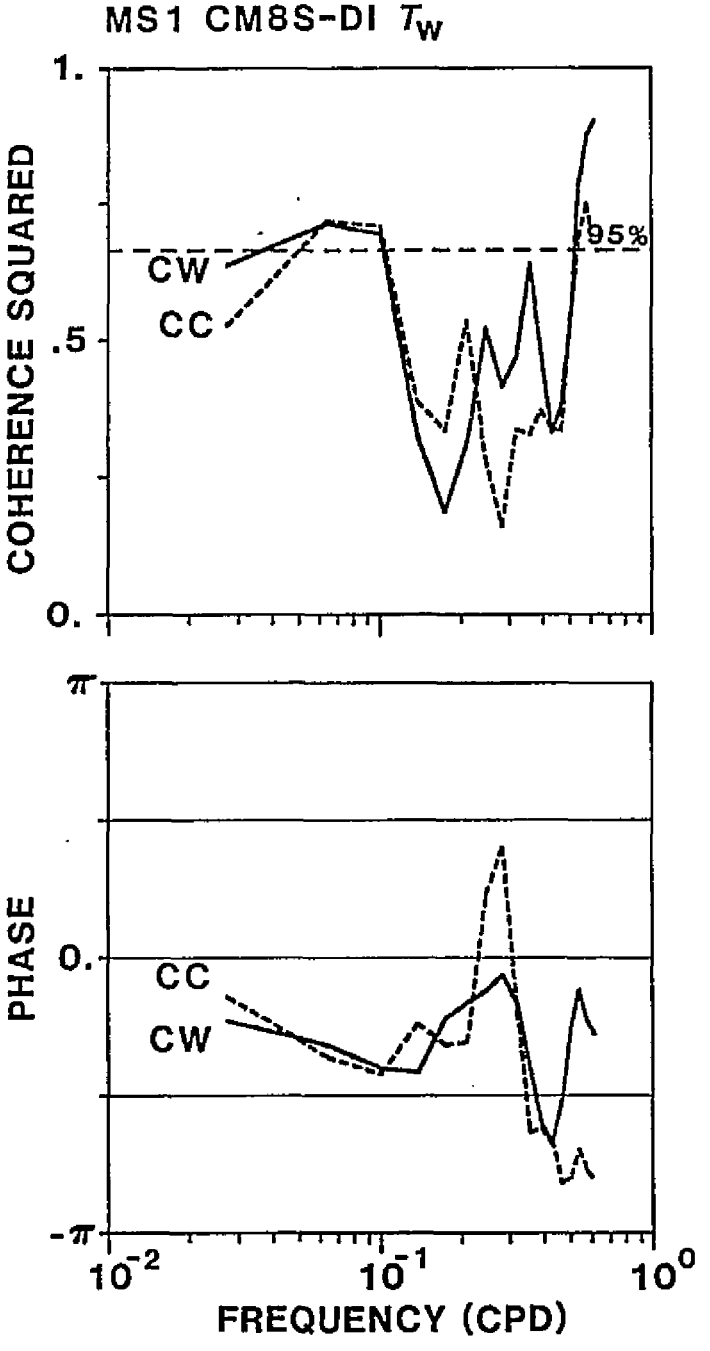

Figure 19. Complex coherence-squared and phase between surface currents at CM8 and DI wind stress for MS1. Positive phase indicates surface currents lag wind stress. Degrees of freedom are 8.

Complex EOF Analysis

Complex EOF analyses were performed using current velocities alone, current velocities and DI wind stress, current velocities and BY wind stress, and current velocities and both DI and BY wind stress as inputs. The statistics and patterns were very similar for each of the input groups (Appendix III). The EOF results using currents and DI wind stress are presented in Table 5. This analysis indicates that 2 modes were statistically different from random noise and account for 75% of the total variance. The magnitude of the first mode fluctuated with about a five day period during the first half of the record. The second mode usually peaked as Mode 1 was rapidly changing magnitude or direction. Mode 2 was dominant during the latter two weeks of the record when the magnitude of Mode 1 was never as high as earlier in the record.

Mode 1 describes 58% of the total variance and has high individual weights associated with most of the current records and low weights associated with the wind stress. The exceptions relatively low weight associated with currents at CM1B, and moderate weight associated with currents at CM2S. After rotation to a preferred orientation, the pattern of variation is consistent with east-west flow variations at CM3, CM5 and CM8, north-south flow variations at CM2, and small east-west flow variations into and out of Chandeleur Sound, and an east-west wind stress variation (Figure 20). This is the general clockwise-counterclockwise current

Table 5. Complex empirical orthogonal function statistics: percent total variance, $\%S_t$, 95% significance level, angle of preferred orientation, ψ, individual weights, β, phase angles, ϕ, and percent individual variance, $\%S_i$, for MS1. Inputs were current meters and DI wind stress.

	Mode 1	Mode 2
$\%S_t$	53.10	21.69
95% S.L.	14.96	13.67
ψ^+	-26	-22

Inputs	β	ϕ^+	$\%S_i$	β	ϕ^+	$\%S_i$
CM1B	0.16	-26	12	0.55	171	60
CM2S	0.28	-108	38	0.46	134	41
CM2B	0.35	-83	60	0.23	113	10
CM3S	0.37	153	65	0.22	160	10
CM5S	0.35	157	60	0.20	164	8
CM5B	0.40	-161	76	0.08	27	1
CM8S	0.41	132	78	0.16	-173	5
CM8B	0.39	173	74	0.08	-161	1
DIT_W	0.18	-177	15	0.55	-102	58

$^+$ Positive angles measured counterclockwise from positive x axis.

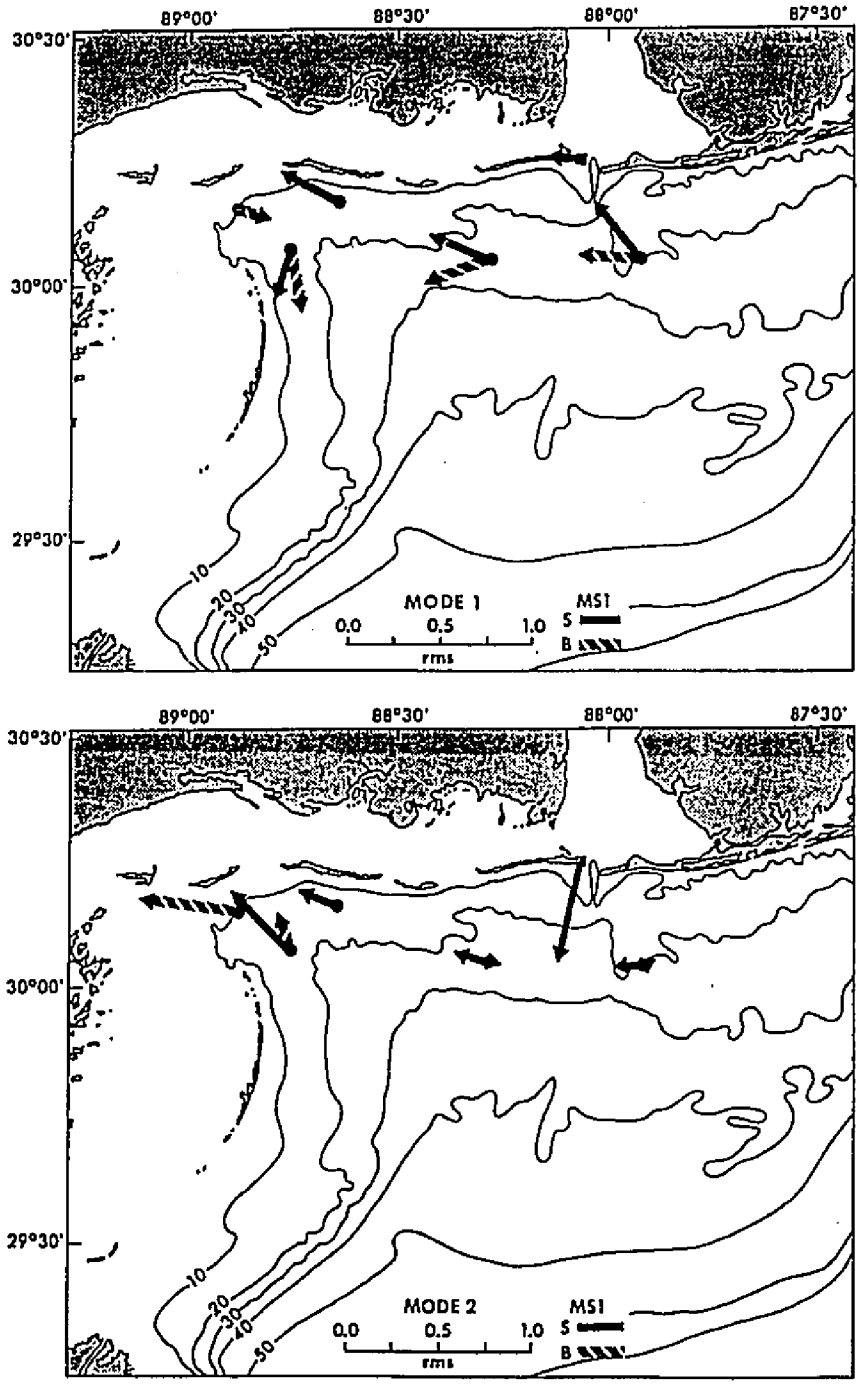

Figure 20. Complex EOF principal-component eigenvectors rotated to a preferred orientation, Mode 1 (upper) and Mode 2 (lower), for MS1.

variability described in an earlier section. The Mode 1 principal component variance ellipse is highly elongated parallel to the isobaths (Figure 21).

Mode 2 describes 22% of the total variance, less than half the variance associated with the first mode. The second mode has high individual weights associated with currents at CM1B and wind stress, moderate weights for currents at CM2S, and low weights for currents at CM2B, CM3, CM5, and CM8. Mode 2 accounts for the largest percent of the DI wind stress variation, 58%. The principal component variance ellipse (Figure 21) for Mode 2 is more isotropic variation than that of Mode 1. The complex components associated with CM1B and $\underline{T}_w$ are oriented roughly 90° apart (Figure 20). A southward wind stress is associated with a westward bottom flow into Chandeleur Sound. A northward wind stress is associated with an eastward bottom flow out of Chandeleur Sound. These are the wind stress directions of post and pre-frontal winds.

Mode 1 is consistent with a barotropic flow. There is generally a similar orientation between surface and bottom meters, with leftward current deflections of 25° to 40° in the bottom layer. In Mode 2 data from CM2 and CM8 are again consistent with a barotropic flow, but surface and bottom currents at CM5 are 150° apart, almost a complete reversal. This is anomalous compared to the results from other meters and is suggestive of baroclinic flow at this site.

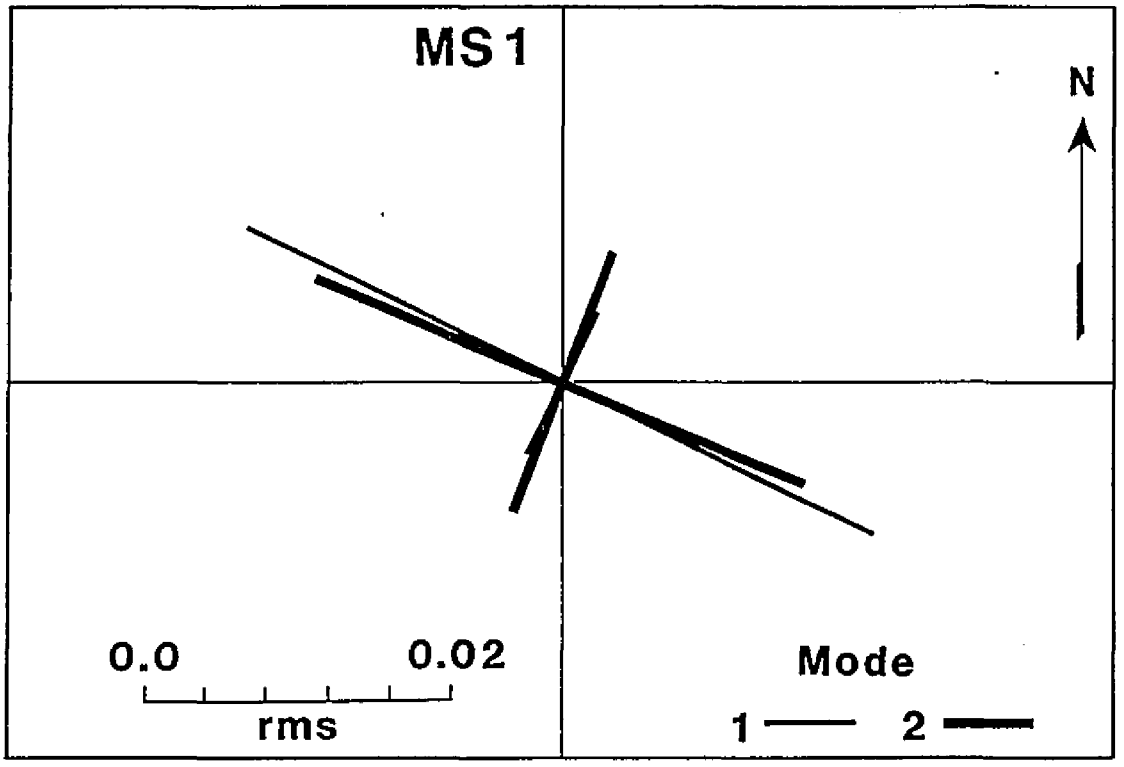

Figure 21. Rms values of principal component coefficients, Modes 1 and 2, for MS1.

Inner Shelf Momentum Balance

The western and eastern barotropic pressure gradient estimates are characteristic of moorings CM5 and CM8, respectively. Because of the limited reliable surface current meter, the velocity gradients were estimated from surface meters CM3, CM5, and CM8. The alongshelf velocity gradients are more reliable than the cross-shelf velocity gradients.

The estimated terms in the alongshelf momentum balance at CM5 and CM8 were very similar. They were not in balance! The rms values for the local time derivative, the cross-shelf field acceleration, the coriolis force, the pressure gradient force, and the surface and bottom stress terms were large (Table 6). Each of the may be important to the total balance. The pressure gradient and the coriolis terms are the most energetic terms. Although usually of the proper sign for balance, the pressure gradient and coriolis terms were unequal in magnitude (Figure 22). Over the first two thirds of the record the pressure gradient was insufficient to balance the coriolis term, regardless of the direction of flow. In the latter third of the record, the pressure gradient became very large and the coriolis term was too small to balance.

The across-shelf momentum equation is also dominated by the barotropic pressure gradient and the coriolis terms (Table 6, Figure 22). The pressure gradient is the dominant

Table 6. Rms values of momentum balance terms, in both alongshelf and cross-shelf directions, for CM5 and CM8 of MS1. Units are m/s^2 ($x10^{-7}$).

	Alongshelf						
	$\frac{\partial U}{\partial t}$	$U\frac{\partial U}{\partial x}$	$V\frac{\partial U}{\partial y}$	fV	$g\frac{\partial \eta}{\partial x}$	$\frac{\tau_{sx}}{\rho H}$	$\frac{\tau_{bx}}{\rho H}$
CM5	17.97	5.24	12.18	48.08	37.51	17.46	11.68
CM8	15.97	2.12	14.21	69.12	35.41	20.26	16.49

	Across shelf						
	$\frac{\partial V}{\partial t}$	$U\frac{\partial V}{\partial x}$	$V\frac{\partial V}{\partial y}$	fU	$g\frac{\partial \eta}{\partial y}$	$\frac{\tau_{sy}}{\rho H}$	$\frac{\tau_{by}}{\rho H}$
CM5	12.68	4.05	9.47	91.35	148.48	25.71	6.05
CM8	14.01	2.74	9.99	69.61	148.44	29.84	6.81

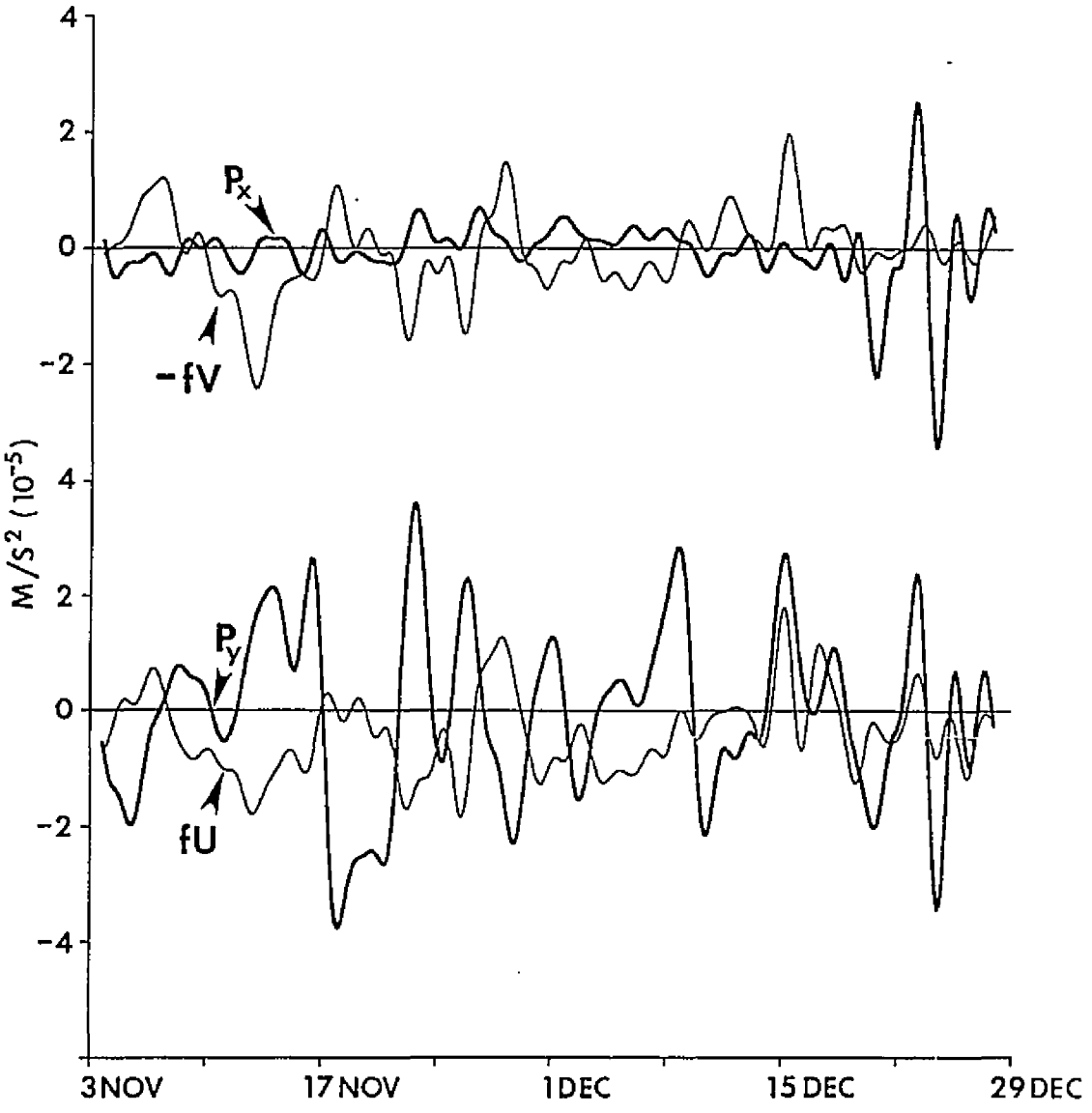

Figure 22. Alongshelf (upper) and across-shelf (lower) momentum equation terms for CM8S from MS1.

term. The coriolis term does not have the appropriate magnitude to fully balance it. Over the latter third of the record, the currents become 180^{o} out of phase with those needed to balance the pressure gradient. The surface stress, at times of interfrontal winds, begins to contribute to a total balance.

The currents appear to lead the pressure gradient by 1 to 2 days. This is the same time delay by which the pressure gradient lags the wind stress. The currents, then, are in phase with the wind stress and may have a directly driven portion as well as a portion in geostrophic balance with the pressure gradient. An attempt to balance the pressure gradient, coriolis and surface stress terms, though, also produced large residuals.

Discussion

A statistically-significant, counterclockwise mean flow of 0.05 to 0.08 m/s, westward along the Mississippi-Alabama barrier islands and southward along the Chandeleur Islands, was present over the inner shelf from 3 November to 28 December. Cold front passages were associated with major changes in the wind field. The wind variance was large near frequencies of 0.1 cpd. The current fluctuations were coherent with the winds at these same time scales. The currents were also spatially coherent at these time scales. These current fluctuations attained speeds of $\pm$0.1 m/s and flowed roughly parallel the isobaths. When winds were from

the east or south, currents flowed counterclockwise around the northwest corner of the inner shelf. When winds were from the northwest, currents flowed clockwise around this region.

DEPLOYMENT MS2

General Data Description

The data return was the best (13 current meters) during the second deployment (MS2). Concurrent data was available during a 46.5-day period from 1800 CST 26 March 1981 to 0600 CST 12 May 1981. Wind stress from DI and BY, DIWL, and water pressure at P2 and P3 were, also, obtained for this time period.

The salinity data were the least usable time series. The salinity and temperature data at CM8 (Kjerfve and Sneed, 1984) were used to estimate the range of salinity and temperature and to estimate periods of stratification. The water column was vertically homogeneous with salinities and temperatures of near 33 ppt and 17^{o} C at the beginning of MS2. Salinities freshened to near 28 ppt and temperatures increased to near 23^{o} C. The water column was vertically homogeneous during the first two weeks of the record. The surface and bottom salinities and temperatures diverged over the rest of the record. The period of greatest stratification occurred near the end of the record. The surface to bottom density difference was approximately 5 kg/m^{3} at that time.

Tabular (Table 7) and pictorial (Figure 23) representations of flow statistics have been prepared. Statistically-significant eastward mean flow, out of the Chandeleur Sound occurred at CM1S and CM2S. Statistically-significant mean eastward flow was generally observed near the Mississippi-Alabama barrier islands. Further offshore, the mean flow was generally northward, but not always statistically-significant.

The principal axes of the low passed currents are oriented primarily along-isobath (Figure 24). The bottom meter low-passed current fluctuations are oriented slightly to the left of those from the surface meters. The cross-shelf rms speeds are usually much smaller than the alongshelf rms speeds. Substantial reduction in velocity variance occurs with depth at the four moorings with surface and bottom meters.

The flow at CM2S (Figure 25) alternates between northwesterly and southeasterly with magnitudes of approximately 0.3 m/s at time scales of about five days. The bottom currents are predominantly north-northwesterly or south-southeasterly and usually in opposition to the surface flow. Alternating alongshore surface currents at CM8 (Figure 25), primarily toward the west-northwest or east-southeast, reach magnitudes greater than 0.3 m/s in the latter half of the record, but only 0.2 m/s over the first half of the record. The bottom currents at this station are much less than 0.15 m/s over the entire record. the surface currents

Table 7. Flow statistics for MS2 current meters component means, $\underline{u}$, $\underline{v}$ ($\times 10^{-2}$ m/s), low passed variances s^2_u and s^2_v ($\times 10^{-4}$ m^2/s^2), correlation time scales, t_{ou}, t_{ov} (d), standard errors, SE_u, SE_v ($\times 10^{-2}$ m/s), and rotation angle of principal axes, θ (deg).

CM	$\underline{u}$	$\underline{v}$	s^2_u	s^2_v	t_{ou}	t_{ov}	SE_u	SE_v	θ^+
1S	7.94*	-0.21	95.64	39.67	1.09	0.86	1.49	0.86	-14.16
1B	-0.13	-1.61*	32.06	14.09	0.81	0.70	0.75	0.46	3.86
2S	3.14*	-1.69	65.55	183.33	1.13	1.22	1.26	2.20	17.21
2B	0.23	0.24	13.67	59.22	0.65	0.88	0.44	1.06	20.68
3S	5.27*	1.80	142.30	36.67	1.36	1.19	2.04	0.97	-8.41
4S	-1.46	3.69*	193.00	77.26	1.08	0.72	2.11	1.10	-23.91
4B	0.31	0.94*	17.90	4.28	0.63	0.55	0.49	0.23	-9.09
5S	-1.29	2.03	98.29	93.50	1.17	1.26	1.57	1.59	-43.50
6S	5.37*	0.42	66.85	22.79	0.99	1.29	1.19	0.80	-25.10
6B	2.59*	1.69*	28.24	11.31	0.83	0.59	0.71	0.38	9.78
7S	0.95	1.91*	117.67	30.21	1.64	1.40	2.04	0.95	-15.58
8S	0.45	2.60*	144.74	55.19	1.45	0.98	2.13	1.08	-10.77
8B	0.25	-0.42	17.99	11.17	1.16	0.92	0.67	0.47	32.64

+ Positive angle measured counterclockwise.

* Statistically significant at the 95% level, i.e. larger than 2 SE.

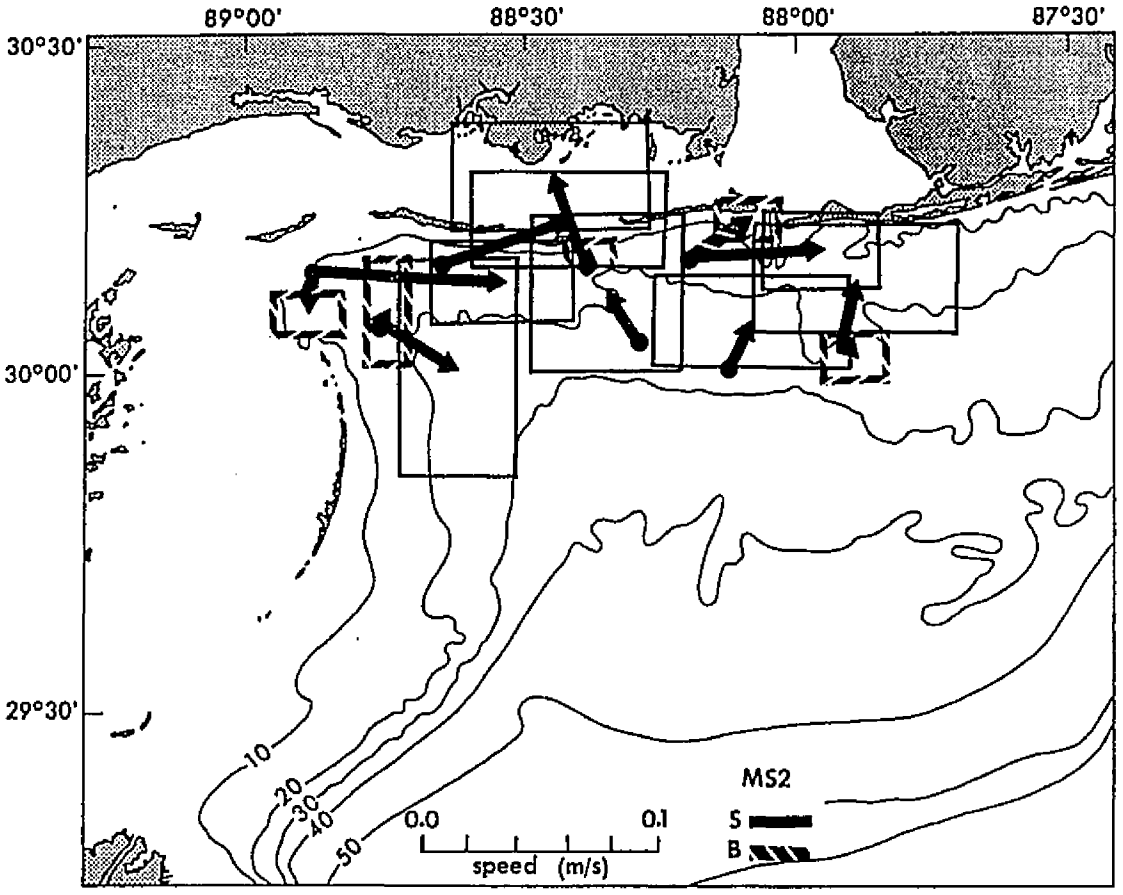

Figure 23. Current meter components mean speeds and standard errors for MS2. Boxes are ± 2 standard errors about the means.

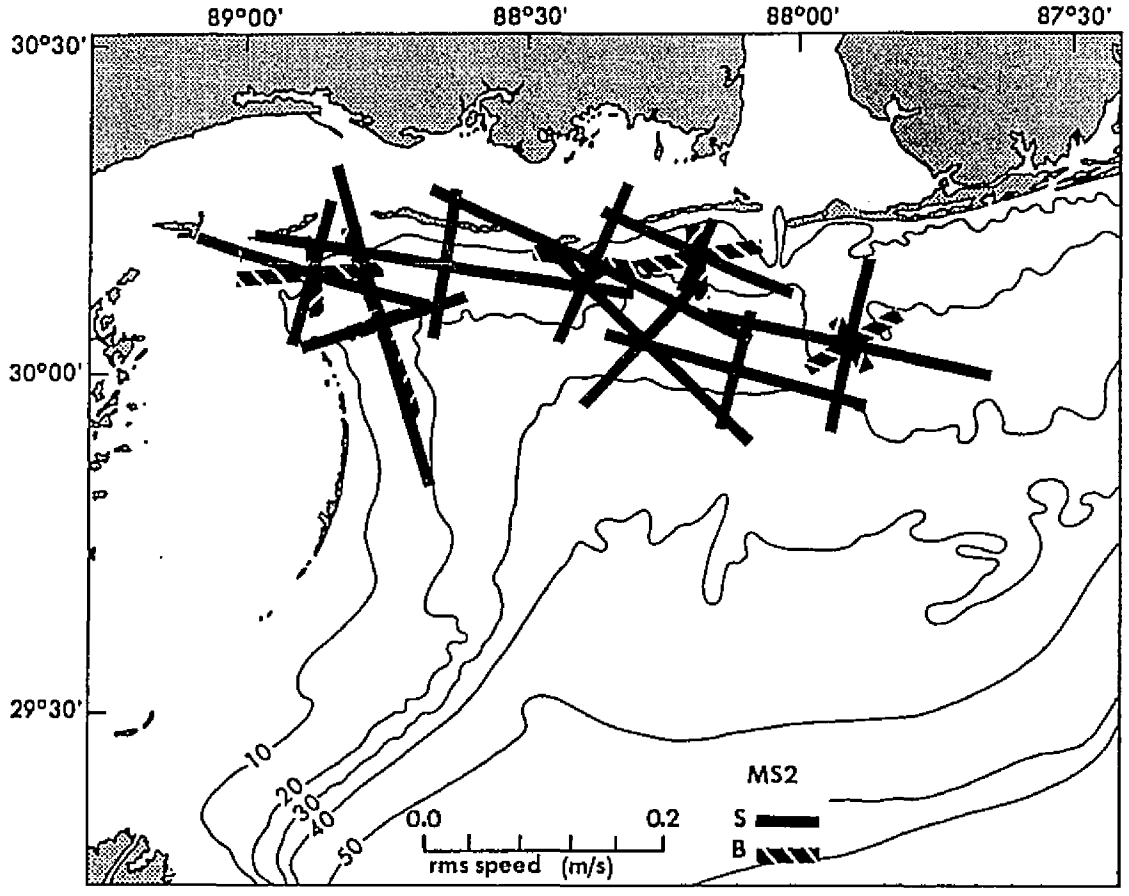

Figure 24. Current meter low passed principal axes for MS2. Length of axes are the rms values along the principal axes.

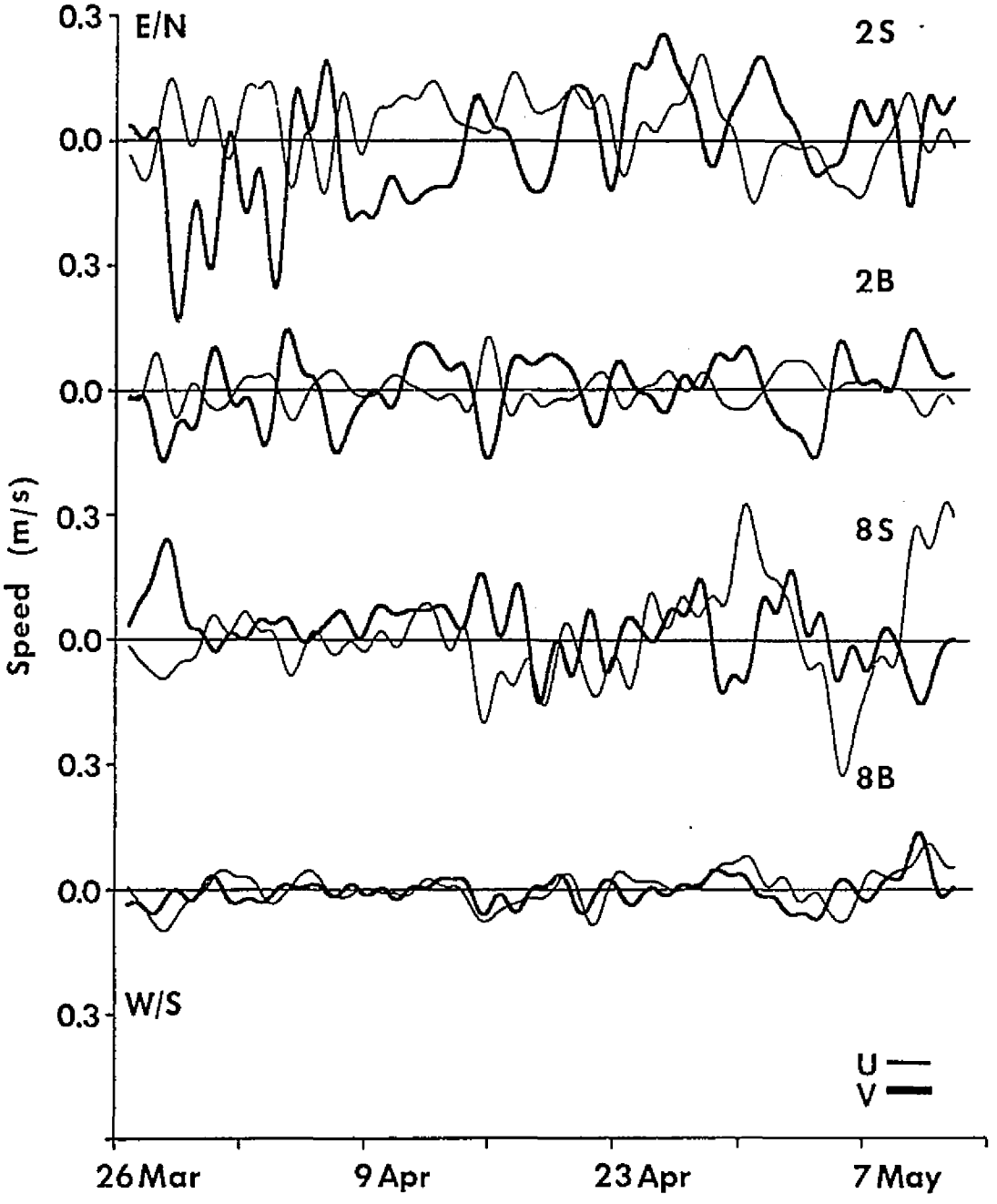

Figure 25. Current meter time series for MS2. Surface and bottom velocity components for CM2, surface and bottom velocity components for CM8. The velocity component, u, (light) is positive east; v, (dark) is positive north.

at CM5 and CM7 (not shown) are similar to those at CM8S, with small-amplitude current fluctuations over the first half and large variations over the latter half of the record. At CM3S, CM4 and CM6 (not shown) were energetic during the early part of the deployment. The currents at CM1S (not shown) attained speeds of 0.3 m/s and flowed almost exclusively to the east-southeast over the first half of the record. The inner shelf currents flow generally flowed counterclockwise over the first half of the deployment and clockwise during the latter half. Brief current reversals occurred throughout the deployment.

Winds were coherent over the entire shelf. Coastal winds at DI led the shelf break winds at BY by 9 hours. This lag is an average of the short, less than 3 hour, and the long, 24 hour, wind shift lags due to frontal passage across the shelf. Short lags occurred when polar air rapidly moved through the region behind cold fronts. Longer lags occurred when fronts stalled in the coastal region or when low pressure centers migrated across the area. At such times the wind field could be very different at the two wind sites. Wind direction at BY was rotated approximately 6-8^{o} clockwise of that at DI.

DI wind roses for the month of April were very similar to the April composite of Schroeder and Wiseman (1985). Tropical maritime air moved onshore as a result of the strengthening of the Bermuda high pressure system off the east coast of the U.S.. Prevailing winds were from the

southeast. Interruption of this wind field occurred when atmospheric low pressure systems or polar air outbreaks and associated cold fronts migrated across the continent. Post-frontal winds from the north or northwest were short lived, lasting only one to two days (Figure 26).

Water levels were very coherent during this deployment. Bottom pressure gauges recorded $\pm$0.08 m fluctuations while DIWL variations had a range of 0.42 m. Major fluctuations occurred in late March and early April during cold front passages. An early-May atmospheric low pressure system migrating from over the Mississippi Delta toward the northeast passed over the study area and caused the greatest water level fluctuations.

Complex Spectrum Analysis

Energy in the wind stress spectra from DISL is concentrated in two frequency bands (Figure 27): clockwise-rotating winds from 0.3 to 0.5 cpd and more variable motion below 0.22 cpd. The statistical reliability of spectrum estimates for frequencies less than 0.08 is poor because of the limited number of cycles contained within the total record. BY wind stress spectra very similar to DI spectra. Spectrum energy levels, though, are higher over the energetic frequency bands. Coherence between DI and BY wind stress (not shown) was very high, greater than 0.9, over frequencies from 0.07 to 0.3 cpd. The coherence of negative frequencies continued at high levels until 0.5 cpd, the

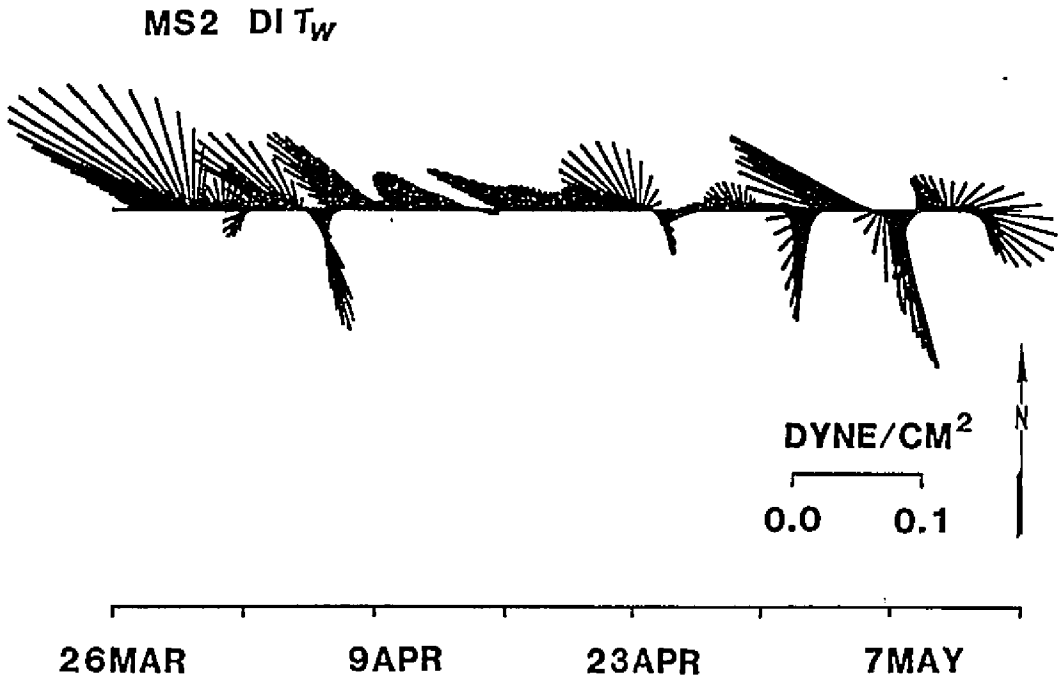

Figure 26. Stick plot of DI wind stress for MS2.

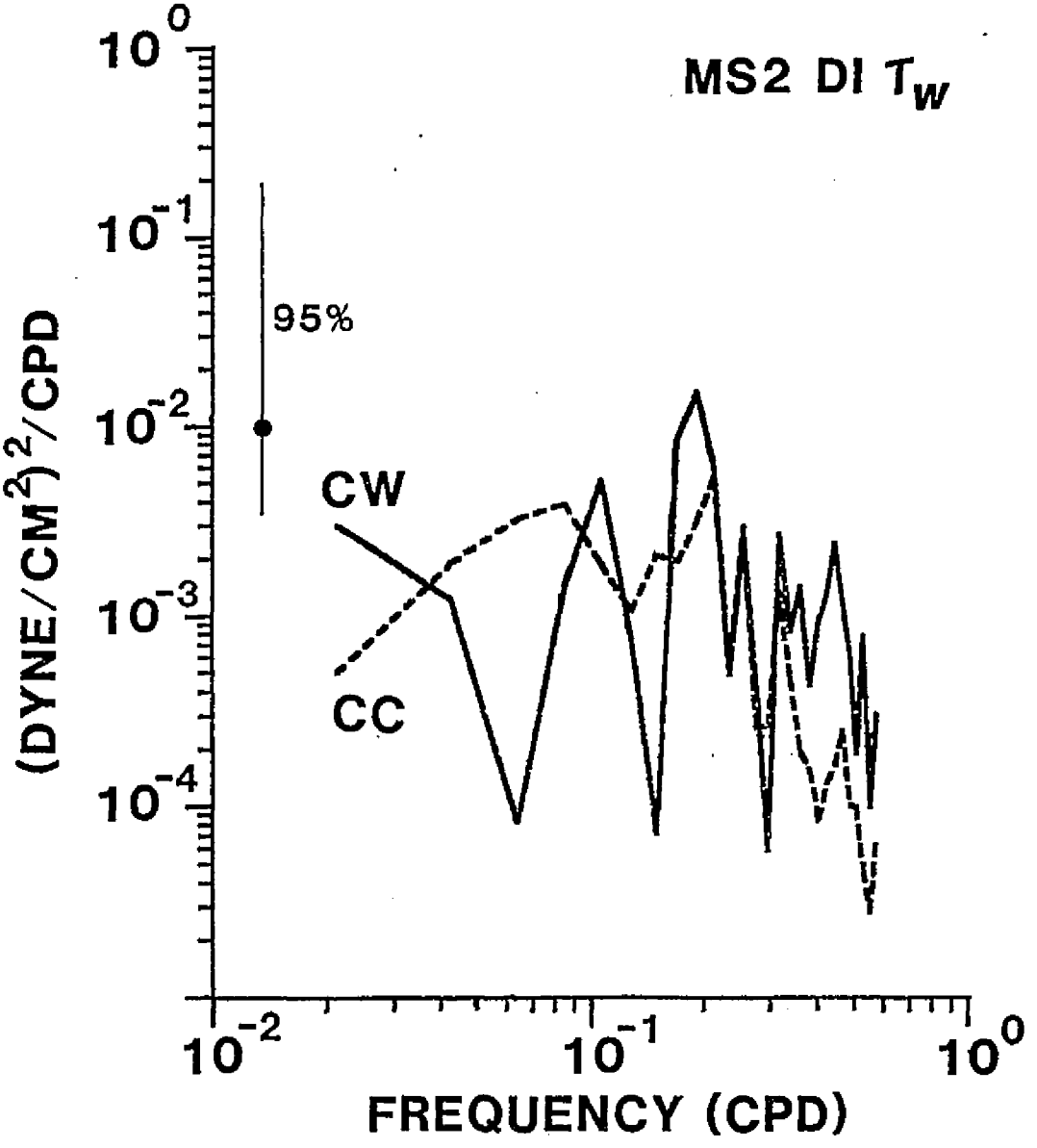

Figure 27. Complex wind stress spectra from DISL for MS2. Degrees of freedom are 4.

coherence of positive frequencies dropped to 0.75 at frequencies greater than 0.3 cpd. Phase was slightly positive over most frequencies less than 0.3 cpd, i.e. BY wind stress lagged DI wind stress by a small amount. This is consistent with the direction of cold front migration. Because the wind stress was coherent over the study region the DI wind stress was used in the subsequent cross-spectrum analyses.

The current spectra were generally bimodal (Figure 28). Energetic bands occurred near 0.4 cpd and below 0.1 cpd. The bottom currents were less energetic than the surface currents and primarily rotated clockwise. Coherence between the surface and bottom currents was moderate. Highest coherence was found near or below 0.1 cpd, e.g. Figure 29.

Coherence between currents and DI wind stress was generally erratic. At some moorings (CM1, CM4, CM7 and CM8), both surface and bottom currents were strongly coherent with the wind stress in a band near +0.1 cpd (Figure 30).

Complex EOF Analysis

The current field during MS2 can be described by three modes (Table 8) that are statistically different from random noise and account for only 66% of the total variance. Mode 1 dominated the field. Modes 2 and 3 occurred simultaneously much of the time. They were usually important when Mode 1 was rapidly changing magnitude or direction.

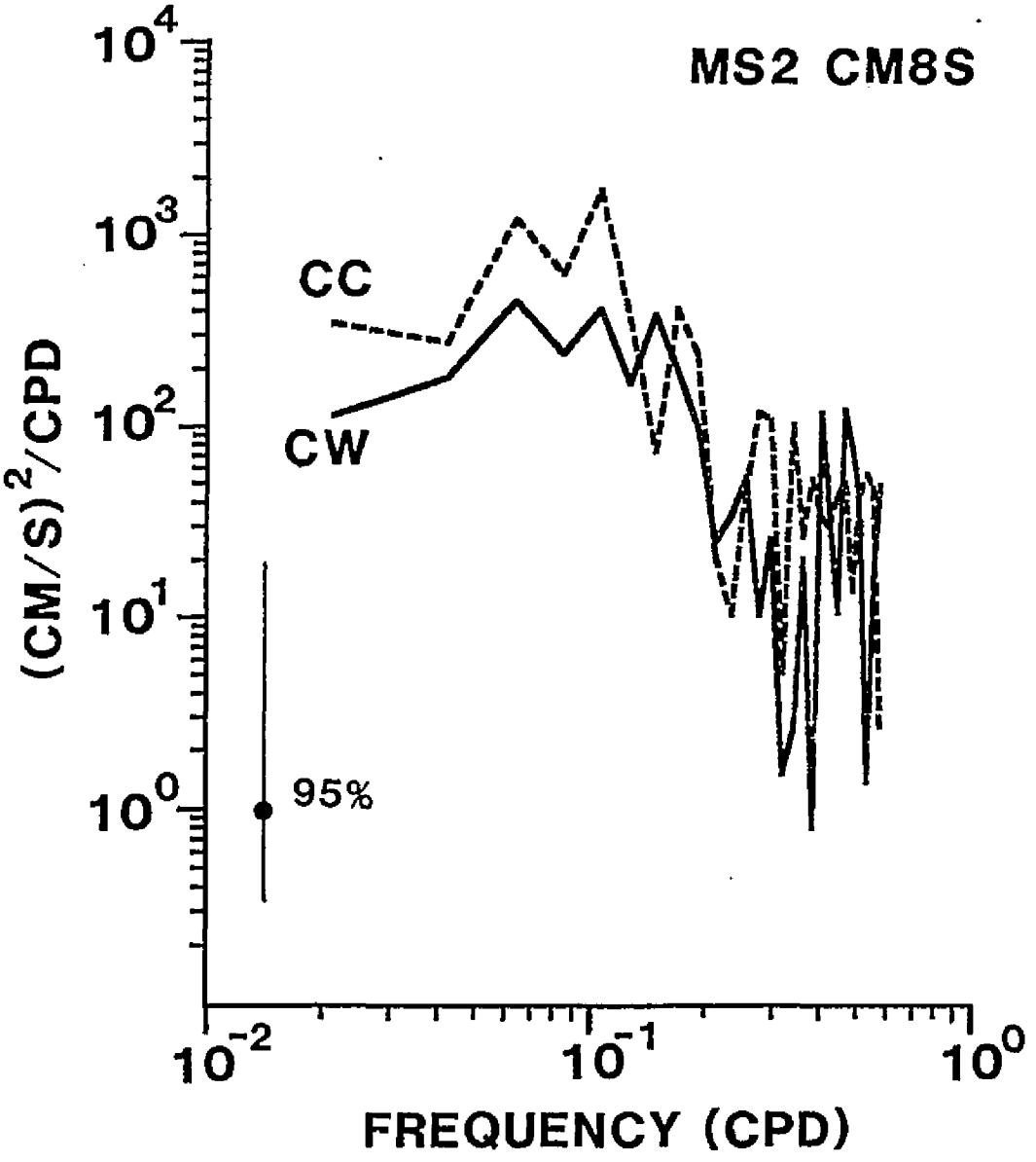

Figure 28. Complex current meter spectra from CM8S for MS2. Degrees of freedom are 4.

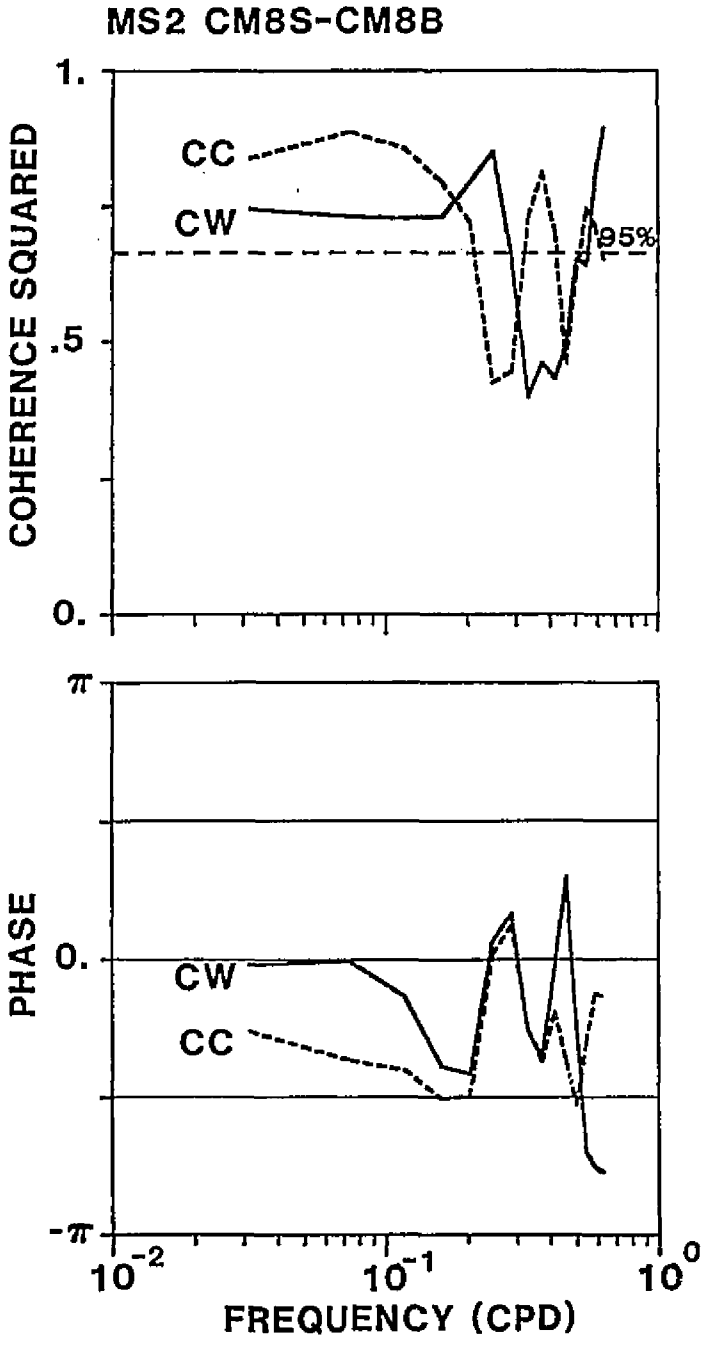

Figure 29. Complex coherence squared and phase between surface and bottom current meters at CM8 for MS2. Positive phase indicates bottom meter lags surface meter. Degrees of freedom are 8.

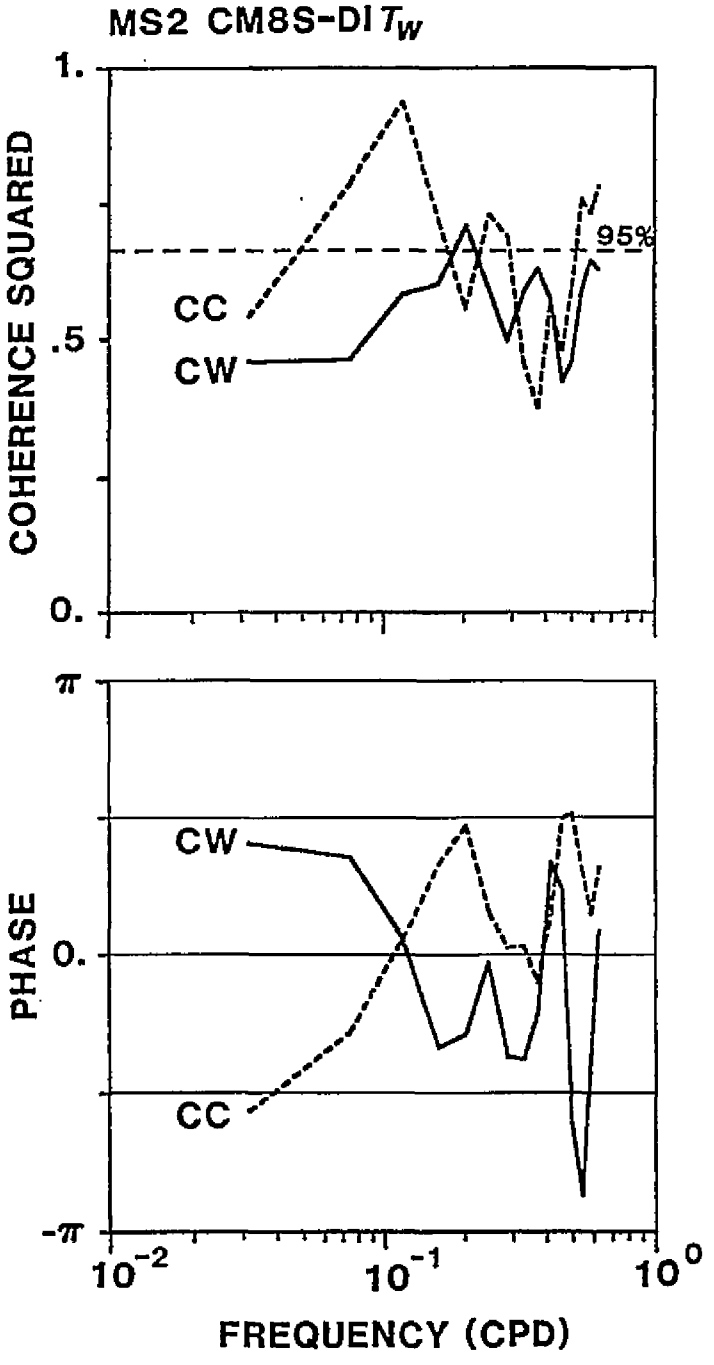

Figure 30. Complex coherence squared and phase between surface currents at CM8 and Dauphin Island wind stress for MS2. Positive phase indicates surface currents lag wind stress. Degrees of freedom are 8.

Table 8. Complex empirical orthogonal function statistics: percent total variance, $\%S_t$, 95% significance level, angle of preferred orientation, ψ, individual weights, β, phase angles, ϕ, and percent individual variance, $\%S_i$, for MS2. Inputs were current meters and DI wind stress.

	Mode 1			Mode 2			Mode 3		
$\%S_t$	38.28			16.97			11.09		
95% S.L.	12.76			11.64			10.89		
ψ^+	-36			-39			15		
Inputs	β	ϕ^+	$\%S_i$	β	ϕ^+	$\%S_i$	β	ϕ^+	$\%S_i$
CM1S	0.20	-36	20	0.19	-13	9	0.41	-118	26
CM1B	0.26	-15	36	0.18	92	8	0.35	-85	19
CM2S	0.22	-84	26	0.37	-69	35	0.33	-146	17
CM2B	0.27	-69	40	0.35	137	28	0.07	-111	1
CM3S	0.35	175	65	0.15	-106	6	0.08	62	1
CM4S	0.36	161	70	0.08	-40	1	0.07	-176	1
CM4B	0.23	-173	29	0.27	99	17	0.06	138	1
CM5S	0.24	149	31	0.30	-125	22	0.39	-120	23
CM6S	0.24	166	32	0.25	20	15	0.25	-179	9
CM6B	0.13	138	9	0.44	48	46	0.21	163	7
CM7S	0.29	160	45	0.22	-149	11	0.31	-67	15
CM8S	0.26	151	38	0.23	-94	12	0.39	-60	24
CM8B	0.31	-153	50	0.23	99	12	0.22	-52	7
$DI\underline{T}_w$	0.29	154	45	0.26	103	16	0.16	29	4

$^+$ Positive angles measured counterclockwise from positive x axis.

Mode 1 accounted for 33% of the total variance and had significant weights associated with most of the inputs. High individual weights were associated with the wind stress, CM2B, CM3S, CM4S, CM7S, and CM8, low weights with CM6B, and moderate weights with CM1, CM2S and CM4B. Surface and currents at offshore sites were most heavily weighted. This mode describes a barotropic response. The principal component variance ellipse for Mode 1 is highly elongated (Figure 31). As during MS1, the Mode 1 flow pattern describes clockwise or counterclockwise flow around the inner shelf (Figure 32). The magnitude of Mode 1 correlates well with times of northwestward wind stress. When the region is influenced by the Bermuda High, a counterclockwise flow occurs. The flow pattern reverses when the wind reverses. Currents at CM1 are counter to the flow along the Mississippi-Alabama barrier islands.

Mode 2 describes 17% of the total variance. Flow directions at surface and bottom meters, are often in opposite directions (Figure 32). This is consistent with baroclinic flows or strong shears required to maintain continuity. The principal component variance ellipse is much more circular than for Mode 1 (Figure 31). The magnitude of Mode 2 usually correlates with times of clockwise rotation of the wind stress, which occurs a short time before and after cold front passage. Prefrontal winds are associated with currents flowing counterclockwise. Mode 2 currents begin to reverse direction, as winds shift after frontal

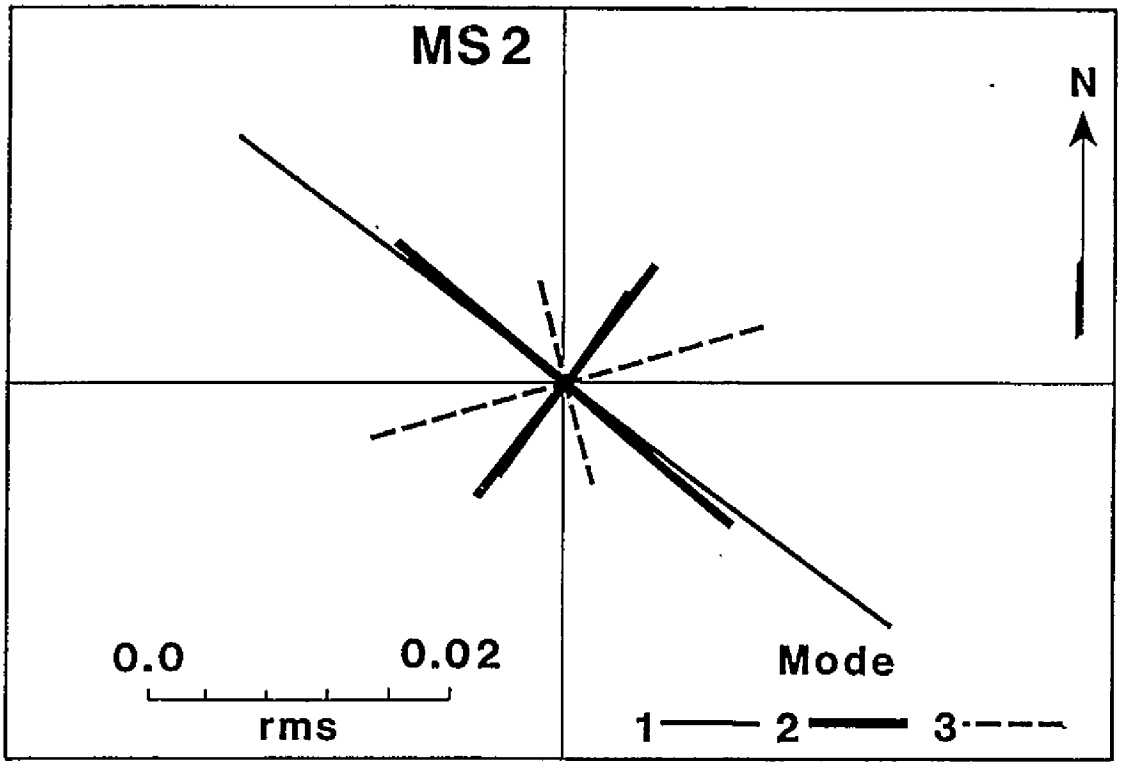

Figure 31. Rms values of principal component coefficients for Modes 1,2 and 3, for MS2.

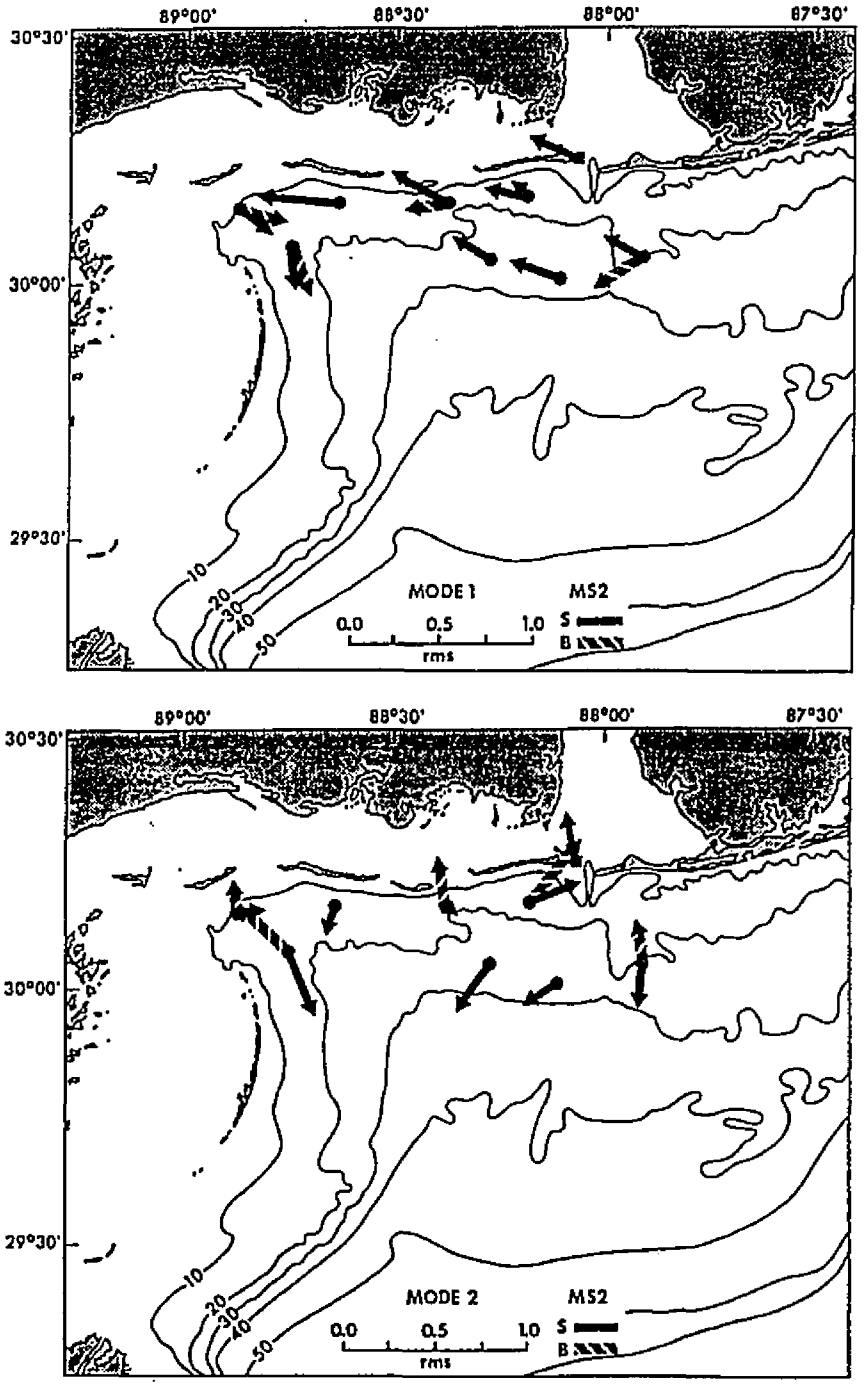

Figure 32. Complex EOF principal component eigenvectors rotated to a preferred orientation for Mode 1 (upper), Mode 2 (lower) and Mode 3 (next page), for MS2.

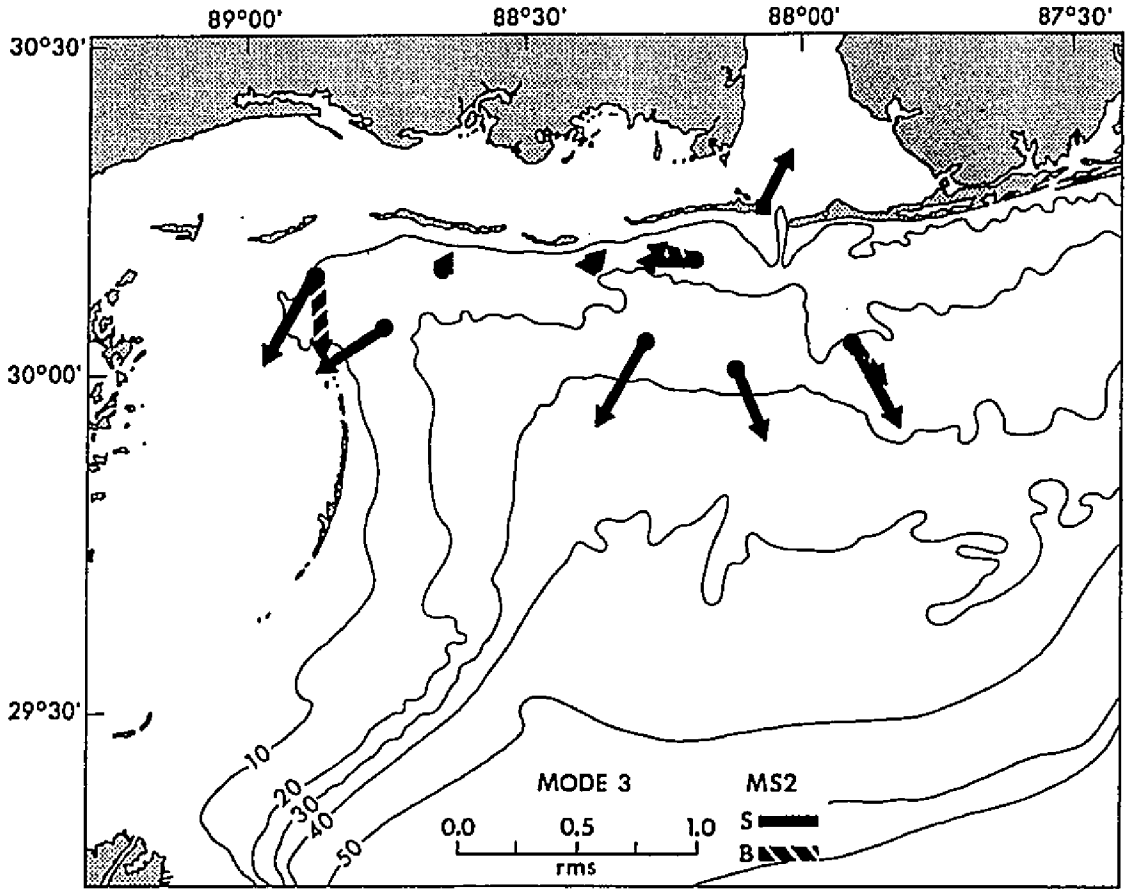

Figure 32. Continued.

passage. Post-front winds are usually to the south. The winds rotate clockwise to north-westward again as fronts move away and their influence diminishes. This post front wind rotation initiates a reversal of the clockwise flowing currents.

Mode 3 describes 11% of the total variance. It is just significantly different from noise at the 95% level (Table 8). This pattern is consistent with barotropic flow, but does not appear to be driven by the wind stress (Figure 32).

Mode 1 describes the primary flow pattern. Modes 2 and 3 occur during brief transitions when Mode 1 changes direction.

Inner Shelf Momentum Balance

The momentum balance was estimated only at CM8 because of insufficient bottom current data elsewhere. The estimated balance is ageostrophic (Figure 33). A large residual term was estimated for both the alongshelf and across-shelf equations. The coriolis terms and the across-shelf pressure term are the dominant ones determined directly from the data (Table 9). Other terms were important during brief events. Better data are clearly needed in order to resolve the dynamics of this region.

Discussion

An onshore statistically-significant mean flow, of 0.02 to 0.04 m/s, was present at the offshore surface meters

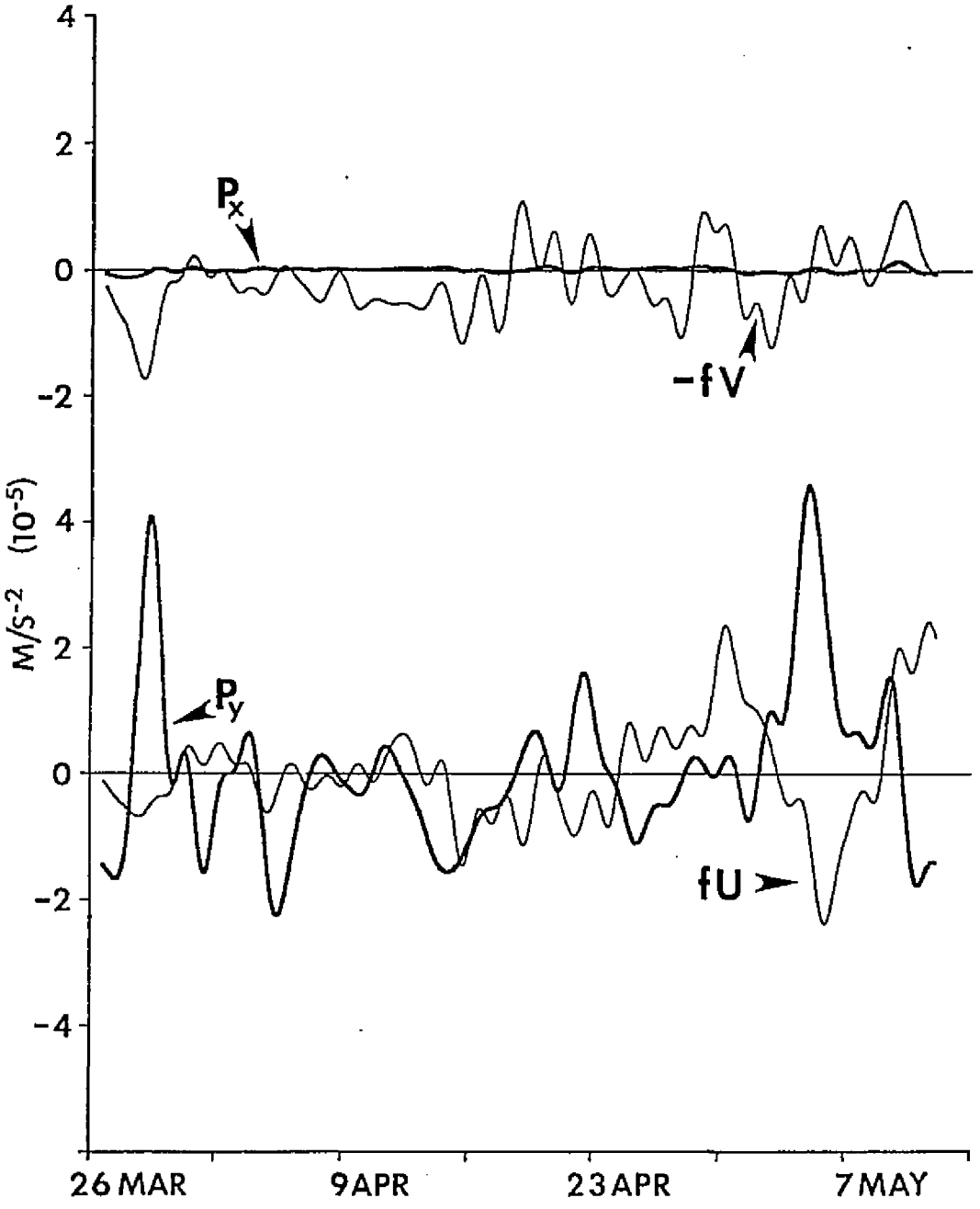

Figure 33. Alongshelf (upper) and cross-shelf (lower) momentum equation terms for CM8 from MS2.

Table 9. Rms values of momentum balance terms, in both alongshelf and cross-shelf directions, for CM8 of MS2. Units are m/s^2 ($x10^{-7}$).

	Alongshelf						
	$\frac{\partial U}{\partial t}$	$U\frac{\partial U}{\partial x}$	$V\frac{\partial U}{\partial y}$	fV	$g\frac{\partial \eta}{\partial x}$	$\frac{\tau_{sx}}{\rho H}$	$\frac{\tau_{bx}}{\rho H}$
CM8	14.30	5.92	3.58	54.16	4.04	17.54	4.36

	Across-shelf						
	$\frac{\partial V}{\partial t}$	$U\frac{\partial V}{\partial x}$	$V\frac{\partial V}{\partial y}$	fU	$g\frac{\partial \eta}{\partial y}$	$\frac{\tau_{sy}}{\rho H}$	$\frac{\tau_{by}}{\rho H}$
CM8	13.69	6.20	3.08	87.70	126.63	19.24	3.92

from 26 March to 12 May. Inshore, shallower currents had statistically-significant eastward mean flow of 0.03 to 0.08 m/s. Winds were predominantly from the southeast, cold fronts were associated with major interruptions of this wind field. Wind variance was largest at frequencies less than 0.2 cpd. Current fluctuations were coherent with the winds at frequencies less than 0.2 cpd. Currents were spatially coherent at these same time scales. These current fluctuations reached speeds of $\pm$0.1 m/s and flowed roughly parallel the isobaths. Winds from the southeast did produce a counterclockwise flow around the corner of the inner shelf. The eastward mean flows are the result of the highly non-stationary nature of the system and the short record length.

MS3 DEPLOYMENT

General Data Description

Less current meter data was available from the third deployment, MS3, than from the previous two. This was due to fewer moorings being deployed and to low quality of the returned data records. A 40.375-day synoptic data set was sampled by seven current meters. Current meter data, from 1500 CST 18 July to 0000 CST 28 August 1981, were analyzed with concurrent DI wind stress, DIWL and water pressures from P2 and P3. A salinity- and temperature- stratified water column existed at the beginning of MS3 (Kjerfve and Sneed, 1984). Surface and bottom values of salinity and

temperature were approximately 30 and 35 ppt and 30° and 24° C, respectively. Surface values remained fairly constant throughout the record, but bottom temperatures increased to over 29° C over the first half of the record, before stabilizing. Bottom salinities decreased gradually over the entire record to near 31 ppt in late August. Surface to bottom density differences decreased from about 7 to 1 kg/m^3 over the record length.

Flow statistics (Table 10, Figure 34) were estimated for the MS3 deployment. The mean currents from deeper water (CM5, CM7 and CM8) are generally to the west and statistically-significant. The bottom currents had an offshore component and surface meters had an onshore component. The bottom current at CM2 was south-southwestward. Strong vertical shear was present at sites with both surface and bottom meters. This was probably due to a baroclinic flow component favored by the stratification.

The principal axes of the surface and bottom currents were generally aligned west-southwest east-northeast (Figure 35). Minor axes were much smaller than the major axes. This was probably because of steering. Alongshelf surface rms velocities were much larger than bottom values. This vertical shear could be the result of the stratification observed during most of the deployment.

A coherent clockwise or counterclockwise flow was usually present over the entire inner shelf. Currents were not very

Table 10. Flow statistics for MS3 current meter component means, $\underline{u}$, $\underline{v}$ ($\times 10^{-2}$ m/s), low passed variances S^2_u and S^2_v ($\times 10^{-4}$ m^2/s^2), correlation time scales, t_{ou}, t_{ov} (d), standard errors, SE_u, SE_v ($\times 10^{-2}$ m/s), and rotation angle of principal axes, θ (deg).

CM	$\underline{u}$	$\underline{v}$	S^2_u	S^2_v	t_{ou}	t_{ov}	SE_u	SE_v	θ^+
2B	0.28	-1.37	2.01	25.84	1.18	1.36	0.47	0.82	29.27
4S	0.85	0.25	155.43	6.43	1.67	1.79	2.47	0.80	-13.26
5S	-5.73*	0.27	117.66	14.23	2.03	0.98	2.41	0.63	-8.67
7S	-6.94*	0.89*	124.91	10.26	2.14	0.65	2.57	0.42	-4.40
7B	-4.30*	-1.49*	27.16	5.34	1.12	1.16	0.85	0.43	11.83
8S	-5.69	3.11*	309.41	23.80	2.45	1.48	4.15	1.35	-17.56
8B	-7.00*	-2.41*	39.60	11.59	1.58	1.13	1.22	0.61	14.39

+ Positive angle measured counterclockwise.

* Statistically significant at the 95% level, i.e. larger than 2 SE.

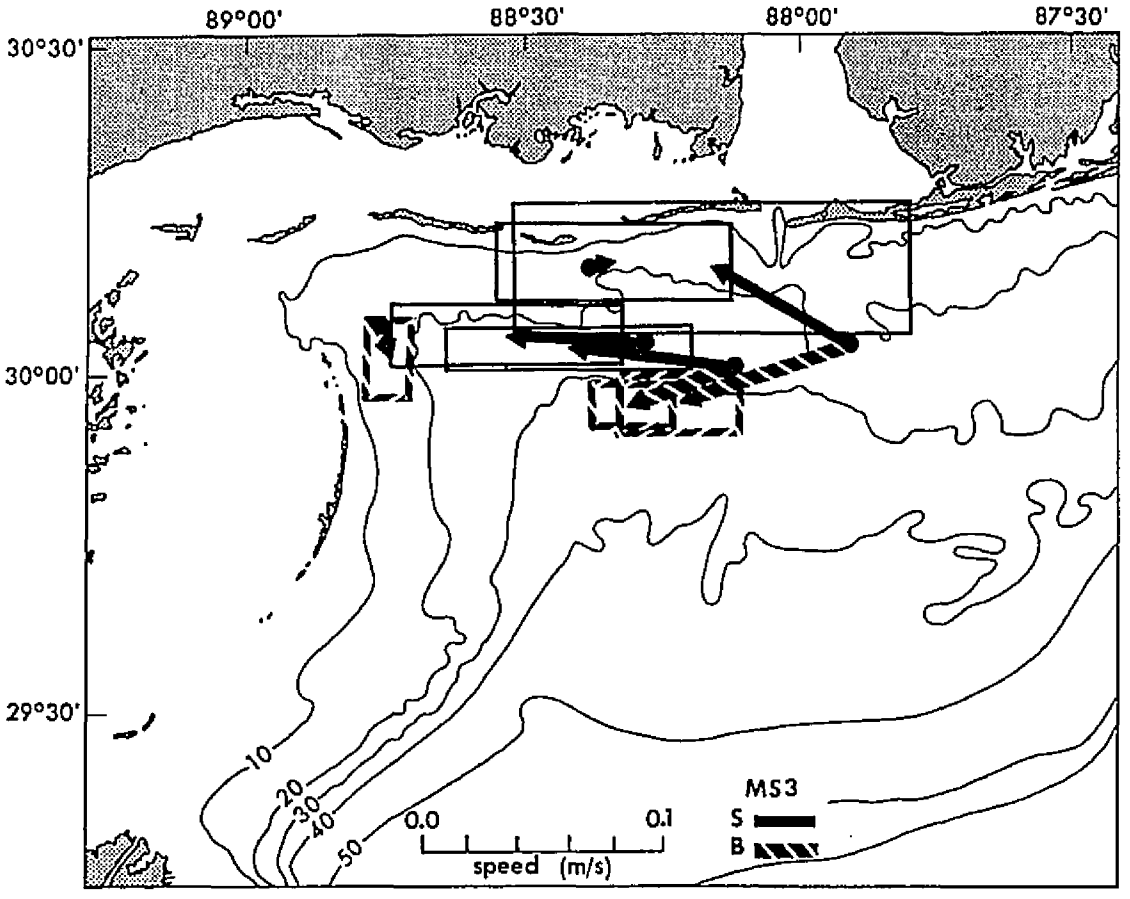

Figure 34. Current meter components mean speeds and standard errors for MS3. Boxes are ± 2 standard errors about the means.

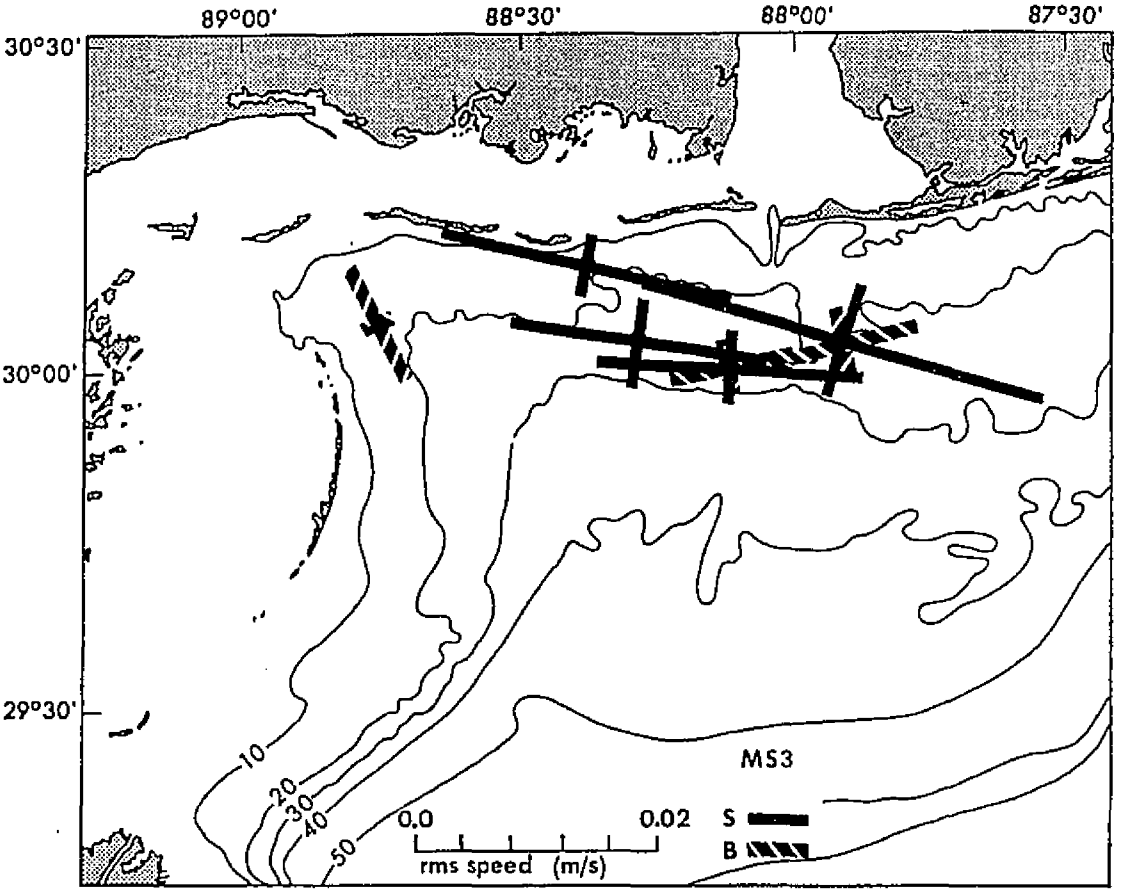

Figure 35. Current meter low passed principal axes for MS3. Length of axes are the rms values along the principal axes.

energetic except at the beginning and at the end of the deployment (Figure 36). A strong clockwise flow occurred from the onset of the deployment until 20 July. Eastward currents at CM8S and CM4S were greater than 0.4 m/s. Simultaneously, northward currents were present at CM2B, but at much reduced speeds. Bottom currents at the other moorings were weak and counter to the surface currents. Surface currents reversed direction around July 23rd and flowed in a modulated, generally counterclockwise pattern through August. For short periods, flow at CM2B and CM4S was northward or eastward, respectively. Alongshelf flow at the offshore moorings weakened, occasionally to near stagnant conditions, but never reversed.

DI winds for July and August were similar but weaker than the monthly composites of Schroeder and Wiseman (1985). The winds were weak and a function of the atmospheric high pressure system over the Gulf of Mexico except for a relatively strong event at the end of the record (figure 37). This high would stall cold fronts, or occlude fronts parallel to the Mississippi-Alabama coastline but north of the Gulf. The fronts then dissipated or moved eastward. An occluded front in late August finally pushed over the shelf after remaining near the coast for three days. Strong southwesterly winds on the 19th, followed by primarily westerly winds until the 26th, forced the observed counterclockwise current pattern.

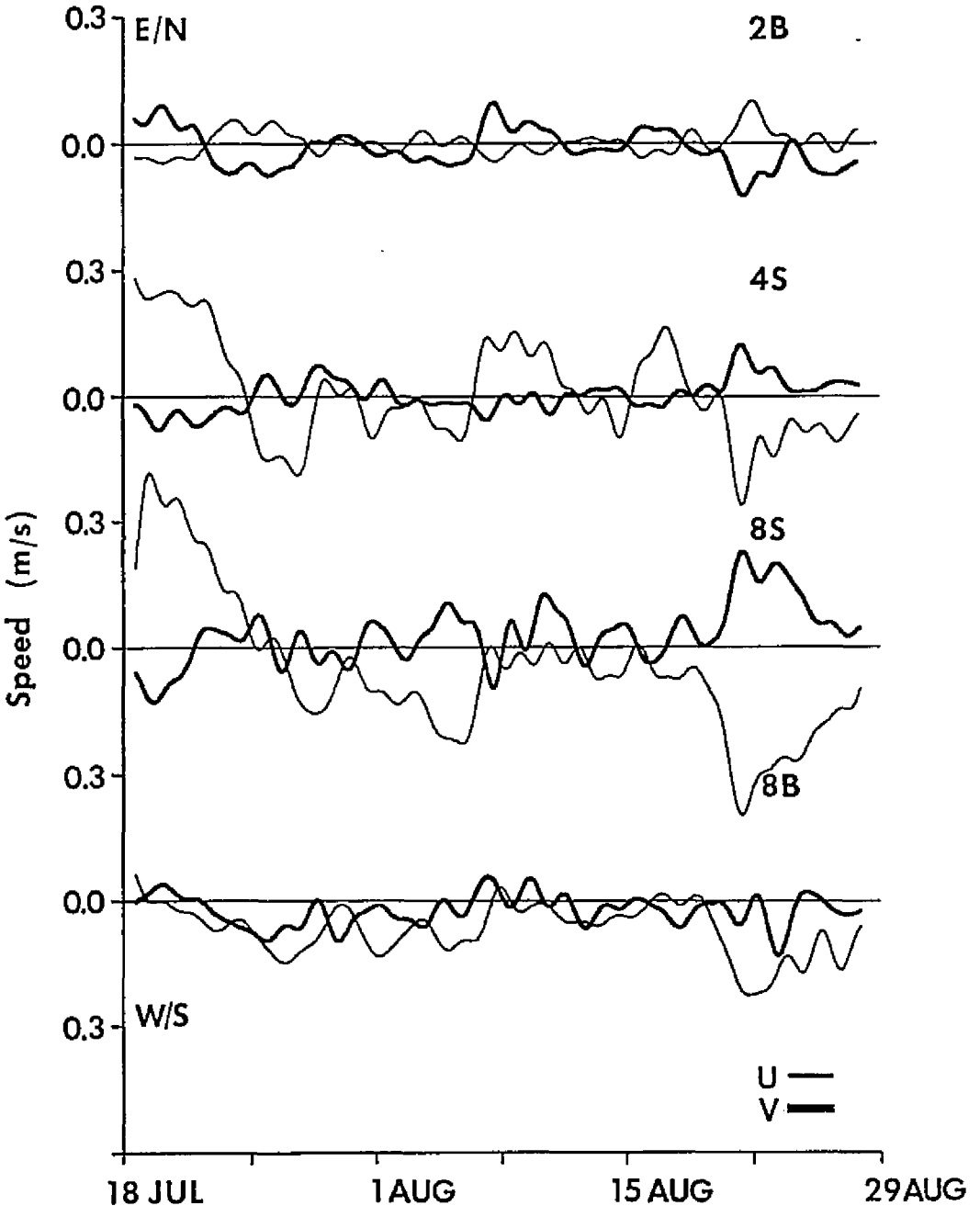

Figure 36. Current meter time series for MS3. Bottom velocity components for CM2, surface velocity components for CM4, surface and bottom velocity components for CM8. The velocity component, u, (light) is positive east; v, (dark) is positive north.

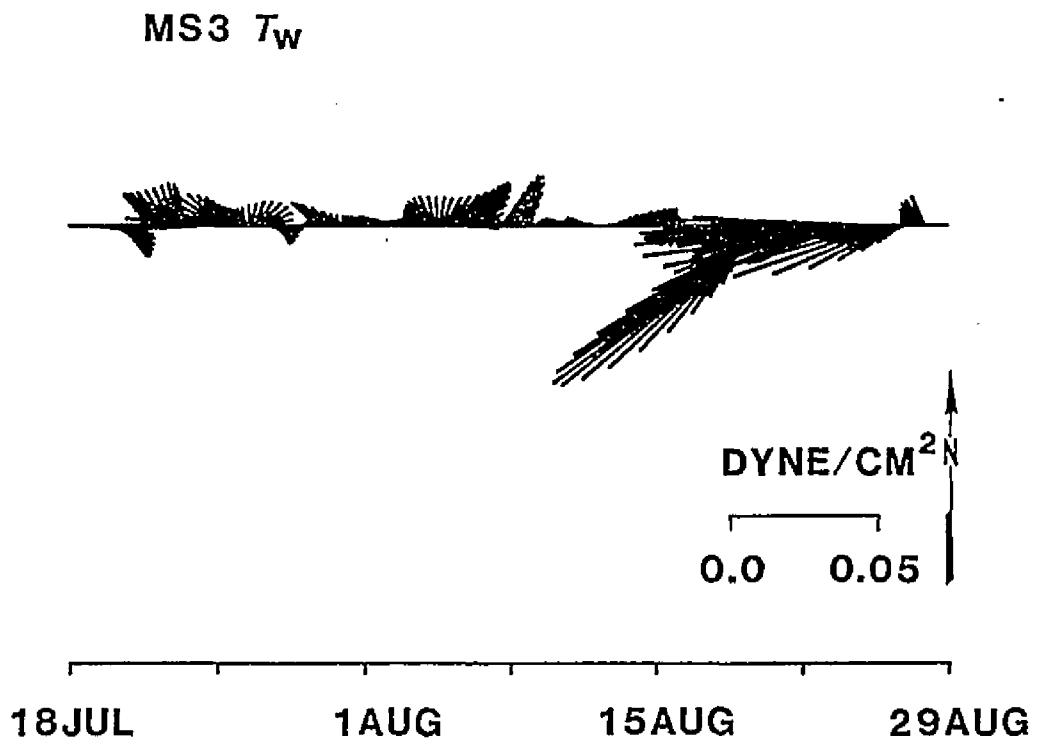

Figure 37. Stick plot of DI wind stress for MS3.

Water level variations of $\pm$0.1 meters were usually coherent over the inner shelf.

Complex Spectrum Analysis

The DI wind stress is energetic in two frequency bands with clockwise rotation (near 0.2 and below 0.1 cpd) (Figure 38).

Subtidal current velocities vary in a nearly rectilinear manner. Surface currents are more energetic than bottom currents. The spectra are often dominated by low frequency energy (Figure 39).

Surface and bottom currents at CM8 are highly coherent in the frequency band +0.06 to +0.02 (Figure 40).
The currents at CM8S and DI wind stress coherent in bands near $\pm$0.3 cpd (Figure 41).

Complex EOF Analysis

The first two EOF modes during MS3 account for 77% of the total variance, although only the first mode is statistically different from random noise. Mode 2 was generally important when Mode 1 was changing magnitude rapidly.

Mode 1 described over 64% of the total variance in the data. This mode was important at all the current meter sites but described only a small portion of the wind stress variance (Table 11). Surface currents were slightly more important than bottom currents in this mode. Mode 1, as in

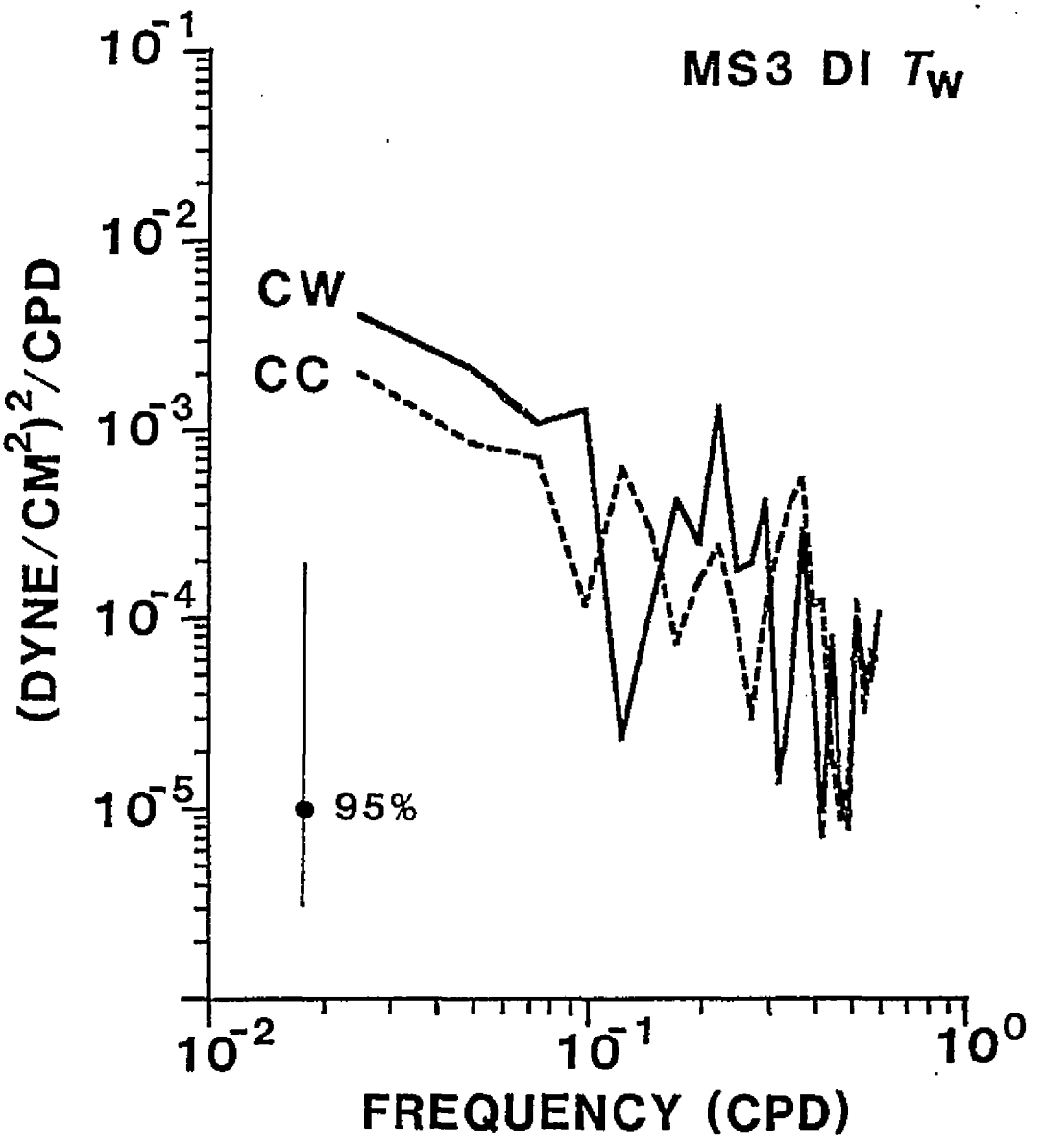

Figure 38. Complex wind stress spectra from DISL for MS3. Degrees of freedom are 4.

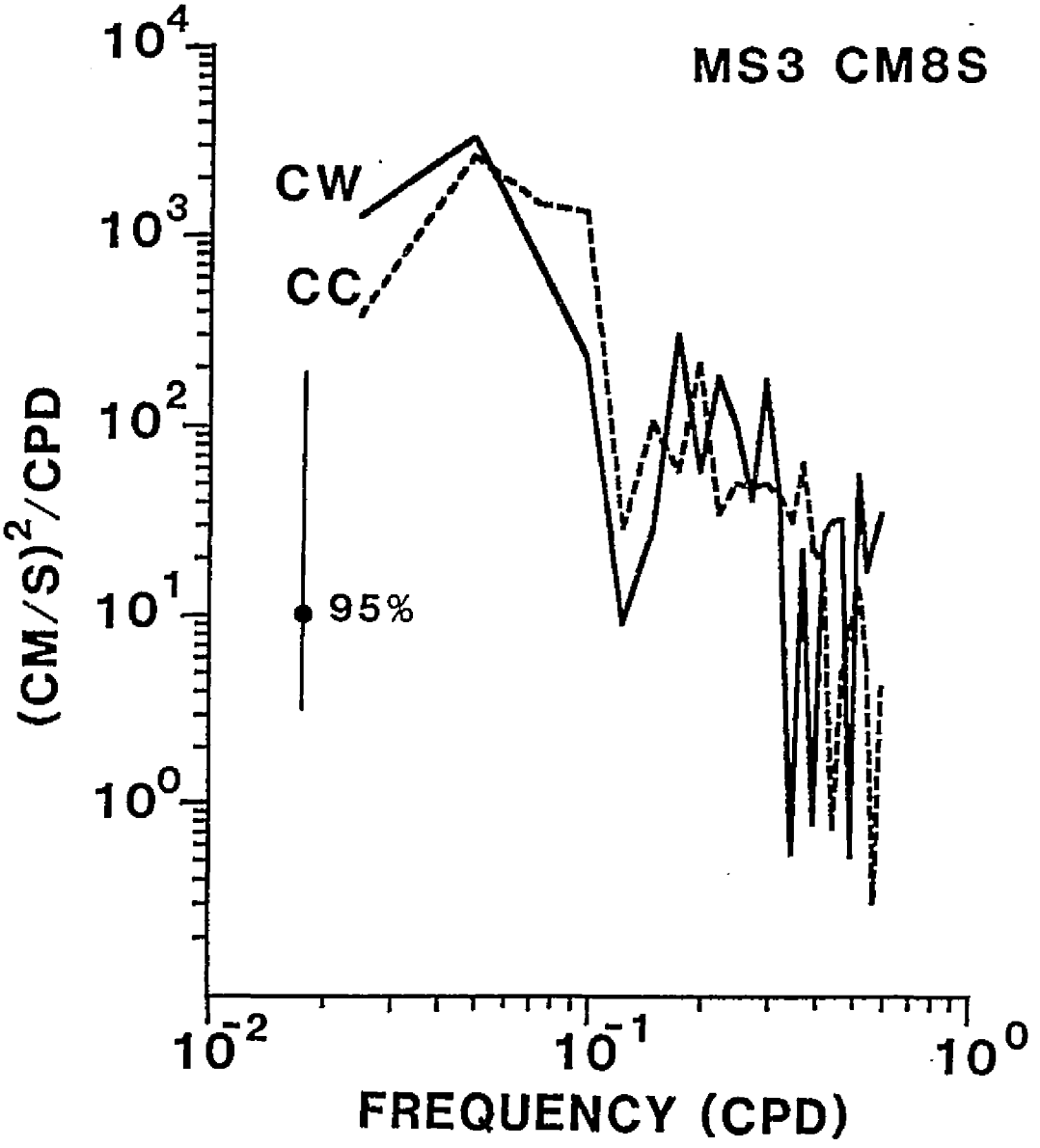

Figure 39. Complex current meter spectra from CM8S for MS3. Degrees of freedom are 4.

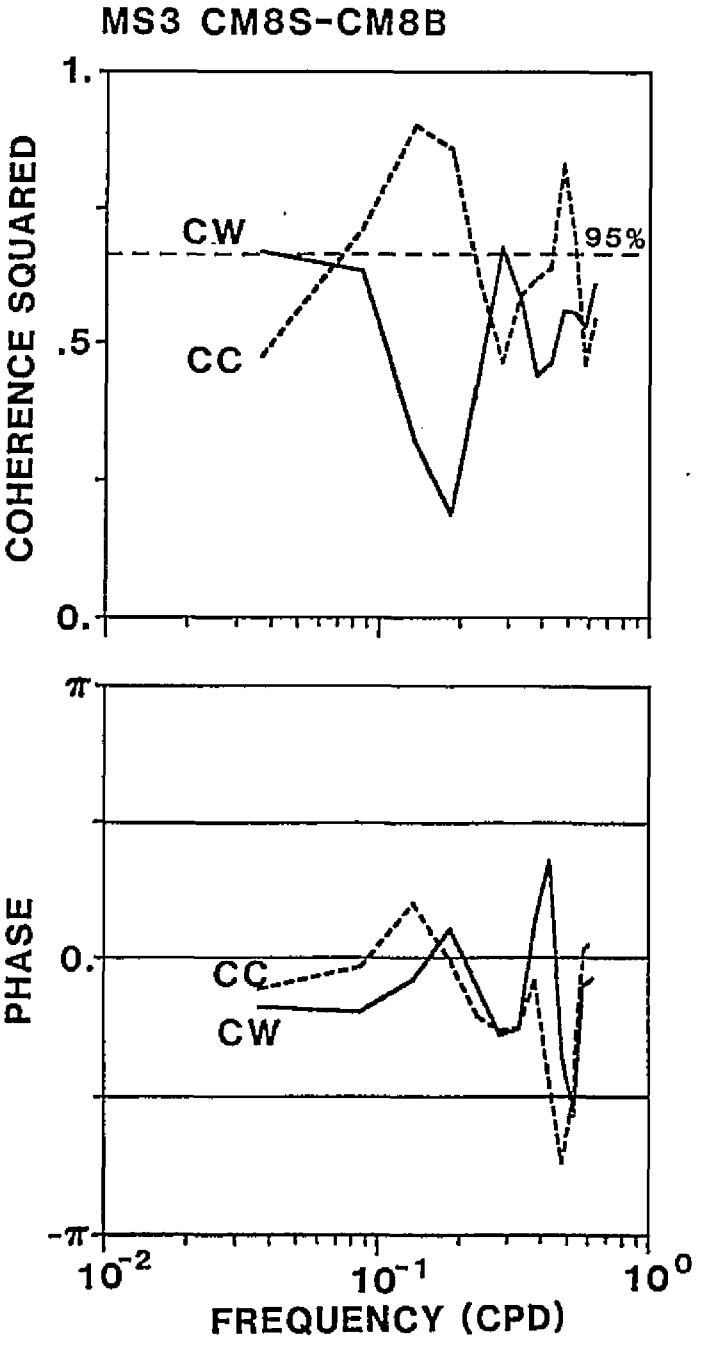

Figure 40. Complex coherence squared and phase between surface and bottom current meters at CM8 for MS3. Positive phase indicates bottom meter lags surface meter. Degrees of freedom are 8.

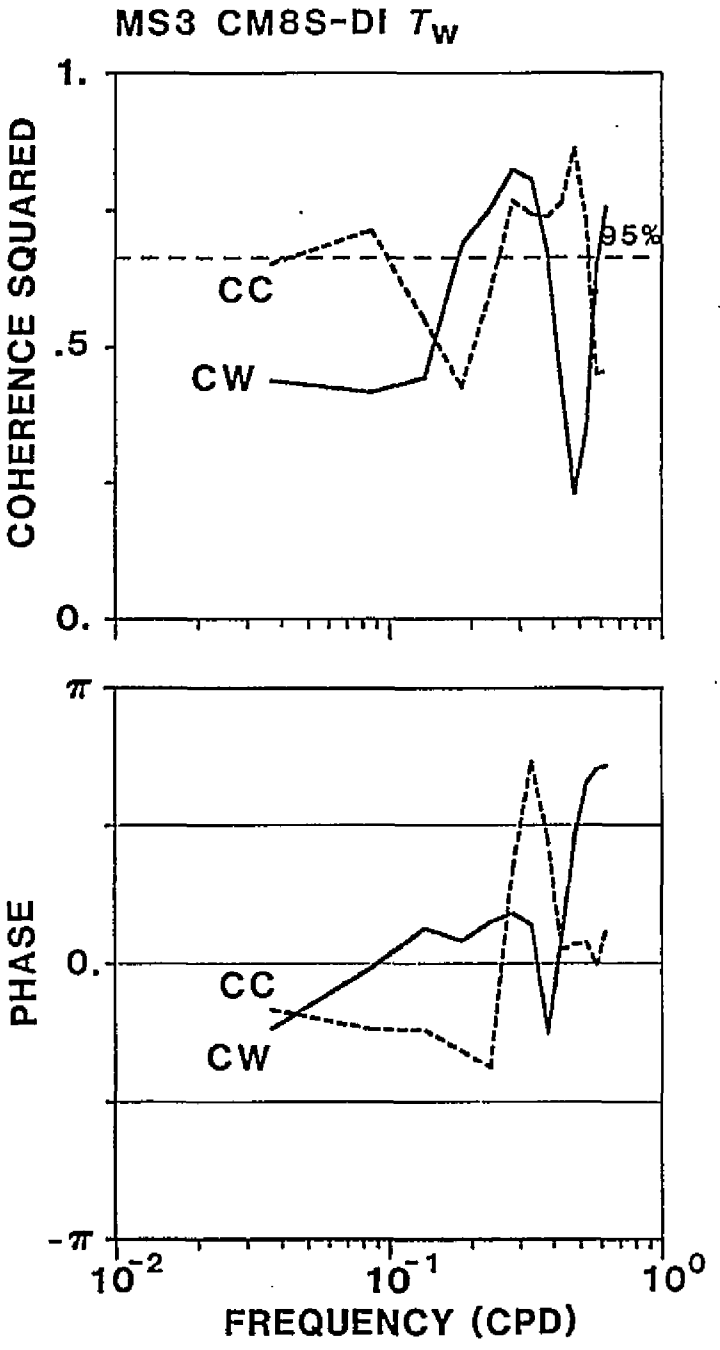

Figure 41. Complex coherence squared and phase between surface currents at CM8 and Dauphin Island wind stress for MS3. Positive phase indicates surface currents lag wind stress. Degrees of freedom are 8.

Table 11. Complex empirical orthogonal function statistics: percent total variance, $\%S_t$, 95% significance level, angle of preferred orientation, ψ, individual weights, β, phase angles, ϕ, and percent individual variance, $\%S_i$, for MS3. Inputs were current meters and DI wind stress.

	Mode 1	Mode 2
$\%S_t$	63.86	13.44*
95% S.L.	16.08	14.59
ψ^+	-11	-76

Inputs	β	ϕ^+	$\%S_i$	β	ϕ^+	$\%S_i$
CM2B	0.36	122	66	0.28	-172	9
CM4S	0.40	-11	80	0.18	161	4
CM5S	0.36	-7	67	0.24	-114	6
CM7S	0.38	-3	75	0.21	-109	5
CM7B	0.36	16	68	0.38	110	16
CM8S	0.39	-15	77	0.26	-119	7
CM8B	0.35	24	62	0.15	128	2
DIT_w	0.18	13	16	0.75	-4	60

+ Positive angles measured counterclockwise from positive x axis.

* Not significantly different from noise at the 95% level.

the previous analyses, described a clockwise flow around the inner shelf or the reverse pattern (Figure 42). The wind stress contribution to this pattern was consistent with Ekman drift. The principal component variance ellipse was highly-extended alongshore because of the rectilinear nature of the current fluctuations.

Mode 2 described 13% of the total variance. Although this this is less than the 95% significance level, this mode describes much of the wind stress variance. The Mode 2 principal component variance ellipse is almost isotropic. The wind stress variation had no dominant orientation (Figure 43). The current weights in this mode are small, but the pattern is consistent with wind-driven upwelling.

Momentum Balance Analysis

The most important contributions to the summer momentum balance are from the coriolis and the barotropic pressure gradient terms (Table 12). The rms values of the other terms are within an order of magnitude of the larger two terms. Alongshore pressure gradient and coriolis forces were small during most of the record (Figure 44). Near the end of the deployment, when a slow front moved through the region and both the coriolis force and pressure gradient force increased.

The across shelf pressure gradient and the coriolis forces were very important in the across-shelf momentum balance (Table 12). None of the other terms had rms values

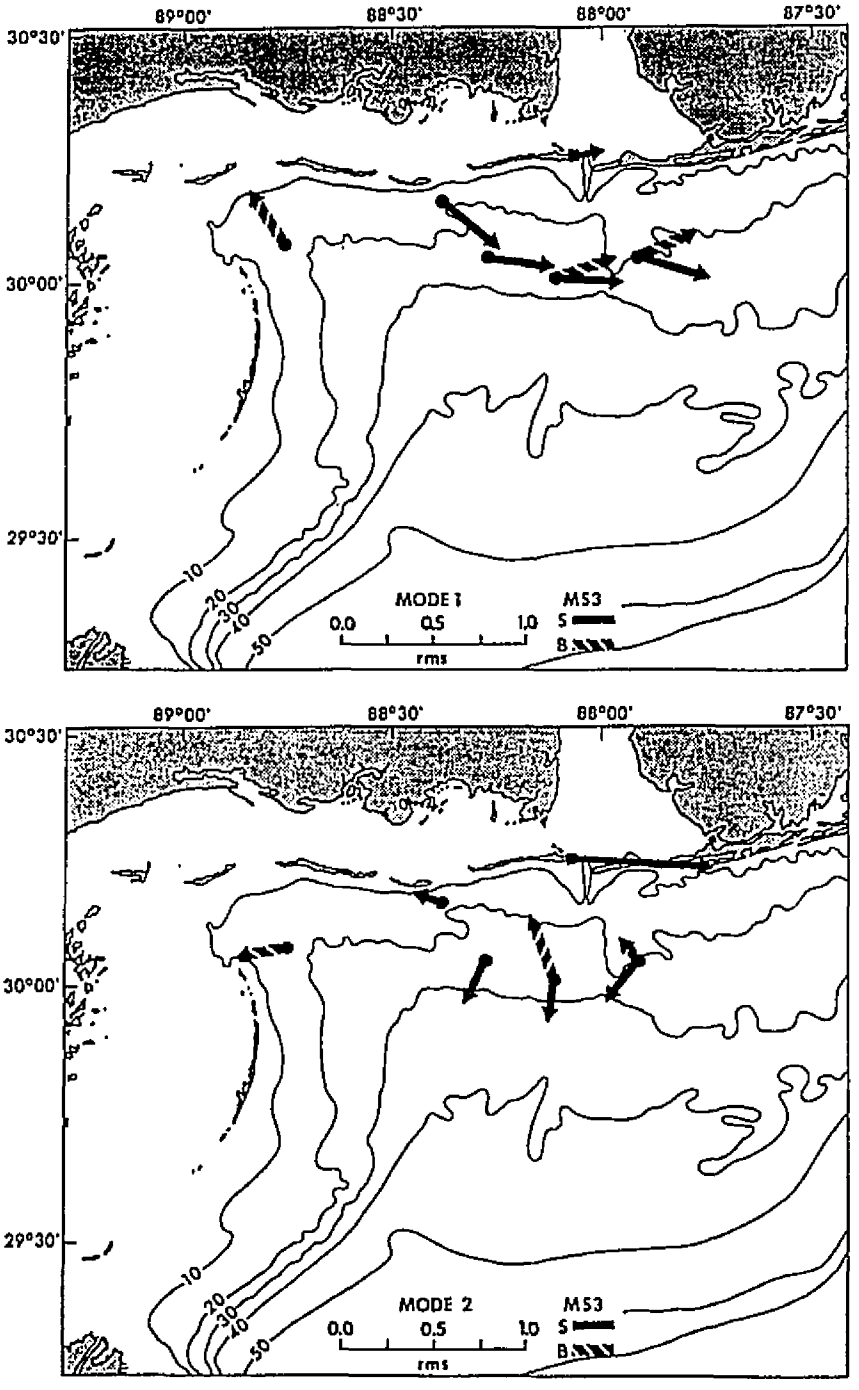

Figure 42. Complex EOF principal component eigenvectors rotated to a preferred orientation for Mode 1 (upper) and Mode 2 (lower), for MS3.

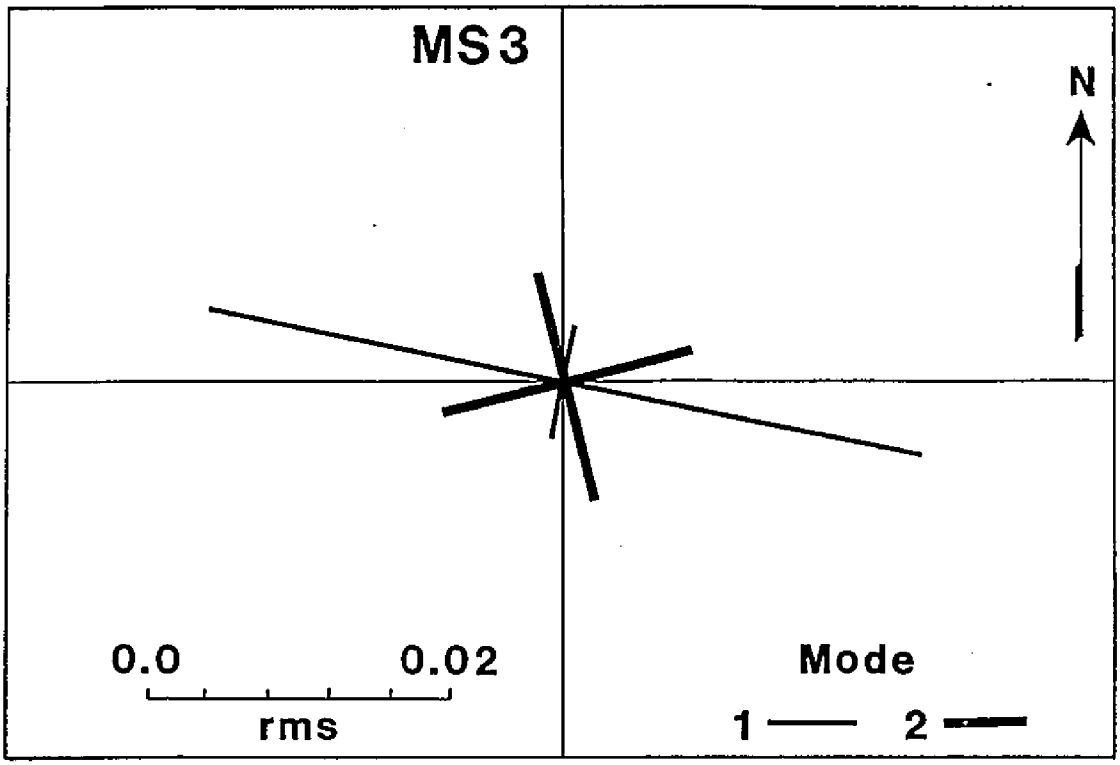

Figure 43. Rms values of principal component coefficients for Modes 1 and 2, for MS3.

Table 12. Rms values of momentum balance terms, in both alongshelf and cross-shelf directions, for CM7 and CM8 of MS3. Units are m/s^2 ($x10^{-7}$).

	Alongshelf						
	$\frac{\partial U}{\partial t}$	$U\frac{\partial U}{\partial x}$	$V\frac{\partial U}{\partial y}$	fV	$g\frac{\partial \eta}{\partial x}$	$\frac{\tau_{sx}}{\rho H}$	$\frac{\tau_{bx}}{\rho H}$
CM7	7.20	11.99	7.18	24.11	47.84	8.63	5.33
CM8	11.48	5.67	11.58	51.44	47.84	11.25	14.60

	Across-shelf						
	$\frac{\partial V}{\partial t}$	$U\frac{\partial V}{\partial x}$	$V\frac{\partial V}{\partial y}$	fU	$g\frac{\partial \eta}{\partial y}$	$\frac{\tau_{sy}}{\rho H}$	$\frac{\tau_{by}}{\rho H}$
CM7	6.97	3.46	4.77	81.25	51.59	4.81	2.06
CM8	9.65	3.63	10.03	122.73	51.59	6.24	5.98

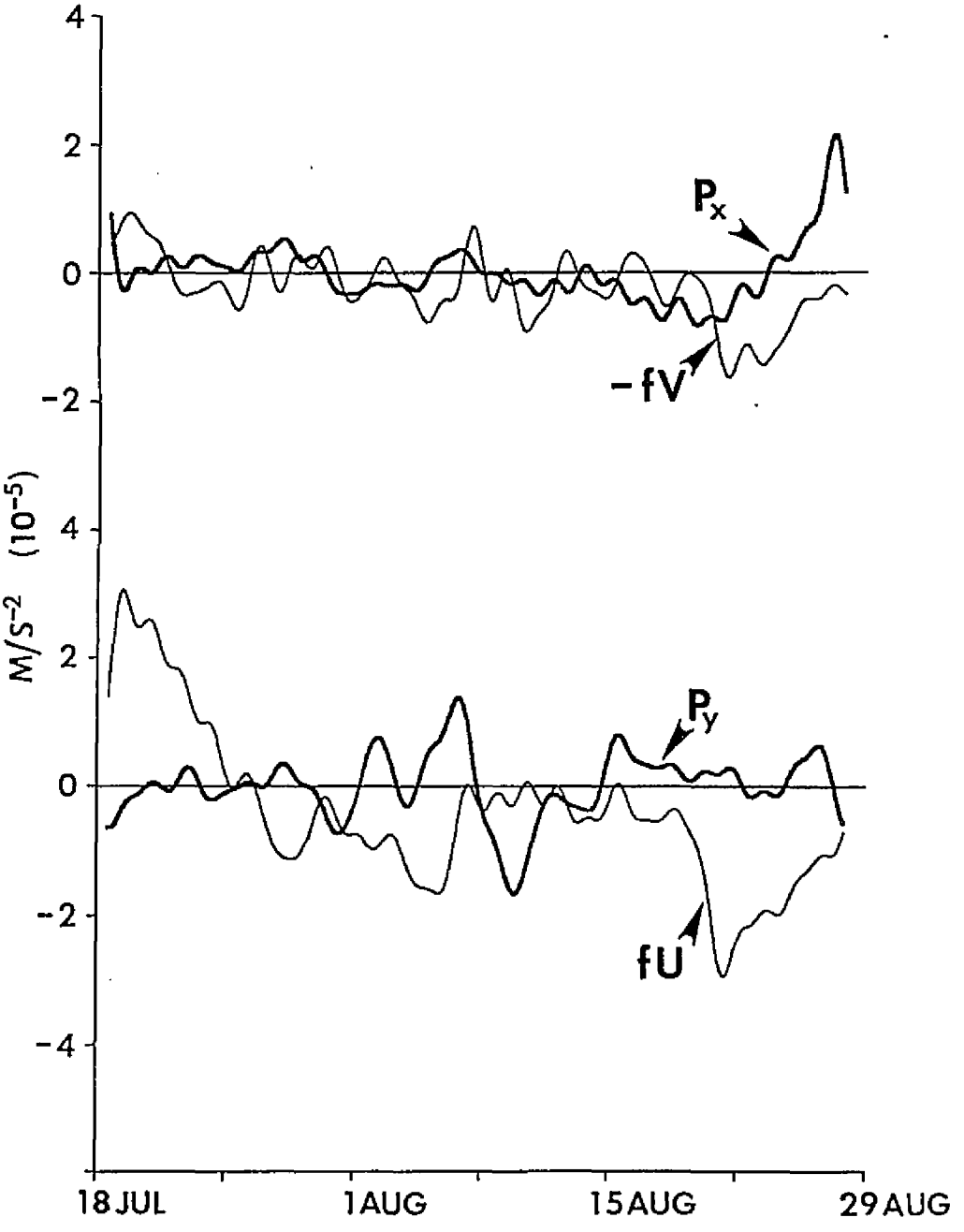

Figure 44. Alongshelf (upper) and cross-shelf (lower) momentum equation terms for CM8 from MS3.

large enough to contribute significantly to a partial balance. The alongshore currents were too great for the across shelf pressure gradient to balance the coriolis force (Figure 44) during the first and last quarter of the record. The pressure gradient increased and the alongshelf currents were of the proper size and sign to balance the coriolis force midway through the deployment. The best approach to geostrophic balance observed in any of the three records occurred during the first week in August. For the remainder of the deployment, the residual terms were very important to the dynamic balance.

Discussion

A statistically-significant, counterclockwise mean flow of 0.04 to 0.07 m/s, was present over the inner shelf from 18 July to 28 August 1981. Cold front passages were limited, only two actually crossed the shelf, and much weaker than the winter and spring deployments. Prevailing winds were from the southeast. The wind variance was largest at the lowest frequencies. The current fluctuations were largest at frequencies below 0.1 cpd, but currents were coherent with the winds at 0.2 to 0.5 cpd. The currents were spatially coherent at these longer time scales. These current fluctuations attained speeds of $\pm$0.1 m/s and flowed roughly parallel the isobaths. When winds were from the east or south, currents flowed counterclockwise around the northwest corner of the inner shelf.

DISCUSSION

The data from these three seasonal current meter deployments, along with the supporting data, are not sufficient to describe the total variability of the LMAS inner shelf circulation. Flow, however, can be characterized for these definite time periods. A better understanding of inner shelf circulation and a comparison of seasonal circulation patterns can be derived from their analysis.

Early winter mean inner-shelf flows are westward along the Mississippi-Alabama barrier islands and southward along the Chandeleur Islands. This mean circulation is interrupted by multiple, sustained flow events in the opposite direction, i.e. clockwise flow, generally in during a cold front passage.

During the winter deployment the cross-shelf pressure gradient was mainly determined by water levels either set up or down against the coast in response to winds. The coriolis force due to alongshore currents was too small to balance the pressure gradient. Other forces, which could be estimated from the data, did not balance the pressure gradient force. The dynamics of this region could not be described using the available data.

The mean circulation during the spring flowed in a different pattern. At the deeper moorings, the flow was onshore. At the shallower moorings, the flow was eastward. Currents at the shallower moorings may have been influenced

by the tidal passes between barrier islands. Mean currents continued to be shelfward from Chandeleur Sound.

The summer deployment utilized the fewest moorings and resulted in the shortest usable record. Counterclockwise statistically-significant alongshore mean currents were present.

Variations in the currents during the three deployments were very similar. Two descriptions of variance, the total subtidal variance and the EOF partitioning of the variance, were consistent with quasi-parabathic flow. When flow was counterclockwise there is also an onshore flow, toward the Mississippi Sound. When clockwise flow occurred the cross-shelf flow was seaward. The circulation variability is correlated with the cycle of cold front passages. Prefrontal southeasterly winds force shelf waters toward the northwest and drive a counterclockwise circulation on the inner shelf. The water level rises in the corner region. Some of this water flows through tidal passes into the back barrier sounds. The winds quickly shift through the south and west as fronts pass. The water slope inside the sounds exceeds a balance with the wind stress and shelfward flow begins. This return flow precedes the generally northwesterly post-front winds that force a flow out of the corner region. The nearshore water level is set down and the counterclockwise inner shelf flow ceases or sometimes reverses direction.

Water level drops in the back barrier bays and sounds as the fronts pass. This water has two possible avenues of

escape: southward behind the Chandeleur Islands and onto the shelf via Breton Sound or through the tidal passes between the Mississippi-Alabama barrier islands.

Both appear to be used to varying degrees dependent upon the post-front wind direction and duration. If a front passes through the region quickly, winds rotate clockwise from prefrontal southerly winds through the post-frontal northerly wind and back to southeasterly interfrontal winds. The currents on the inner shelf weaken during the wind shift but strengthen again as the wind direction rotates to southeasterly. This scenario occurred on 23 November (Figure 14).

If the post-front wind direction remains from the north or the northeast for two or three days, alongshelf currents south of the Mississippi-Alabama barrier islands become weak and confused. Cross-shelf currents flow offshore. Alongshelf currents immediately seaward of the Chandeleur Islands reverse and flow to the north. Water in the bays and sounds flows southward via the Chandeleur Sound-Breton Sound route. This scenario is consistent with the flow from 17 November until 20 November. The inner shelf currents rotates to a counterclockwise pattern as the wind direction returns to the interfrontal direction.

A third pattern occurs when post-frontal winds remain from the northwest for two or four days. The alongshore flow reverses over the entire inner shelf while the cross-shelf flow is directed offshore. Bay and sound water moves

eastward onto the LMAS through the channel at the north end of the Chandeleur Islands and southward between the Mississippi-Alabama barrier islands. This situation occurred from 27 to 30 November.

The circulation during the short winter deployment was a collection of variations on these scenarios. There was even another situation that resulted in clockwise flow on the inner shelf. Fronts associated with rapidly moving polar air mass outbreaks (i.e. 14 to 18 December), pushed through the region very rapidly. The average locations of high and low atmospheric pressure cells created winds that oscillated from the southwest to northwest. The currents reversed over the entire region.

Wind regimes were different during each season. Early winter winds were primarily from a northerly direction. Southeasterly spring winds were driven by the strengthening Bermuda high pressure system. Frontal passages occurred regularly during both seasons. Winter energy levels were higher at low frequencies while spring energy levels were higher in the 0.2 to 0.3 cpd band associated with the fronts. The fronts were more regular during the spring. The winter fronts were aperiodic, which resulted in the spectrum energy being spread over a wide frequency band. Summer winds were much weaker than during the other seasons. Only two fronts actually crossed the shelf. The wind spectrum was redder than during the other seasons. The clockwise rotating portion of the seasonal spectra, at frontal frequencies, was

more energetic than the counterclockwise rotating portion.

The number of fronts per day (fpd) occurring during the winter and spring deployments were 0.22 and 0.19, respectively. These numbers are slightly than the 0.25 fpd avérage reported by Fernandez-Partagas and Mooers (1975), but larger than the November-December average of 0.13 fpd and the April average of 0.15 fpd reported by Dimego et al (1976). Henry (1979) suggested 0.17 fpd was representative of November and December and 0.22 fpd of April. Such descriptive numbers are difficult to compare between studies. Because these studies give no information concerning the range of expected values, frontal occurrence during this study can only be described as normal.

Data from all three deployments were used in an attempt to estimate the vertically-integrated momentum balance over the inner shelf. The results were unsatisfying. The residual terms were always an important part of the balance. These terms, a combination of the baroclinic pressure gradient force and the generalized Reynolds' stresses, were terms that could not be determined directly from the data. The poor quality of the salinity data from adjacent moorings made it impossible to estimate the proper horizontal baroclinic pressure gradient. Using scale analysis, it can be seen that a cross-shelf density difference of 1 kg/m^3 over a distance of 10 km would be of the correct magnitude to balance the coriolis and baroclinic pressure gradient forces estimated for the inner shelf (Appendix II). The

presence of light water near the coast, as is normal, is not always consistent with a baroclinic pressure gradient force of the same sign as the residuals.

Seasonal flow on the inner shelf was characterized using data from three seasonal current meter deployments. The currents generally flow along-shore. The flow is either clockwise or counterclockwise around the inner shelf region. The winds accompanying frontal passage are associated with the flow reversals. The extent and duration of the reversals seem dependent on the duration and direction of the post-front winds. The data were highly non-stationary. Seasonal mean flow patterns are, therefore, difficult to predict.

4. PROCESSES FOR SEDIMENT DISPERSION

SURFACE SEDIMENT DISTRIBUTION

The surface sediment distribution has been described by Ludwick (1964), Upshaw et al (1966), Doyle and Sparks (1980), and the U.S. Department of the Interior (1982), U.S. Department of Commerce (1985) for the entire LMAS region, and for the western portion by Scruton (1956), Shepard (1956), and Kindinger et al (1982). In each of these maps, excluding the barrier island and estuarine sediments, there are two major sedimentary provinces: the Mississippi Province and the Eastern Gulf Province. The former, composed of silt and clay sediments, is attributed to the St. Bernard prodelta of the Mississippi River and will be referred to here as prodelta clays, while the latter, a well sorted, clean, fine quartz sand, will be referred to as the eastern sands.

Most of the previously mentioned surficial sediment maps describe the sediment sizes as either sand, silt or clay, or some combination of the three. Only Ludwick (1964) described the grain size in greater detail and categorized the sediment types (Figure 45). He used data from heavily sampled multiple cross-shelf transects to produce cumulative frequency curves for the two main sediment types characteristic of the shelf as for the other barrier island and estuarine sediments (Table 13). The eastern sands are a relict deposit, but are still mobile; the prodelta clays

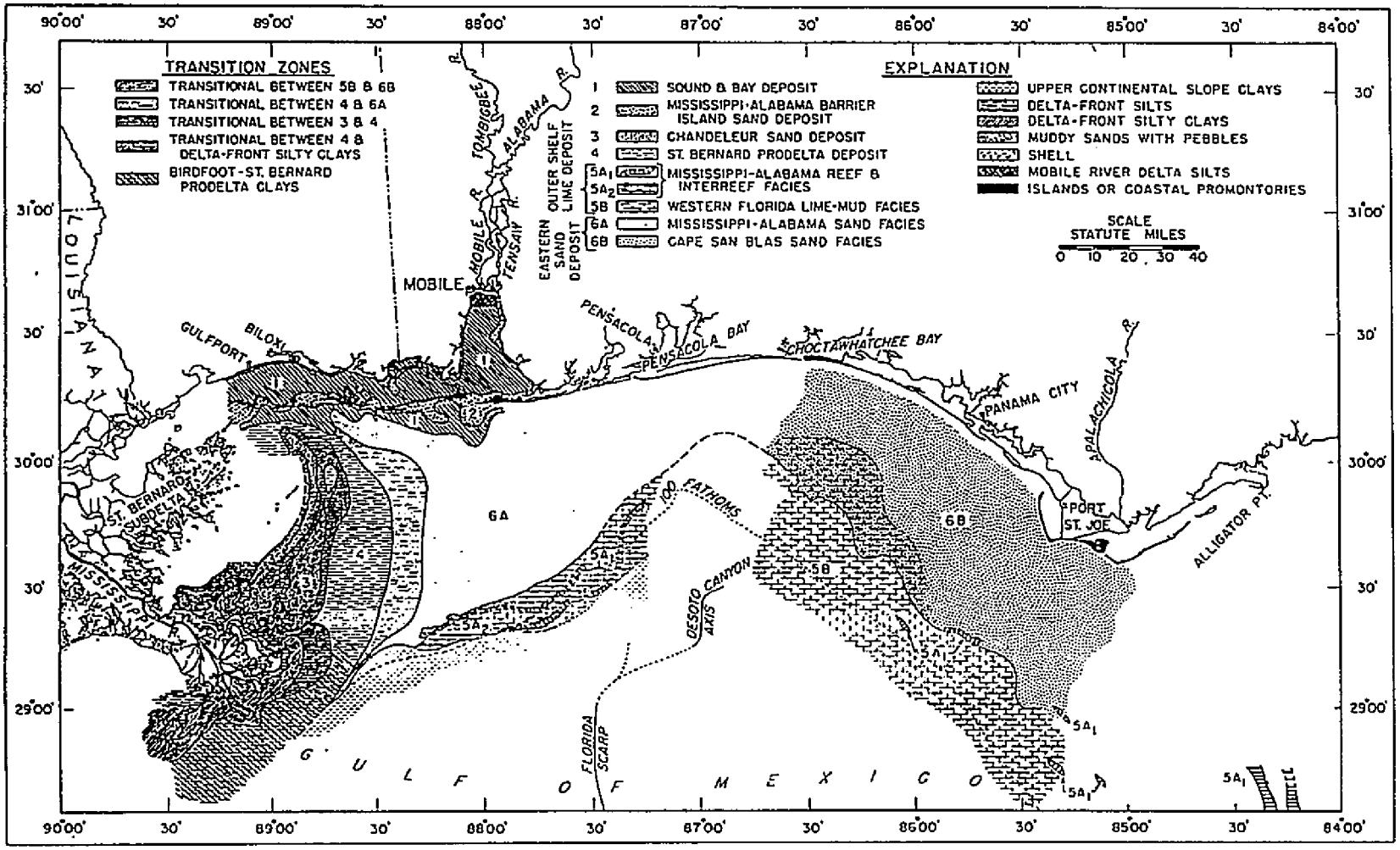

Figure 45. Sediment distribution on the LMAS (after Ludwick, 1964).

Table 13. Sediment grain sizes determined from the cumulative frequency data in Ludwick (1964).

	Cumulative percent				
	10	25	50	75	90
Chandeleur Islands	0.18	0.15	0.11	0.09	0.075
Miss.-Al. Barrier Is.	0.35	0.28	0.20	0.18	0.15
Sounds and Bays	0.0625	0.018	0.002	0.0003	-
St. Bernard Prodelta	0.02	0.006	0.0015	0.0003	-
Eastern Sands	0.30	0.24	0.18	0.02	0.15

overlay the eastern sands (Kindinger et al, 1982). There is a region of mixing between the two sediment types, extending in a north-south concave westward arc east of the Chandeleur Islands (Figure 45). This region of mixing corresponds very well to the heavy mineral assemblage limits of Fairbank (1962).

SEDIMENT TRANSPORT MECHANISMS

Three transport mechanisms will be investigated, tidal and subtidal currents and wave induced resuspension.

Tides in the Gulf of Mexico are primarily diurnal (Marmer, 1954). Tidal amplitudes in the LMAS region are on the order of 0.3 m (Seim et al, 1987). Tidal currents, viewed as fluctuations about a mean flow, can be filtered from a current time series as a zero mean process. The rms speeds (standard deviations) along the major principal axes of the tidal-band currents from the inner shelf bottom current meters discussed in Chapter 3 have been calculated (Table 13). Peak bottom tidal currents, estimated as twice the rms speed along the major axes of the tidal band currents,are between 0.05 and 0.16 m/s for the inner shelf currents. Only at CM1B do the magnitudes reach over 0.2 m/s and this is because of the topographic channelization in the vicinity of the meter. Seim et al (1987) performed harmonic analysis of the four main components of the tidal currents using these same meters (Table 14). Even when acting in concert, the four components (K_1, O_1, M_2, S_2) produce

Table 14. Bottom tidal currents and tidal harmonic current amplitudes for inner continental shelf currents. Major axes rms values (this study) and harmonic constants (Seim et al, 1987) in m/s.

	BOTTOM RMS VALUES			TIDAL HARMONIC AMPLITUDES			
METER	MS1	MS2	MS3	K_1	O_1	M_2	S_2
CM1B	0.116	0.086	---	0.103	0.100	0.037	0.025
CM2B	0.082	0.078	0.056	0.071	0.066	0.026	0.018
CM4B	---	0.050	0.038	0.029	0.029	0.017	0.007
CM5B	0.032	---	---	---	---	---	---
CM6B	0.038*	0.046	---	0.042+	0.019+	0.017+	0.010+
CM7B	0.027	---	0.050	0.031	0.018	0.011	0.008
CM8B	0.039	0.062	0.067	0.067	0.027	0.008	0.003

* Record length one half of the other MS1 deployment

+ Questionable results (Seim et al, 1987)

currents of 0.1 m/s on the inner shelf and 0.26 m/s at CM1 (Seim et al, 1987).

Critical erosion speeds for the 25% and 75% sediment sizes (Table 13) of the Eastern Sands were predicted to be 0.36 and 0.42 m/s, respectively, using the empirical formula

$$u_c = 122.6\ d^{0.29}$$

for the critical erosion speed, u_c, 1 m above the bottom, as a function of grain size, d, in centimeters (Miller et al, 1977). Allen (1965) predicted an approximately a 0.38 m/s critical erosion speed at 1 m above the bottom using a Sundborg-type diagram for the same size sediments. The bottom current meters were moored 1.8 m off the bottom. Using the tidal current estimates from these meters as conservative speed estimates, there should be no sediment movement of the eastern sands induced by tidal currents.

The prodelta clays probably do not behave as spheroid quartz grains and therefore the same graphical and empirical techniques may not be the proper tools to use to estimate critical erosion speeds for the smaller sediment grain sizes.

The cohesive nature of fine grained sediments makes it difficult to determine the boundary shear stress or an erosion speed needed to move them. This cohesiveness is a function of the organic material content, water content, texture and composition of the sediments (Drake, 1976). Postma (1967) demonstrated the dependence on composition and

water content for sediments smaller than 0.1 mm, and that the speed needed to transport silts and clays is smaller than the speed needed to erode them. Postma also presented a relationship between mean erosion speed at 0.15 m above the bed for sediments less than sand size and water content. The critical erosion speed rapidly increases as fine grained sediments dewater. This extends the Sundborg-type diagram over smaller grain sizes. Although these speeds cannot be used directly in this study, it certainly follows that speeds at 1.8 m above the bed would need to be much greater than the 0.18 m/s needed to erode unconsolidated prodelta cohesive sediments estimated from Postma's relationship.

Strong subtidal bottom currents are episodic, but can reach and maintain speeds of 0.2 m/s (Chapter 3) for durations of two to five days. The subtidal current speeds alone are too low to move the eastern sands.

Waves in this region are relatively low. Wave observations (U.S. Department of Commerce, 1972) are statistically similar to hindcast data for a 20 year period (U.S. Army, Draft Report) (Table 15). The observed mean significant wave height is only 1 m (3ft), as are mean hindcast significant wave heights. The significant hindcast wave periods are 5.1 to 5.5 s. The most frequent direction is from the southeast. The largest hindcast wave heights and periods are 3.6 to 4.7 m and 10.0 to 11.1 s. These statistics are very similar to those calculated from observed data, 4.9 m heights and 10.0 to 11.0 s periods. The

Table 15. Unpublished hindcast wave statistics (U.S. Army, Draft Report) and observed data (U.S. Department of Commerce, 1972) for the LMAS region.

	WIS STATIONS				OBSERVED
	25	26	27	28	DATA
			Mean		
Significant Height (m)	1.1	1.0	1.1	1.1	1.0 (3ft)
Period (s)	5.5	5.1	5.4	5.3	-
Most Frequent Direction*	135.	135.	135.	135.	-
			Largest		
Significant Height (m)	3.9	3.6	4.7	4.2	4.9 (16ft)
Associated Period (s)	10.0	10.0	11.1	10.0	10.-11.
Average Direction*	104.	140.	138.	140.	-

WIS Station Locations:
25 - 29.5°N 88.5°W
26 - 30.0°N 88.5°W
27 - 30.0°N 88.0°W
28 - 30.0°N 87.5°W

Observed Data Region Center: 29°40'N 88°30'W

* Wave direction is the direction from which the waves arrive.

direction of the largest hindcast wave is from the east-southeast or southeast.

The depth at which a specified sediment size will move because the bottom wave orbital speed reaches the critical erosion speed, and the frequency of occurrence of such events was estimated from hindcast wave periods and heights (U.S. Army, Draft Report) (Figures 46 and 47). A combination of wave heights and periods capable of moving mean size eastern sand grains 70% of the time were determined using hindcast wave statistics from a station that lies in the eastern sands and linear wave theory (Figure 46). Wave heights less than 1 m, with periods of 4-5 s and wave heights of 1-2 m with periods of 4-6.5 s can move 0.18 mm sediment in water depths of 26 meters. Over 95% of the hindcast waves have periods of 7.5 s or less and would not move sediment in water deeper than 34 m. Conversely, less than 5% of the waves have periods greater than 7.5 s and heights between 1 and 4 m. These waves, though, are able to move sediment in waters up to a maximum depth of 64 m.

Mean current speeds probably do not exceed the unconsolidated threshold speed of Postma (1967) in either the tidal or subtidal band. The combination of the currents in the two bands may occasionally be sufficient to cause erosion. Wave orbital speeds can exceed this critical speed near the bed (see above). If a characteristic critical speed is assigned for a given sediment type, the formula of Komar and Miller (1975) can be used to predict the depth at which

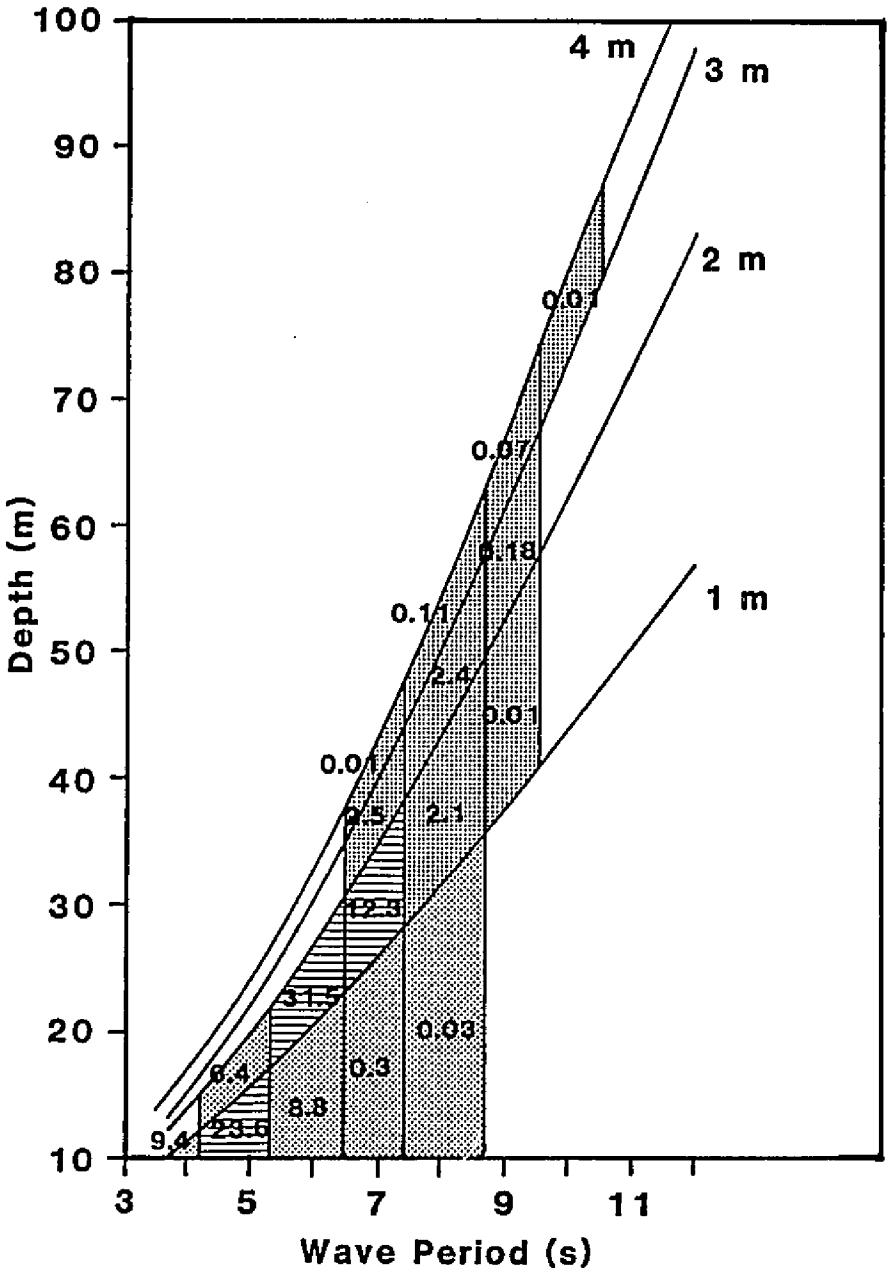

Figure 46. Depths of sediment movement due to wave orbital motion for median eastern sand sediment size grains. Wave periods and heights are from U.S. Army, Draft Report, and depths of sediment motion determined after Komar and Miller (1975). Wave categories with greater than 10% frequency of occurrence are cross-hatched rather than stippled.

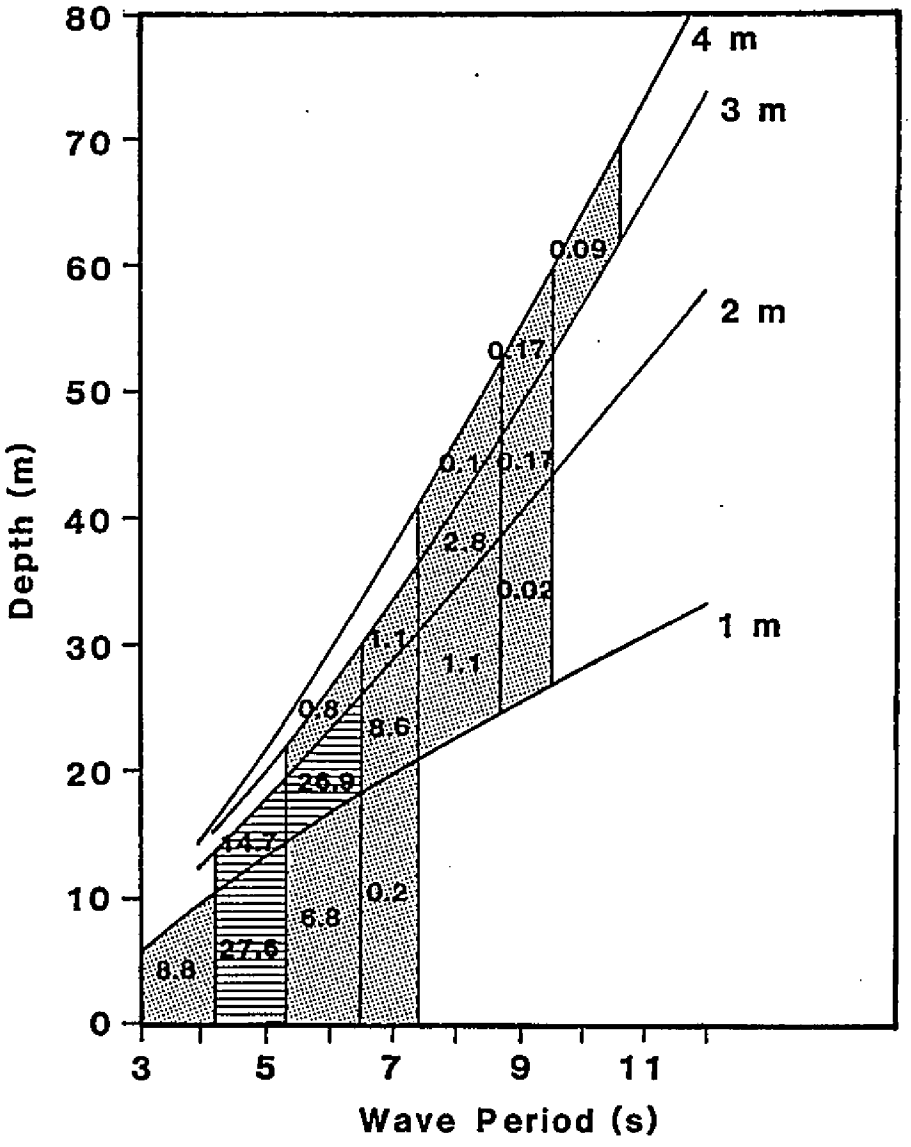

Figure 47. Depths of sediment movement due to wave orbital motion for prodelta clay size grains with an estimated critical erosion speed of 0.1 m/s. Wave periods and heights are from U.S. Army, Draft Report, and depths of sediment motion determined after Komar and Miller (1975). Wave categories with greater than 10% frequency of occurrence are cross-hatched rather than stippled.

this sediment moves for specific wave period and height combinations. These calculations were performed using a critical speed of 0.1 m/s and wave periods and heights observed at WIS station 25 (29.5°N, 88.5°W) (Figure 47). The results should be applicable to the transport of the prodelta clays. Over 67% of the waves have heights less than 1 m and periods of 4-5 s, or heights 1-2 m and periods 5.2-7.5 s. Over 99% of the waves have heights less than 3 m and periods less than 8.7 s. Such waves achieve the critical near-bottom speeds only in depths less than 50 m. Conditions that attain these speeds in water depths greater than 50 m occur less than 1% of the time. Longer wave periods than those commonly occurring in the Gulf of Mexico are required to move sediment in 100 m water depth, e.g. hurricane waves.

Komar and Miller's (1975) scheme to assess sediment movement assumes that the sediment behaves as spheroidal quartz grains. This is a reasonable assumption for the eastern sands. The eastern sands will move in water depths up to 60 m under the expected wave conditions. Most of the resuspension, though, will occur in less than 30 m of water. If little compaction occurs and a wave orbital erosion speed approximately for the same as the eastern sands is assumed, then erosion of the prodelta clays occurs in up to 80 m water depth under non-hurricane waves. Most of the movement, though, takes place in less than 40 m depth. Sahl et al (1987) reported erosion speeds of 4 cm/s for recently deposited fine grained sediments on the Texas shelf. If this

is characteristic of prodelta clays, a fine drape of unconsolidated sediments should be mobile out to 100 m water depth under commonly occurring waves.

Wave data were available from from a National Data Buoy Office offshore buoy concurrent with the winter, MS1, and spring, MS2, inner shelf current meter deployments. The data consisted of significant wave height and dominant periods determined from hourly wave spectra estimated from 8.5-minute data records. The raw data were low-pass filtered with a cutoff of 0.6 d and resampled at 0.125 d increments. Waves recorded at the buoy (BY) were assumed to be due to the wind field at BY and to propagate in the direction of the winds at BY. Winds have been shown to be very coherent over the LMAS region (chapter 3). Therefore, it was assumed that wind conditions and, consequently, wave periods and directions were similar on the inner shelf. A transformation of wave heights at BY to wave heights in water depths appropriate to the inner shelf current meters (see Chapter 3 for locations and depths) required a reduction of only 5 to 10% (U.S. Army, 1977).

If the subtidal currents are too weak to initiate sand size sediment movement and the wave orbitals are assumed to be symmetric, then the combined wave-current speeds might be sufficient to initiate motion with only the subtidal flow contributing to subsequent net advection. Note, however, that the tidal currents are also assumed to contribute no net displacement on the shelf. They will be ignored as

transport agents although they may contribute to resuspension. Wind direction change at cold front passage is marked by a rapid clockwise rotation. Wave heights and periods are greatest during the prefrontal winds and during other high speed events of multiple day duration. Frontal passage usually results in amplitude reduction of the longer period higher waves produced by the southeast prefrontal winds (figures 48 and 49).

Waves heights of 1 to 2 m and periods greater than 6 s occurred during one-third of the MS1 deployment. Seventy-five percent of the occurrences of high waves were accompanied by bottom currents flow to the west at CM8. Three periods of eastward flow occurred during episodes of high wave conditions. The highest wave conditions (greater than 2-meter heights and 7-second periods) move eastern sands in up to 30 m water depths. Moderately high wave conditions can move eastern sands in 20 to 25 m water depths. Flow is coherent between CM8B and CM2B. Assuming alongshore currents at CM2B are representative of these at similar depths at the southern end of the Chandeleur Islands, the direction of movement of pro delta clays can be estimated.

Prodelta clays generally move southward at times of highest wave conditions. Albeit a conservative estimate, depths of movement are less than 40 m. Flow to the north along the Chandeleur Islands accompanies wave conditions able to move sediments at depths up to 30 m. Such wave

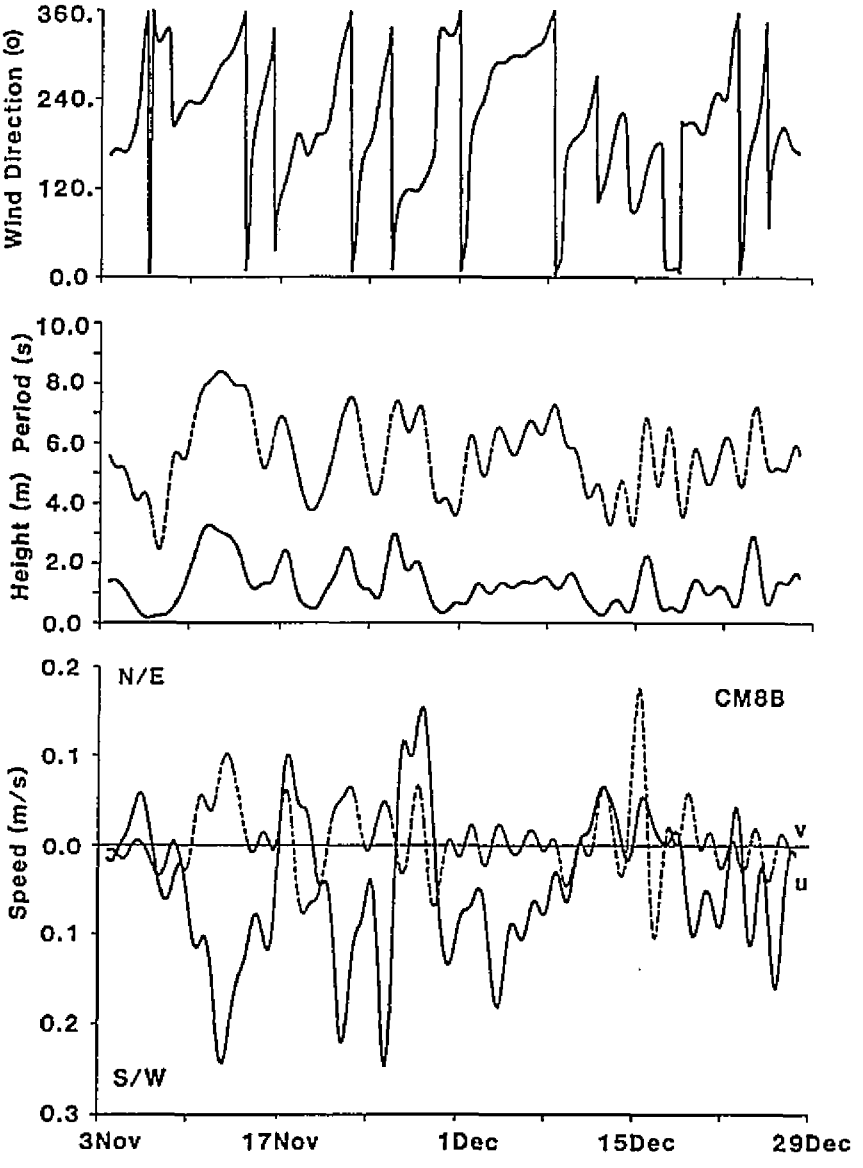

Figure 48. Time series of low passed BY wind direction, dominant wave period, significant wave height, and the bottom currents at CM8 for MS1.

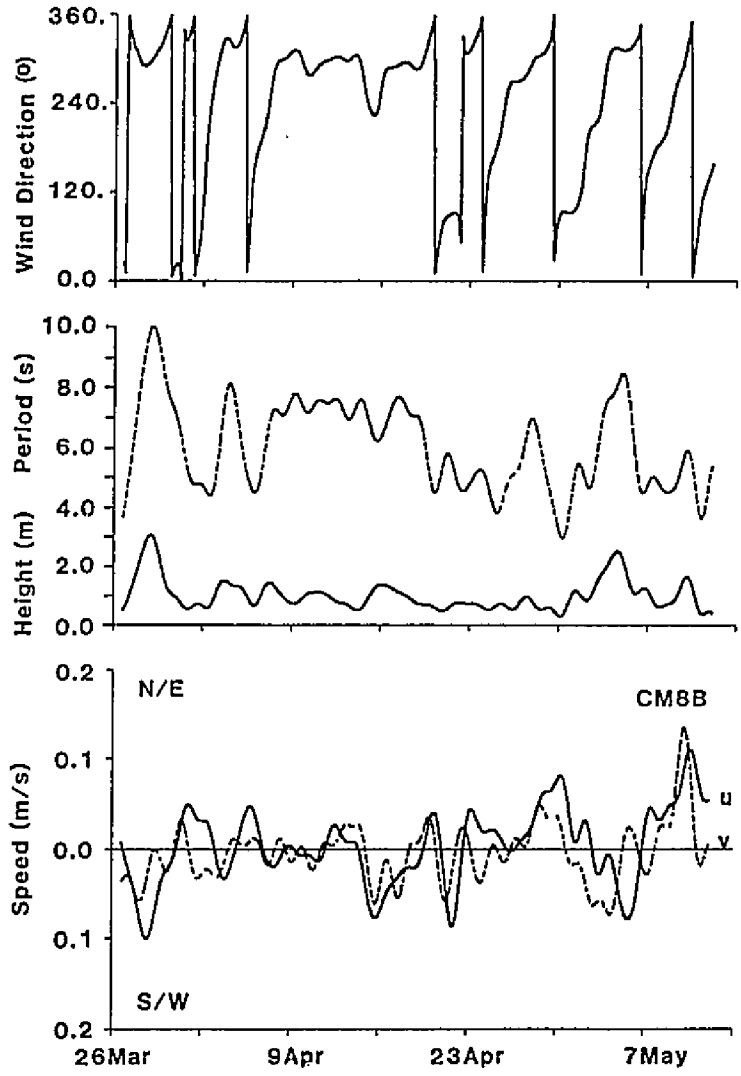

Figure 49. Time series of low passed BY wind direction, dominant wave period, significant wave height, and the bottom currents at CM8 for MS2.

conditions enabled flows to carry prodelta clays north along the Chandeleurs or eastern sands east along the Mississippi-Alabama barrier islands during 10% of the deployment.

Bottom currents at CM8 flow westward 90% of the time when there are long wave periods and large wave heights during MS2 (Figure 49). The times of high wave conditions correspond to interfrontal or prefrontal southeasterly or southerly wind directions. Seven second periods and 2-meter wave heights will move eastern sands in depths up to 30 m while 6 s, 1-2 m waves move sediment in 20 m water depths. Subtidal flows to the east occur at the current meter moorings when wave conditions are low, i.e. periods less than 5 s and 1 m or less heights. Sediment movement is limited to depths less than 10 m under these conditions.

Highest wave conditions occurred when subtidal near bottom flow along the Chandeleurs was to the south. Sediment movement was probably also in this direction, but limited to depths less than 50 m. Less extreme, but still high, wave conditions also result in southward sediment transport in water depths less than 25 m. Wave conditions during northward bottom flow limit sediment movement to depths less than 15 m. In general, during the MS2 deployment, little sand size sediment moved eastward and few prodelta clays moved northward at depths greater than 10 m.

DISCUSSION

Subtidal currents are capable of transporting sediment on

the LMAS, but not of eroding sediment once it is deposited. Between the barrier islands, where tidal currents are channelized, there are larger tidal current speeds than on the inner shelf. These currents may be capable of resuspending unconsolidated, recently deposited sediments. On the broad flat shelf, the tidal currents are much too weak to erode either the sand-size particles or any consolidated finer particles.

Wave activity on the the shelf is of low energy (periods of less than 10 s and significant wave heights of less than 2 m). These relatively low-energy combinations of wave periods and heights can produce orbital speeds at the bottom that are capable of eroding sediment. Niedoroda and Swift (1981) found, that wave orbital motion resulted in no net movement in water depths greater than 10 m on the coast of Long Island. In the LMAS region, 10 m depth is approximately the depth limit of the barrier island sands (Ludwick, 1964).

Shelf sediment transport requires resuspension by the shear stress due to the interaction of wave orbital motion and the subtidal current. The tidal currents are ignored in this conservative analysis although they probably contribute to resuspension. Current velocities in the tidal band are considered a zero mean process. Net advection has been relegated to the subtidal band. Times of greatest wave period and height during the MS1 and MS2 deployments, and consequent sediment movement at the greatest water depths, occurred during counterclockwise subtidal circulation over

the inner shelf. Sediment moved westward along the Mississippi-Alabama barrier islands and southward along the Chandeleur Islands. Sediment movement was moved out to depths, at least, 40 m.

Wave conditions on the shelf during frontal passages were usually much too low to affect the bottom in water greater than 10 m deep. Yet, these wave periods of 5-6 s and heights of 1 m eroded bottom sediments in the shallow sounds and bays. The resultant turbidity fronts evident in the satellite images presented by Schroeder et al (1985) and Abston et al (1987). Sediment that is transported to the shelf from the bays and sounds during cold front passage is advected over the shelf by the subtidal flow. Resuspension of shelf sediments usually occurs when interfrontal and prefrontal winds produce long period waves. These are higher than normal. They occur concurrent with counterclockwise flow on the inner shelf. A net counterclockwise sediment transport results. The bay and sound sediments that are flushed to the shelf during cold front passage will ultimately be moved westward along the Mississippi-Alabama coast then southward along the Chandeleur Islands. They reenter the sounds and bays during strong easterly wind conditions.

In order to investigate the possibility that resuspended bottom sediments move onshore, a Lagrangian analysis was performed using the Eulerian current meter data. The bottom current meter data for all the deployments were chopped into

discrete time intervals that corresponded to the correlation time scales of each current record (Csanady, 1983). These correlation time scales were the same ones used to determine the standard errors about the means (see chapter 3). The mean flows calculated from these discrete segments of current data are independent and can provide independent estimates of Lagrangian-displacement. The probability distributions for the near-bottom Lagrangian displacement at CM8 during the MS1 and MS2 deployments were calculated (Figure 50). An onshore, westward transport was highly probable during deployment MS1, while an eastward displacement with no significant on-offshore transport was most probable during deployment MS2. Probability distributions from other near-bottom sites gave similar results.

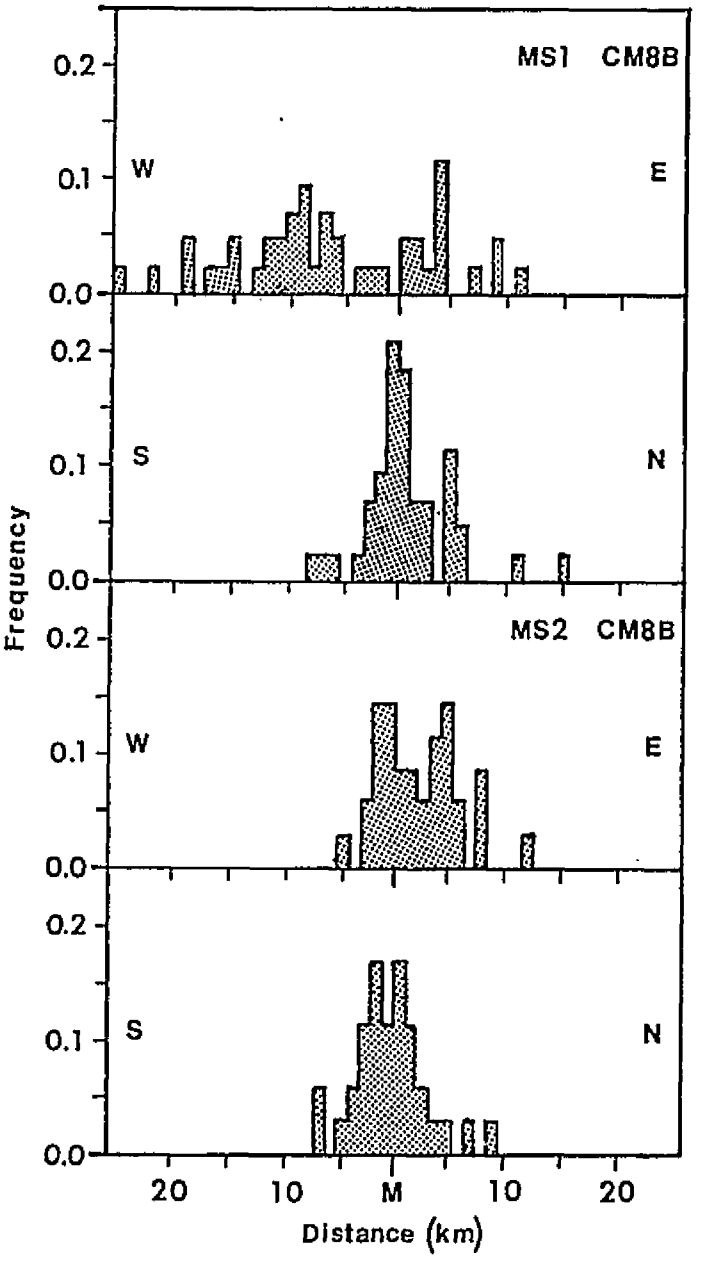

Figure 50. Probability distributions for the alongshore and across shore bottom velocity components at CM8 for both the MS1 and MS2 deployments. Correlation time periods are 1.25 d.

5. SUMMARY

The circulation on the LMAS and adjacent regions has been characterized using historical hydrographic data and current meter data. Generalized seasonal circulation patterns have been proposed (Figure 51). These patterns are based on objective data over the inner shelf, outer shelf, and upper slope. The midshelf patterns are more subjective.

Westward flows on the inner shelf, outer shelf and upper slope in the spring and summer (Figure 51) are interpreted as the northern and southern portions of closed cyclonic and anticyclonic circulation cells, respectively. Spring and summer midshelf flow is eastward. This is consistent with flow around two counter-rotating circulation cells. The offshelf flow over the eastern LMAS shelfbreak has three possible fates. Some shelf water flows westward along the upper slope and may either recirculate around the anticyclonic cell, moving onshelf just east of the Mississippi Delta, or continue west across the Delta front. Some water moves offshelf and then up the De Soto Canyon, flowing onshore and then westward over the inner shelf. Finally, some may continue to flow southeastward along the eastern flank of the Canyon. A convergence on the western LMAS must occur between the onshore flow just east of the Delta and inner shelf flow moving south along the Chandeleur Islands. This water must then move eastward, across the LMAS

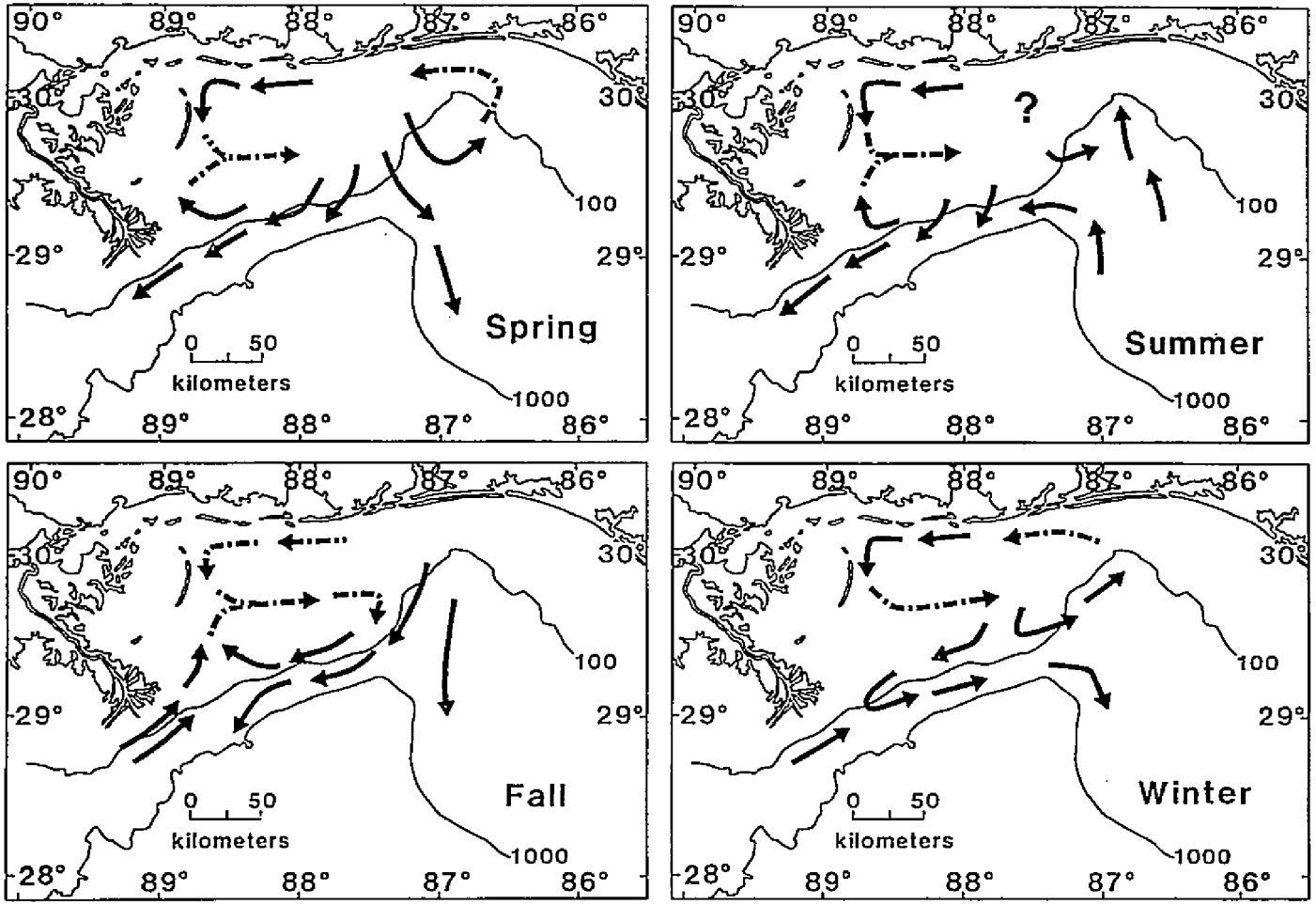

Figure 51. Generalized circulation on the LMAS, for the spring (upper left), summer (upper right), fall (lower left), winter (lower right). Solid lines are objective, broken lines are subjective. Arrows indicate direction of flow.

toward the De Soto Canyon and the region of shelfbreak exchange.

The observed mean inner shelf flow patterns are consistent with wind-driven flow. Mean monthly winds, for an 11-year period (1974-1984), were from an eastern quadrant during most of the year (Schroeder and Wiseman, 1985). The mean easterly winds during the fall can be assumed to drive an inner shelf circulation similar to that observed in the spring and summer. At the same time, flow from west of the Delta turns onto the shelf just east of the Delta (Figure 51). The principal pattern of two counter-rotating cells on the shelf with onshore flow to the west and offshelf flow to the east remains.

The anticyclonic circulation cell over the outer shelf and upper slope is not present during the winter. Winter shelf circulation appears to consist of a single cyclonic cell. Currents are eastward over the upper slope and westward over the inner shelf (Figure 51). There is weak offshelf flow all along the shelf-break in winter.

Spring discharge from the Mississippi River disperses eastward along the shelf-break. A ridge of high dynamic topography results on the shallow isobaric surfaces. Circulation is clockwise around this ridge, eastward over the outer shelf and westward over the upper slope. Outer shelf and slope flow during summer and fall, is a continuation of that associated with spring runoff conditions. Most of the fresh water is gone from the outer

shelf by winter. Weak offshelf and eastward flow over the outer shelf and upper slope are consistent with the dynamic topography.

The inner shelf circulation is parabathic cyclonic flow interrupted by aperiodic reversals associated with northwesterly winds. Peak current speeds observed during winter, spring and summer exceeded 0.3 m/s in either alongshore direction. Post-front wind direction and duration appeared to be related to the degree of spatial coherence in alongshore flow. Normal circulation relaxed as cold fronts moved through the region and wind directions shifted. Fast-moving fronts tended only to interrupt the existing flow, but longer periods of post-front winds from the northwest reversed the inner shelf flow direction.

Wave-induced sediment resuspension and advection by subtidal bottom currents are both necessary for net sediment transport on the inner shelf. Long-term hindcast wave statistics from the shelf were analyzed. Sediment resuspension during high wave conditions can occur in water depths of 40 m or less. Highest wave conditions, with durations on the order of hours per year, may resuspension sediment in up to 80 m water depth. Sediment transport occurs primarily during prefrontal winds conducive to long waves and cyclonic inner shelf flow in the winter and spring. Winds during the summer are weaker. Locally generated wind waves would resuspend shelf sediment at shallower water depths. Outer shelf and upper slope

sediments are most likely to be resuspended only by hurricane condition waves or, possibly, by direct influence of the Loop Current.

Continued investigation is needed to understand the inner shelf-outer shelf exchange and midshelf flow. Observed shelf-break exchange is not documented by in situ current measurements, nor are the time and spatial scales of outer-shelf variability understood.

REFERENCES

Abston, J.R., S.P. Dinnel, W.W. Schroeder, A.W. Schultz, and Wm.J. Wiseman, Jr., (1987) Coastal sediment plume morphology and its relationship to environmental forcing: Main Pass, Mobile Bay, Alabama. Coastal Sediments '87', ASCE, New Orleans, 1987.

Allen, J.R.L. (1965) Origin and characteristics of recent alluvial sediments. Sedimentology, 5, 89-191.

Amorocho, J. and J.J. DeVries, (1980) A new evaluation of the wind stress coefficient over water surfaces. Journal of Geophysical Research, 85, 433-442.

Amorocho, J. and J.J. DeVries, (1981) Reply. Journal of Geophysical Research, 86, 4308.

Austin, G.B., Jr. (1955) Some recent oceanographic surveys of the Gulf of Mexico. Transactions, American Geophysical Union, 36(5), 885-892.

Beardsley, R.C. and W.C. Boicourt, (1981) On estuarine and continental-shelf circulation in the Middle Atlantic Bight. in B.A. Warren and C. Wunsch, (eds.), Evolution of Physical Oceanography, Scientific surveys in honor of Henry Stommel. MIT Press, Cambridge, MA. p198-233.

Chuang, W-S., W.W. Schroeder, and Wm.J. Wiseman, Jr., (1982) Summer current observations off the Alabama coast. Contributions in Marine Science, 25, 121-131.

Chew, F., K.L. Drennan, and W.J. Demoran (1962) Some results of drift bottle studies off the Mississippi Delta. Limnology and Oceanography, 7(2), 252-257.

Cochrane, J.D., and F.J. Kelly (1986) Low-frequency circulation on the Texas-Louisiana continental shelf. Journal of Geophysical Research, 91, 10645-10659.

Collier, A., K.H. Drummond, and G.B. Austin, Jr. (1958) Gulf of Mexico physical and chemical data from Alaska cruises. Special Scientific Report: Fisheries, 249, pp47.

Csanady, G.T. (1979) The pressure field along the western margin of the North Atlantic. Journal of Geophysical Research, 84, 4905-4914.

Csanady, G.T. (1983) Dispersal by randomly varying currents. Journal of Fluid Mechanics, 132, 375-394.

Curray, J.R. (1960) Sediments and history of the Holocene transgression continental shelf, Northwest Gulf of Mexico. In: F.P. Shepard, F.B. Pleger, and T.H. Van Andel (eds.), Recent sediments, northwest Gulf of Mexico, American Association of Petroleum Geologists, Tulsa, Ok, p394.

Denbo, D.W. and J.S. Allen, (1984) Rotary orthogonal function analysis of currents near the Oregon coast. Journal of Physical Oceanography, 14, 35-46.

Dimego, G.J., L.F. Bosart, and G.W. Endersen, (1976) An examination of the frequency and mean conditions surrounding frontal incursions into the Gulf of Mexico and Caribbean Sea. Monthly Weather Review, 104, 709-718.

Dinnel, S.P. (1983) Distribution and residence time of freshwater on the west Louisiana and Texas continental shelves. Unpublished master's thesis, Louisiana State University, p89.

Dinnel, S.P. and W.W. Schroeder, in press, Coastal water level measurements: northeast Gulf of Mexico. Journal of Coastal Research.

Dinnel, S.P. and W.J. Wiseman, Jr., (1986) Fresh water on the Louisiana and Texas shelf. Continental Shelf Research, 6(6), 765-784.

Doyle, L.J. and T.N. Sparks, (1980) Sediments of the Mississippi, Alabama and Florida (MAFLA) continental shelf. Journal of Sedimentary Petrology, 50(3), 905-916.

Drake, D.E. (1976) Suspended sediment transport and mud deposition on continental shelves. In: Stanley, D.P. and D.J.P. Swift (eds.), Marine sediment transport and environmental management, Wiley, New York, p127-158.

Drennan, K.L. (1968) Hydrographic studies in the northeast Gulf of Mexico. Gulf South Research Institute, pp110.

Duxbury, A.C. (1962) Averaged dynamic topographies of the Gulf of Mexico. Limnology and Oceanography, 7(3), 428-431.

Ebbesmeyer, C.C., G.N. Williams, R.C. Hamilton, C.E. Abbott, B.G. Collipp, and C.F. McFarlane (1982) Strong persistent currents observed at depth off the Mississippi River Delta. Proceedings 14th Offshore Technology Conference, Houston, Texas, May 3-6 1982, pp259-263.

Fairbank, N.C., (1962) Heavy minerals from the eastern Gulf of Mexico. Deep-Sea Research, 9, 307-338.

Fernandez-Partagas, J. and C.N.K. Mooers, (1975) Some front characteristics over the eastern Gulf of Mexico and surrounding land areas. Final report to BLM under contract 08550-CT4-L6.

Goldstein, A.,Jr., (1942) Sedimentary petrologic provinces of the northern Gulf of Mexico. Journal of Sedimentary Petrology, 12(2), 77-84.

Gonella, J., (1972) A rotary-component method for analyzing meteorological and oceanographic vector time series. Deep-Sea Research, 19, 833-846.

Griffin, G.M., (1962) Regional clay-mineral facies, products of weathering intensity and current distribution in the northeastern Gulf of Mexico. Geological Society of America Bulletin, 73, 737-768.

Grambling, R. and S. Brabant, (1984) The role of outer continental shelf oil and gas activities in the growth and modification of Louisiana's coastal zone. University of Southwestern Louisiana.

Gunter, G., (1963) The fertile fisheries crescent. Journal of the Mississippi Academy of Science, 9, 286-290.

Hardy, D.M., (1977) Empirical eigenvector analysis of vector observations. Geophysical Research Letters, 4(8), 319-320.

Hardy, D.M. and J.J. Walton, (1978) Principal components analysis of vector wind measurements. Journal of Applied Meteorology, 17, 1153-1162.

Helland-Hansen, B. (1934) The Sognefjord Section. In: James Johnstone Memorial Volume. University of Liverpool Press, pp257-274.

Henry, W.K., (1979) Some aspects of the fate of cold fronts in the Gulf of Mexico. Monthly Weather Review, 107, 1078-1082.

Herman, A.W. (1982) Spatial and temporal variability of chlorophyll distributions and geostrophic current estimates on the Peru shelf at 9S. Journal of Marine Research, 40, 185-207.

Huang, W.H., L. Doyle, W. Chiou, (1975) Clay mineral studies of surface sediments from the shelf of the northeastern and eastern Gulf of Mexico. In: S.W. Bailey (ed.), Proceedings of the International Clay Conference, Mexico 1975, Applied Pub. LTD, Wilmette, p55-70.

Huh, O.K., W.J. Wiseman, Jr.,and L.J. Rouse, Jr. (1981) Intrusion of Loop Current waters onto the west Florida continental shelf. Journal of Geophysical Research, 86, 4186-4192.

Huh, O.K., L.J. Rouse, and N.D. Walker, (1984) Cold-air outbreaks over the northwest Florida continental shelf: heat flux processes and hydrographic changes. Journal of Geophysical Research, 89, 717-726.

Ichiye, T., (1960) On the hydrography near Mississippi Delta, Oceanographical Magazine, 11(2), 65-78.

Ketchum B.H. and D.J. Keen, (1955) The accumulation of river water over the continental shelf between Cape Cod and Chesapeake Bay. Papers in Marine Biology and Oceanography, Supplement to Deep-Sea Research, 3, 346-357.

Kindinger, J.L., R.L. Miller, C.E. Stelting, and A.H. Bouma, (1982) Depositional history of Louisiana-Mississippi outer continental shelf. United States Geological Survey, Open File Report 82-1077, p52.

Kjerfve, B., (1983) Analysis and synthesis of oceanographic conditions in Mississippi Sound, April thru October 1980. U.S. Army Corps of Engineers, Mobile District, Final Report, p436.

Kjerfve, B. and J.E. Sneed, (1984) Analysis and synthesis of oceanographic conditions in the Mississippi Sound offshore region. U.S. Army Corps of Engineers, Mobile District, Final Report, Vol. 1 and 2.

Komar, P.D. and M.C. Miller, (1975) On the comparison between the threshold of sediment motion under waves and unidirectional currents with a discussion of the practical evaluation of the threshold, Journal of Sedimentary Petrology, 45, 362-367.

Larson, D.K., D. Davis, R. Detro, P. Durmond, E. Liebow, R. Motschall, D. Sorensen, and W. Guidroz, (1980) Mississippi deltaic plain regional ecological characterization: a socioeconomic study. Volume 1, Synthesis papers. U.S. Fish and Wildlife Service, Office of Biological Services, FWS/OBS-79/05.

Legler, D.M., (1983) Empirical orthogonal function analysis of wind vectors over the tropical Pacific region. Bulletin of the American Meteorological Society, 64(3), 234-241.

Leipper, D. (1954) Physical Oceanography of the Gulf of Mexico: Gulf of Mexico, its origin, waters, and marine life. Fishery Bulletin, Fish and Wildlife Service, U.S., 55, 119-137.

Ludwick, J.C., (1964) Sediments in northeastern Gulf of Mexico. In: R.L. Miller (ed.), Papers in marine geology, Macmillan Company, New York.

Marmer, H.A., (1954) Tides and sea level in the Gulf of Mexico. In: P.S. Galtsoff (ed.), Gulf of Mexico, its origins, waters, and marine life. U.S. Fish and Wildlife Service, Fishery Bulletin 89.

Miller, M.C., I.N. McCave, and P.D. Komar, (1977) Threshold of sediment motion under unidirectional currents. Sedimentology, 24, 507-527.

Molinari, R.L., J.F. Festa, and D.W. Behringer (1978) The circulation in the Gulf of Mexico derived from estimated dynamic height fields. Journal of Physical Oceanography, 8, 987-996.

Molinari, R.L., D.A. Mayer, and F. Chew (1979) Physical conditions at a potential OTEC site in the Gulf of Mexico; 88 W, 29 N. NOAA Technical Memorandum ERL AOML-41, pp158.

Molinari, R.L., and D.A. Mayer (1982) Current meter observations on the continental slope in the eastern Gulf of Mexico, Journal of Physical Oceanography, 12, 1480-1492.

Mooers, C.N.K., (1973) A technique for the cross spectrum analysis of pairs of complex-valued time series, with emphasis on properties of polarized components and rotational invariants. Deep-Sea Research, 20, 1129-1141.

Murray, S.P. (1972) Observations on wind, tidal, and density driven currents in the vicinity of the Mississippi River Delta, In.; Shelf sediment transport, D.J.P. Swift, D.B. Duane, and H. Pilkey, editors, Dowden, Hutchinson, and Ross, Stroudsburg, Pa.,p127-142.

Niedoroda, A.W., and D.J.P. Swift, (1981) Maintenance of the shoreface by wave orbital currents and mean flow: observations from the Long Island coast. Geophysical Research Letters, 8(4), 337-340.

Outlaw, D.G., (1983) Prototype tidal data analysis for Mississippi Sound and adjacent areas. Miscellaneous Report CERC-83-1. U.S. Army Engineer Waterways Experiment Station, Vicksburg, MI.

Overland, J.E. and R.W. Preisendorfer, (1982) A significance test for principal components applied to a cyclone climatology. Monthly Weather Review, 110(1), 1-4.

Postma, H. (1867) Sediment transport and sedimentation in the estuarine environment. In: G.H. Lauff (ed.), Estuaries, American Association Advancement of Science, Washington D.C., p158-179.

Raytheon, (1981a) Mississippi Sound and adjacent areas study. Quality control report. First deployment period. Raytheon Ocean Systems Co., East Providence, RI.

Raytheon, (1981b) Mississippi Sound and adjacent areas study. Quality control report. Second deployment period. Raytheon Ocean Systems Co., East Providence, RI.

Raytheon, (1981c) Mississippi Sound and adjacent areas study. Quality control report. Third deployment period. Raytheon Ocean Systems Co., East Providence, RI.

Sahl, L.E., W.J. Merrell, D.W. McGrath, and J.A. Webb, (1987) Transport of mud on continental shelves:evidence from the Texas shelf. Marine Geology, 76, 33-43.

Schmalz, R.A., Jr., (1985) Numerical model investigation of Mississippi Sound and adjacent areas. Miscellaneous Report CERC-85-2. U.S. Army Engineer Waterways Experiment Station, Vicksburg, MI.

Schroeder, W.W. and W.R. Lysinger (1979) Hydrography and circulation of Mobile Bay. In; Symposium on the Natural Resources of the Mobile Bay Estuary, Alabama, H.A. Loyacano and J.P. Smith, editors, U.S. Army Corps of Engineers, Mobile District, 75-94.

Schroeder, W.W., (1981a) Circulation patterns of the Alabama and Mississippi inner continental shelves. Final report Deployment 1, for U.S. Army Engineer District, Mobile. p20.

Schroeder, W.W., (1981b) Circulation patterns of the Alabama and Mississippi inner continental shelves. Final report Deployment 2, for U.S. Army Engineer District, Mobile. p28.

Schroeder, W.W., (1982) Circulation patterns of the Alabama and Mississippi inner continental shelves. Final report Deployment 3, for U.S. Army Engineer District, Mobile. p17.

Schroeder, W.W. and Wm.J. Wiseman, Jr., (1985) An analysis of the winds (1974-1984) and sea level elevations (1973-1983) in coastal Alabama. MASGP-84-024, Mississippi-Alabama Sea Grant Consortium, p102.

Schroeder, W.W., O.K. Huh, L.J. Rouse, Jr., and Wm.J. Wiseman, Jr., (1985) Satellite observations of the circulation east of the Mississippi Delta: Cold-air outbreak conditions. Remote sensing of Environment, 18, 49-58.

Schroeder, W.W., S.P. Dinnel, Wm.J. Wiseman, Jr.,and W.J. Merrell, Jr., (1987) Circulation patterns inferred from the movement of detached buoys in the eastern Gulf of Mexico. Continental Shelf Research, 7:883-894.

Scruton, P.C., (1956) Oceanography of Mississippi Delta sedimentary environments. Bulletin of the American Association of Petroleum Geologists, 40(12), 2864-2952.

Seim, H.E., B. Kjerfve, and J.E. Sneed, (1987) Tides of Mississippi Sound and adjacent continental shelf, Estuarine, Coastal and Shelf Science, 25, 143-156.

Servain, J. and D.M. Legler, (1986) Empirical orthogonal analysis of tropical Atlantic sea surface temperature and wind stress: 1964-1979. Journal of Geophysical Research, 91, 14,181-14,191.

Shay, L.K., and R.L. Elsberry, (1987) Near-inertial ocean current responses to Hurricane Frederic. Journal of Physical Oceanography, 17, 1249-1269.

Shepard, F.P., (1956) Marginal sediments of Mississippi Delta. Bulletin of the American Association of Petroleum Geologists, 40(11), 2537-2634.

Sheng, Y.P., (1983) Mathematical modeling of three-dimensional coastal currents and sediment dispersion: model development and application. Technical Report CERC-83-2. U.S. Army Engineer Waterways Experiment Station, Vicksburg, MI.

Smedstad, O.M., and J.E. Weber (1986) Geostrophic currents in shelf areas. Continental Shelf Research, 6, 655-670.

Stephansson, U., L.P. Atkinson, and D.F. Bumpus (1971) Hydrographic properties and circulation of the North Carolina shelf and slope waters. Deep-Sea Research, 18, 383-420.

Sturges, W. and J.C. Evans, (1983) On the variability of the Loop current in the Gulf of Mexico. Journal of Marine Research, 41(4), 639-653.

Sverdrup, H.U., M.W. Johnson, and R.H. Fleming (1942) The oceans, their physics, chemistry and general biology, Prentice-Hill Inc., Englewood, N.J., pp1087.

Swift, D.J.P., D.J. Stanley, and J.R. Curray, (1971) Relict sediments on continental shelves: a reconsideration. Journal of Geology, 79, 322-346.

Thompson, S.H., and E.L. Arnold, Jr., (1971) Gulf of Mexico fisheries. In: S. Shapiro (ed.), Our changing fisheries, U.S. Government printing Office, Washington D.C.

TRI, (1983) Proceedings of the Mobile Bay area drilling fluids transport study plan workshop, December6-8, 1983, Mobile, Al. Sponsored by the U.S. Environmental Protection Agency.

Tolbert, W.H., and G.G. Salsman (1964) Surface circulation of the eastern Gulf of Mexico as determined by drift-bottle studies. Journal of Geophysical Research, 69, 223-230.

U.S. Army, (1974) Deep draft access to ports of New Orleans and Baton Rouge. Draft environmental statement, Corps of Engineers, New Orleans District.

U.S. Army, (1977) Shore Protection Manual, CERC, U.S. Government Printing Office.

U.S. Army, Draft Report, Gulf of Mexico Hindcast Wave Information. WIS Report 18, CERC, Corps of Engineers, Vicksburg.

U.S. Department of Commerce (1972) Environmental Guide for the U.S. Gulf Coast. NCC, NOAA, U.S. Government Printing Office.

U.S. Department of Commerce (1985) Gulf of Mexico, Coastal and Ocean Zones Strategic Assessment Data Atlas. NOAA, U.S. Government Printing Office, Washington D.C.

U.S. Department of Commerce (1985) National Estuarine Inventory Data Atlas, Physical and Hydrologic Characteristics. NOAA, U.S. Government Printing Office, Washington D.C.

U.S. Department of the Interior, (1982) Bottom sediments and selected endangered and threatened species, Map 1. Minerals Management Service, New Orleans Outer Continental Shelf Regional Office.

Upshaw, C.F., W.B. Creath, and F.L. Brooks, (1966) Sediments and microfauna off the coasts of Mississippi and adjacent states. Mississippi Geological, Economic and Topographical Survey, 106, 1-127.

Van Andel, T.H. (1960) Sources and dispersion of Holocene sediments, northern Gulf of Mexico. In: F.P. Shepard, F.B. Phleger, and T.H. Van Andel (eds.), Recent sediments, northwestern Gulf of Mexico. American Association of Petroleum Geologists, Tulsa, Ok, p394.

Van Andel, T.H. and D.M. Poole, (1960) Sources of recent sediments in the northern Gulf of Mexico. Journal of Sedimentary Petrology, 30(1), 91-122.

Vittor, B.A., and Associates, (1985) Tuscaloosa Trend regional data search and synthesis study (Volume I- Synthesis Report), Final report submitted to Minerals Management Service, Metairie, La. p477.

Wiseman, Wm.J., Jr., W.W. Schroeder, S.P. Dinnel, (1988) Shelf-estuarine water exchanges between the Gulf of Mexico and Mobile Bay, Alabama. In; American Fisheries Society Symposium, 3, 1-8.

Wiseman, Wm.J., Jr. and S.P. Dinnel, (1988) Shelf currents near the Mississippi delta. Journal of Physical Oceanography, 18(9), 1287-1291.

APPENDIX I

Complex empirical orthogonal function analysis (EOF) produces rotationally invariant eigenvectors. In order to better interpret the associated patterns described by these vectors, they need to be related to the physical setting or coordinate system. Each principal component has a major axis of variation, a preferred orientation, which must be determined. For each principal component,

$\underline{Z}_m = \underline{V}_{lt}\underline{E}_{lm}$,

where, $\underline{V}$, a set of l complex input time series with t points, is multiplied by, $\underline{E}_{lm}$, the eigenvector associated with l complex input time series and m modes. $\underline{E}_{lm}$ can be expressed as,

$E_{lm} = B_{lm}\exp(-\theta_{lm})$,

where, B_{lm}, is a weight, and, θ_{lm}, is a phase angle. These phase angles are rotationally invariant within each mode, and so are equivalent to the sum of θ_{lm} and a constant angle, P_m, an inferred preferred orientation angle of each mode. If, for some P_m, the quantity $(\underline{V}_{lt}\underline{E}_{lm})^2$ is maximized over all t and l, i.e.

$$\sum_{t=1}^{t} \sum_{l=1}^{l} (\underline{V}_{lt}\underline{E}_{lm})^2$$

then P_m is the angle of preferred orientation relative to the input coordinate system.

Dropping the subscripts for convenience, but remembering that all eigenvector components, either amplitude or phase

angle, have subscripts l and m, that the preferred orientation P, has subscript m, and that input vector subscripts are t and l, we have

$(\underline{VE})^2 = (\underline{V}B\exp(-\theta+P)^2$

$=\{(u+iv)(B\cos(\theta+P)-iB\sin(\theta+P)\}^2$

$=\{[uB\cos(\theta+P)+vB\sin(\theta+P)]+i[vB\cos(\theta+P)-uB\sin(\theta+P)]\}^2$

$=u^2B^2\cos^2(\theta+P)+2uvB^2\cos(\theta+P)\sin(\theta+P)+v^2B^2\sin^2(\theta+P)$

$+v^2B^2\cos^2(\theta+P)+2uvB^2\cos(\theta+P)\sin(\theta+P)-u^2B^2\sin^2(\theta+P)$

$+i[2uvB^2\cos^2(\theta+P)-2uvB^2\sin(\theta+P)\cos(\theta+P)$

$+v^2B^2\sin(\theta+P)\cos(\theta+P)-2uvB^2\sin^2(\theta+P)]$

$=(u2B2-v2B2)\cos2(\theta+P)+4uvB2\cos(\theta+P)\sin(\theta+P)$

$-(u^2B^2)\sin^2(\theta+P)+i[(2uvB^2)\cos^2(\theta+P)-(2uvB^2)\sin^2(\theta+P)$

$+(v^2B^2-u^2B^2)2\sin(\theta+P)\cos(\theta+P)$

Now using the sum of two angles identity we can write

$=(u^2B^2-v^2B^2)(\cos^2\theta\cos^2P+\sin^2\theta\sin^2P-2\cos\theta\cos P\sin\theta\sin P)$

$+(v^2B^2-u^2B^2)(\sin^2\theta\cos^2P+\cos^2\theta\sin^2P+2\sin\theta\cos P\cos\theta\sin P)$

$+(4uvB^2)(\sin\theta\cos\theta\cos^2P-\sin^2P\cos\theta\sin\theta$

$+\cos^2\theta\cos P\sin\theta-\sin^2\theta\cos P\sin P)$

$+i[(2uvB^2)(\cos^2\theta\cos^2P+\sin^2\theta\sin^2P-2\cos\theta\cos P\sin\theta\sin P)$

$-(2uvB^2)(\sin^2\theta\cos^2P+\cos^2\theta\sin^2P+2\sin\theta\cos P\cos\theta\sin P)$

$+2(v^2B^2-u^2B^2)(\sin\theta\cos\theta\cos^2P-\sin^2P\cos\theta\sin$

$+\cos^2\theta\cos P\sin P-\sin^2\theta\cos P\sin P)]$

Now let

$C_1 = u^2B^2-v^2B^2$, and $C_2 = 4uvB^2$, substituting in

$=C_1\cos^2\theta\cos^2P+C_1\sin^2\theta\sin^2P-2C_1\cos\theta\sin\theta\sin P\cos P$

$-C_1\sin^2\theta\cos^2P-C_1\cos^2\theta\sin^2P+C_2\sin\theta\cos P\cos^2P-C_2\cos\theta\sin\theta\sin^2P$

$+C_2\cos^2\theta\cos P\sin P-C_2\sin^2\theta\cos P\sin P$

$+i[C_2/2(\cos^2\theta\cos^2P+\sin^2\theta\sin^2P-\sin^2\theta\cos^2P-\cos^2\theta\sin^2P)$

$+2C_1(\cos\theta\sin P\sin^2P-\sin\theta\cos\theta\cos^2P+\cos P\sin P\sin^2\theta-\cos P\sin P\cos^2\theta$

$-2C_2(\cos\theta\sin\theta\sin P\cos P)$

Now regroup and combine terms.

$=\cos^2P(C_1\cos^2\theta-C_1\sin^2\theta+C_2\sin\theta\cos\theta)$

$+\sin^2P(C_1\sin^2\theta-C_1\cos^2\theta-C_2\cos\theta\sin\theta)$

$+\sin P\cos P(C_2\cos^2\theta-C_2\sin^2\theta-2C_1\cos\theta\sin\theta)$

$+i[\cos^2P(C_2/2\cos^2\theta-C_2/2\sin^2\theta-2C_1\sin\theta\cos\theta)$

$+\sin^2P(C_2/2\sin^2\theta-C_2/2\cos^2\theta+2C_1\cos\theta\sin\theta)$

$+\sin P\cos P(2C_1\sin^2\theta-2C_1\cos^2\theta-2C_2\cos\theta\sin\theta)]$

Now let

$D_1 = C_1\cos^2\theta-C_1\sin^2\theta+C_2\sin\theta\cos\theta,$

$D_2 = C_2\cos^2\theta-C_2\sin^2\theta-2C_1\cos\theta\sin\theta,$

$D_3 = C_2/2\cos^2\theta-C_2/2\sin^2\theta-2C_1\cos\theta\sin\theta,$

$D_4 = 2C_1\sin^2\theta-2C_1\cos^2\theta-2C_2\cos\theta\sin\theta.$

Substitution gives us,

$=D_1(\cos^2P-\sin^2P)+D_2\cos P\sin P+i[D_4\cos P\sin P+D_3(\cos^2P-\sin^2P)]$

Taking the derivative with respect to P, i.e. d/dP is

$=D_2(\cos^2P-\sin^2P)-2D_1\cos P\sin P+i[D_4(\cos^2P-\sin^2P)-4D_3\cos P\sin P]$

To maximize this function, the first derivative is set equal to zero, remember that a complex function is zero when the real portion is equal to zero.

$0 = D_2(\cos^2P-\sin^2P)-2D_1\cos P\sin P$

Solve for P.

$D_2(\cos^2P\sin^2P)=2D_1\cos P\sin P$

$$\frac{\cos^2P-\sin^2P}{\cos P\sin P} = \frac{4D_1}{D_2}$$

$$\frac{\cos^2 P}{\cos P \sin P} - \frac{\sin^2 P}{\cos P \sin P} = \frac{4D_1}{D_2}$$

$$\cot P - \tan P = \frac{4D_1}{D_2}$$

$$\frac{1}{\tan P} - \tan P - \frac{4D_1}{D_2} = 0$$

$$\tan^2 P + \frac{4D_1}{D_2}\tan P - 1 = 0$$

Solving the quadratic equation for tanP,

$$\tan P = \frac{-\frac{4D_1}{D_2} \pm \left[\left(\frac{4D_1}{D_2} \right)^2 - 4 \right]^{\frac{1}{2}}}{2} .$$

Solving for P,

$$P = \tan^{-1}\left[-\frac{D_1}{D_2} \pm \left(\frac{D_1^2}{D_2^2} + 1 \right)^{\frac{1}{2}} \right]$$

This gives two angles of preferred orientation, either P_1 or P_2, one is the maximum and the other is the minimum. To determine the maximum angle of preferred orientation, the second derivative with respect to P was taken, the maximum corresponds to the angle P with a negative second derivative.

$$\frac{d^2}{dP^2} = \frac{1}{\cos^2 P}\left(2\tan P + \frac{4D_1}{D_2}\right)$$

The resultant angle P can be added to each individual phase angle within each mode. Where,

$$P=\tan^{-1}\left\{ -2\frac{(u^2-v^2)(\cos^2\theta-\sin^2\theta)+4uv\sin\theta\cos\theta)}{4uv(\cos^2\theta-\sin^2\theta)-s(u^2-v^2)\cos\theta\sin\theta} \pm \left[4\frac{(u^2-v^2)(\cos^2\theta-\sin^2\theta)+4uv\sin\theta\cos\theta)}{4uv(\cos^2\theta-\sin^2\theta)-s(u^2-v^2)\cos\theta\sin\theta} - 1\right]^{\frac{1}{2}}\right) .$$

P_m is not a function of B_{1m}, the magnitude of the individual eigenvectors within each mode, but only of the input vectors and the individual phase angles within each mode.

APPENDIX II

Formulation of the vertically integrated horizontal momentum equations beginning with the instantaneous horizontal momentum equations, neglecting viscous forces,

$$\frac{Du}{Dt} = \frac{\partial u}{\partial t} + u\frac{\partial u}{\partial x} + v\frac{\partial u}{\partial y} + w\frac{\partial u}{\partial z} = \frac{\partial P}{\partial x} + fv$$

$$\frac{Dv}{Dt} = \frac{\partial v}{\partial t} + u\frac{\partial v}{\partial x} + v\frac{\partial v}{\partial y} + w\frac{\partial v}{\partial z} = \frac{\partial P}{\partial y} - fu \ .$$

Then, separating each term into a mean and a fluctuating part, i.e. $u = \bar{u} + u'$, by defining a time average so that

$$\bar{u} = \frac{1}{T}\int_0^T \bar{u}dt \ , \text{ and } \quad 0 = \frac{1}{T}\int_0^T u'dt \ ,$$

produces the Reynolds' Stress form of the equations,

$$\frac{\partial \bar{u}}{\partial t} + \bar{u}\frac{\partial \bar{u}}{\partial x} + \bar{v}\frac{\partial \bar{u}}{\partial y} + \bar{w}\frac{\partial \bar{u}}{\partial z} - f\bar{v} =$$

$$- g\int_h^\eta \frac{\partial \rho}{\partial x}dz - g\frac{\partial \eta}{\partial x} - \frac{\partial(\overline{u'u'})}{\partial x} - \frac{\partial(\overline{u'v'})}{\partial y} - \frac{\partial(\overline{u'w'})}{\partial z}$$

$$\frac{\partial \bar{v}}{\partial t} + \bar{u}\frac{\partial \bar{v}}{\partial y} + \bar{v}\frac{\partial \bar{v}}{\partial y} + \bar{w}\frac{\partial \bar{v}}{\partial z} + f\bar{u} =$$

$$- g\int_h^\eta \frac{\partial \rho}{\partial y}dz - g\frac{\partial \eta}{\partial y} - \frac{\partial(\overline{u'v'})}{\partial x} - \frac{\partial(\overline{v'v'})}{\partial y} - \frac{\partial(\overline{w'v'})}{\partial z} \ .$$

The overbar designates the time average of a quantity. Only the momentum equation in the x direction will be fully described. The vertical velocity component, w, can be scaled

from the continuity equation. If characteristic horizontal velocities are 0.1 m/s, and horizontal length scales are 50 km, then for depths of 20 m, the vertical velocity, w, scales as u x 10^{-3}, and the vertical momentum equation becomes the hydrostatic equation for moderate time scales. The time averaged continuity equation multiplied by a velocity component was added to the nonlinear field acceleration terms,

$$\bar{u}\frac{\partial\bar{u}}{\partial x} + \bar{v}\frac{\partial\bar{u}}{\partial y} + \bar{w}\frac{\partial\bar{u}}{\partial z} + \bar{u}\left(\frac{\partial\bar{u}}{\partial x} + \frac{\partial\bar{v}}{\partial y} + \frac{\partial\bar{w}}{\partial z}\right) ,$$

to get the nonlinear terms into the following form,

$$\frac{\partial(\overline{uu})}{\partial x} + \frac{\partial(\overline{uv})}{\partial y} + \frac{\partial(\overline{uw})}{\partial z} .$$

Vertically integration of the Reynolds Stress form of the momentum equations, from the surface, n, to the bottom, h, using Leibnitz's Rule for differentiation, produces,

$$\begin{aligned}
&\frac{\partial}{\partial t}\left(\int_h^\eta \bar{u}\,dz\right) + \bar{u}_\eta\frac{\partial\eta}{\partial t} - \bar{u}_h\frac{\partial h}{\partial t} \\
&+ \frac{\partial}{\partial x}\left(\int_h^\eta \overline{uu}\,dz\right) + \overline{uu}_h\frac{\partial\eta}{\partial x} - \overline{uu}_h\frac{\partial h}{\partial x} \\
&+ \frac{\partial}{\partial y}\left(\int_h^\eta \overline{uv}\,dz\right) + \overline{uv}_\eta\frac{\partial\eta}{\partial y} - \overline{uv}_h\frac{\partial h}{\partial y} \\
&+ \overline{uw}_\eta - \overline{uw}_h - f\int_h^\eta \bar{v}\,dz = -g\int_h^\eta\int_h^\eta \frac{\partial\rho}{\partial x}\,dz\,dz - g\int_h^\eta \frac{\partial\eta}{\partial x}\,dz \\
&- \frac{\partial}{\partial x}\left(\int_h^\eta \overline{u'u'}\,dz\right) - \overline{u'u'}_\eta\frac{\partial\eta}{\partial x} + \overline{u'u'}_h\frac{\partial h}{\partial x}
\end{aligned}$$

$$- \frac{\partial}{\partial y}\left(\int_h^\eta \overline{u'v'}\,dz\right) - \overline{u'v'}_\eta \frac{\partial \eta}{\partial y} + \overline{u'v'}_h \frac{\partial h}{\partial y}$$

$$- \overline{u'w'}_\eta + \overline{u'w'}_h \ .$$

Now we define the horizontal time mean velocity as a vertical mean and a variation about the vertical mean, i.e. $u = U + u''$, where the vertical integration over water depth H, yields,

$$U = \frac{1}{H}\int_h^\eta \hat{u}\,dz, \text{ and } 0 = \frac{1}{H}\int_h^\eta u''\,dz \ .$$

Let $\langle \cdot \rangle$ denote a vertically integrated quantity. Using this notation we now can write the vertically integrated alongshore momentum equation as,

$$\frac{\partial (HU)}{\partial t} + \frac{\partial (HUU)}{\partial x} + \frac{\partial (HUV)}{\partial y}$$

$$+ \bar{u}_\eta \frac{\partial \eta}{\partial t} + \overline{\bar{u}\bar{u}}_\eta \frac{\partial \eta}{\partial x} + \overline{\bar{u}\bar{v}}_\eta \frac{\partial \eta}{\partial y} + \overline{\bar{u}\bar{w}}_\eta \qquad \text{(a)}$$

$$- \bar{v}_h \frac{\partial h}{\partial t} - \overline{\bar{v}\bar{u}}_h \frac{\partial h}{\partial x} - \overline{\bar{v}\bar{v}}_h \frac{\partial h}{\partial y} - \overline{\bar{u}\bar{w}}_h \qquad \text{(b)}$$

$$- fHV = -g\frac{H^2}{2}\frac{\partial \rho}{\partial x} - g\rho H \frac{\partial \eta}{\partial x}$$

$$- \frac{\partial (H\langle \overline{u'u'} + \langle u'u' \rangle \rangle)}{\partial x} - \frac{\partial (H\langle \overline{u'v'} + \langle u'v' \rangle \rangle)}{\partial y} \qquad \text{(c)}$$

$$- \langle \overline{u'u'} \rangle_\eta \frac{\partial \eta}{\partial x} - \langle \overline{u'v'} \rangle_\eta \frac{\partial \eta}{\partial y} \qquad \text{(c)}$$

$$+ \langle \overline{u'u'} \rangle_h \frac{\partial h}{\partial x} + \langle \overline{u'v'} \rangle_h \frac{\partial h}{\partial y} \qquad \text{(c)}$$

$$- \langle\overline{u'w'}\rangle_\eta + \langle\overline{u'w'}\rangle_h$$

Where line (a), after distributing out u_η, reduces to zero,

$$\bar{u}_\eta \left[\left(\frac{\partial\eta}{\partial t}\right) + \bar{u}_\eta\left(\frac{\partial\eta}{\partial x}\right) + \bar{v}_\eta\left(\frac{\partial h}{\partial y}\right) + \bar{w}_\eta\right] = 0$$

Line (b) reduces to zero in a similar manner.

$$\bar{u}_\eta\left[-\left(\frac{D\eta}{Dt}\right)_\eta + \bar{w}_\eta\right] = \bar{u}_\eta[-\bar{w}_\eta + \bar{w}_\eta] = 0 \ .$$

Line (c), derived from the integration of the flux terms, is a generalized Reynolds' Stress. They cannot be described with our data and we are forced to leave these terms out of our final momentum balance or confine them to the residual term.

We define the surface and bottom stresses, τ_{sx} and τ_{by}, as $\langle u'w'\rangle_\eta$ and $\langle v'w'\rangle_h$, respectively. These stresses are usually defined as $\rho\langle u'w'\rangle_\eta$ and $\rho\langle u'w'\rangle_h$.

The vertical integration of the horizontal pressure gradient term produces two terms, the baroclinic pressure gradient,

$$-g\frac{H^2}{2}\frac{\partial\rho}{\partial x},$$

and the barotropic pressure gradient,

$$-g\rho H\frac{\partial\eta}{\partial x}.$$

The baroclinic pressure gradient was not directly determined because of inadequate hydrographic data and is included as

part of the residual term. Scale analysis suggests that a baroclinic pressure gradient the same order of magnitude as the barotropic pressure gradient, would have a 1 kg/m^3 density difference over 10 km horizontal distance, assuming a water column of 20 m. This not unlikely for a cross-shelf gradient, especially across the coastal boundary layer in this region. The variability present on the shelf may not produce the necessary contribution, i.e. residual term value, and because of the lack of good hydrographic data we can not determine when an adequate baroclinic term would be important.

The vertically integrated horizontal momentum equations are, then,

$$\frac{\partial U}{\partial x} + \frac{\partial UU}{\partial x} + \frac{\partial VU}{\partial y} - fV + g\frac{\partial \eta}{\partial x} - \frac{\tau_{sx}}{\rho_w H} + \frac{\tau_{bx}}{\rho_w H} = R_x$$

$$\frac{\partial V}{\partial y} + \frac{\partial VU}{\partial x} + \frac{\partial VV}{\partial y} - fV + g\frac{\partial \eta}{\partial y} - \frac{\tau_{sy}}{\rho_w H} + \frac{\tau_{by}}{\rho_w H} = R_y$$

Where the residual terms, R_x and R_y, contain the unneglected but undeterminable terms of each component equation, i.e the generalized Reynolds' Stresses and the baroclinic pressure gradient terms.

APPENDIX III

The following tables contain the empirical orthogonal function analysis output for current meters, current meters plus DI wind stress, current meters plus BY wind stress, and current meter plus both wind stress as inputs.

Table A. Complex empirical orthogonal function statistics: percent total variance explained, $\%S_t$, individual weights, B, arbitrary phase angles, θ, and percent individual input variance explained, $\%S_i$, for Mode 1, MS1. Inputs were current meters, current meters and DI wind stress, current meters and BY wind stress, and current meters and both wind stress.

	Inputs									
	1B	2S	2B	3S	5S	5B	8S	8B	DI	BY
Current Meters					$\%S_t$ = 58.30					
B	0.18	0.31	0.36	0.37	0.36	0.41	0.40	0.40		
θ	180	103	128	7	11	51	-15	26		
$\%S_i$	15	44	61	63	59	77	76	73		
Current meters and DI T_w					$\%S_t$ = 53.10					
B	0.16	0.28	0.35	0.37	0.35	0.40	0.41	0.39	0.18	
θ	180	98	123	-1	3	55	22	19	29	
$\%S_i$	12	38	60	65	60	76	78	74	15	
Current Meters and BY T_w					$\%S_t$ = 55.01					
B	0.16	0.27	0.35	0.36	0.34	0.39	0.40	0.39		0.20
θ	180	98	121	-3	1	44	-24	17		-14
$\%S_i$	13	38	61	63	58	76	78	74		34
Current Meters and Both T_w					$\%S_t$ = 51.37					
B	0.15	0.24	0.34	0.35	0.34	0.38	0.39	0.38	0.21	0.29
θ	180	90	113	-25	-10	35	-35	-174	-169	-22
$\%S_i$	11	31	59	64	58	73	80	73	23	43

+ Positive phase measured counterclockwise.

Table B. As in table A, except for mode 2, MS1.

	Inputs									
	1B	2S	2B	3S	5S	5B	8S	8B	DI	BY
Current Meters					$\%S_t$ = 18.50					
B	0.68	0.49	0.25	0.26	0.28	0.10	0.24	0.15		
θ	-85	-122	-142	-84	-77	73	-77	-35		
$\%S_i$	69	35	9	10	12	2	9	3		
Current meters and DI T_w					$\%S_t$ = 21.69					
B	0.55	0.46	0.23	0.22	0.20	0.08	0.16	0.08	0.55	
θ	-77	-115	-135	-89	-84	139	-75	-49	9	
$\%S_i$	60	41	10	10	8	1	5	1	58	
Current Meters and BY T_w					$\%S_t$ = 19.47					
B	0.59	0.49	0.22	0.25	0.25	0.08	0.19	0.10		0.44
θ	-74	-110	-127	-90	-86	142	-82	-53		8
$\%S_i$	61	42	9	11	11	1	6	2		34
Current Meters and Both T_w					$\%S_t$ = 22.77					
B	0.48	0.46	0.21	0.22	0.20	0.13	0.12	0.08	0.50	0.38
θ	-53	-90	-100	-86	-87	-159	-84	-89	28	14
$\%S_i$	52	47	10	11	9	4	3	2	57	34

+ Positive phase measured counterclockwise.

Table C. As in table A, except for mode 1, MS2.

	Inputs									
	1B	1B	2S	2B	3S	4S	4B	5S	6S	6B
Current Meters					$\%S_t$ = 38.22					
B	0.20	0.28	0.22	0.29	0.36	0.38	0.23	0.27	0.25	0.13
θ	0	24	-51	-26	-145	-159	-131	-172	-153	-173
$\%S_i$	20	38	24	42	64	72	26	37	32	8
Current meters and DI T_w					$\%S_t$ = 38.28					
B	0.20	0.26	0.22	0.27	0.35	0.36	0.23	0.24	0.24	0.13
θ	0	21	-49	-33	-149	-163	-138	-175	-158	174
$\%S_i$	20	36	26	40	65	70	29	31	32	9
Current Meters and BY T_w					$\%S_t$ = 37.77					
B	0.19	0.26	0.23	0.27	0.35	0.37	0.23	0.26	0.24	0.13
θ	0	24	-48	-29	-145	-160	-135	-172	-154	176
$\%S_i$	20	35	27	37	66	70	28	35	30	8
Current Meters and Both T_w					$\%S_t$ = 38.43					
B	0.19	0.24	0.22	0.25	0.34	0.34	0.23	0.23	0.23	0.13
θ	0	21	-46	-37	-149	-164	-140	-174	-159	165
$\%S_i$	20	32	28	35	65	67	30	29	29	10

+ Positive phase measured counterclockwise.

Table C continued.

	Inputs 7S	8S	8B	DI	BY
Current Meters			$\%S_t$ = 38.22		
B	0.30	0.29	0.31		
θ	-161	-170	-111		
$\%S_i$	45	41	49		
Current meters and DI T_w			$\%S_t$ = 38.28		
B	0.29	0.26	0.31	0.29	
θ	-165	-174	-118	-170	
$\%S_i$	45	38	50	45	
Current Meters and BY T_w			$\%S_t$ = 37.77		
B	0.30	0.27	0.30		0.27
θ	-160	-170	-114		-173
$\%S_i$	48	39	49		37
Current Meters and Both T_w			$\%S_t$ = 38.43		
B	0.28	0.25	0.29	0.31	0.28
θ	-164	-173	-120	-172	-176
$\%S_i$	46	35	49	54	46

+ Positive phase measured counterclockwise.

Table D. As in table A, except for mode 2, MS2

	Inputs 1B	1B	2S	2B	3S	4S	4B	5S	6S	6B
Current Meters					$\%S_t$ = 17.16					
B	0.18	0.16	0.37	0.36	0.15	0.05	0.30	0.28	0.29	0.48
θ	50	164	-5	-146	-47	77	171	-68	98	121
$\%S_i$	7	6	31	28	5	1	20	18	18	52
Current meters and DI T_w					$\%S_t$ = 16.97					
B	0.19	0.18	0.37	0.35	0.15	0.08	0.27	0.30	0.25	0.44
θ	26	132	-30	176	-67	-1	138	-85	60	88
$\%S_i$	9	8	33	28	6	1	17	22	15	46
Current Meters and BY T_w					$\%S_t$ = 16.84					
B	0.15	0.19	0.35	0.38	0.14	0.08	0.27	0.26	0.27	0.46
θ	56	175	-2	-152	-40	48	168	-59	88	118
$\%S_i$	5	9	29	33	5	2	18	17	17	50
Current Meters and Both T_w					$\%S_t$ = 16.78					
B	0.15	0.21	0.34	0.36	0.15	0.13	0.24	0.29	0.24	0.41
θ	34	141	-28	169	-58	-7	133	-79	47	83
$\%S_i$	6	11	29	33	6	4	14	22	14	43

+ Positive phase measured counterclockwise.

Table D cont.

	Inputs 7S	8S	8B	DI	BY
Current Meters			$\%S_t$ = 17.16		
B	0.26	0.20	0.26		
Θ	-89	-33	180		
$S_i\%$	15	9	15		
Current meters and DI T_w			$\%S_t$ = 16.97		
B	0.22	0.23	0.23	0.26	
Θ	-109	-55	136	143	
$S_i\%$	11	12	12	16	
Current Meters and B T_w			$\%S_t$ = 16.84		
B	0.23	0.21	0.25	0.26	
Θ	-86	-26	170	-164	
$S_i\%$	13	11	14	15	
Current Meters and Both T_w			$\%S_t$ = 16.78		
B	0.20	0.24	0.22	0.26	0.25
Θ	-105	-51	126	142	163
$S_i\%$	10	15	12	17	16

+ Positive phase measured counterclockwise.

Table E. As in table A, except for modes 1 and 2, MS3. Inputs are currents meters, and current meters and DI wind stress.

	Inputs							
	2B	4S	5S	7S	7B	8S	8B	
Mode 1 Current Meters								$\%S_t$ = 71.14
B	0.36	0.41	0.37	0.39	0.37	0.39	0.35	
θ	0	-131	-127	-123	-107	-136	-97	
$\%S_i$	66	82	68	74	69	76	63	
Mode 1 Current meters and DI T_w								$\%S_t$ = 63.86
B	0.36	0.40	0.36	0.38	0.36	0.39	0.35	0.18
θ	0	-132	-128	-124	-106	-137	-98	-108
$\%S_i$	66	80	67	75	68	77	62	16
Mode 2 Current Meters								$\%S_t$ = 12.52
B	0.48	0.07	0.43	0.32	0.35	0.43	0.41	
θ	0	-49	88	72	-69	64	67	
$\%S_i$	20	0	17	9	11	16	15	
Mode 2 Current meters and DI T_w								$\%S_t$ = 13.44
B	0.28	0.18	0.24	0.21	0.38	0.26	0.15	0.75
θ	0	-27	-134	63	-78	53	-60	168
$\%S_i$	9	4	6	5	16	7	2	60

+ Positive phase measured counterclockwise.

VITA

Scott Page Dinnel was born in Olney, Maryland in 1955. He graduated from Albert Einstein High School, Kensington, Maryland, in 1973. He graduated from the University of South Carolina, Columbia, South Carolina, with a B.S. in Marine Science in 1979. He graduated from the Louisiana State University, Baton Rouge, Louisiana, with an M.S. in Marine Sciences in 1983. He is married and has three children. After finishing his Ph.D. he will be employed as an assistant professor in the Marine Science Department at the University of Southern Mississippi.

DOCTORAL EXAMINATION AND DISSERTATION REPORT

Candidate: Scott Page Dinnel

Major Field: Marine Sciences

Title of Dissertation: CIRCULATION AND SEDIMENT DISPERSAL ON THE LOUISIANA-MISSISSIPPI-ALABAMA CONTINENTAL SHELF

Approved:

Major Professor and Chairman

Dean of the Graduate School

EXAMINING COMMITTEE:

William W. Schroeder

Date of Examination:

November 18, 1988